

# Kaon and Pion Production in Centrality Selected Minimum Bias Pb+Pb Collisions at 40 and 158 A·GeV

Dissertation  
zur Erlangung des Doktorgrades  
der Naturwissenschaften

vorgelegt beim Fachbereich Physik  
der Johann Wolfgang Goethe - Universität  
in Frankfurt am Main

von  
Peter Dinkelaker  
aus Frankfurt am Main

CERN-THESIS-2009-146  
2009  


FRANKFURT AM MAIN, 2009  
(D30)

vom Fachbereich Physik der

Johann Wolfgang Goethe - Universität als Dissertation angenommen.

Dekan: Prof. Dr. Dirk-Hermann Rischke

Gutachter: Prof. Dr. Dr. h.c. Reinhard Stock, Prof. Dr. Christoph Blume

Datum der Disputation:

# Zusammenfassung

Alle bekannte Materie besteht aus elementaren Fermionen (Quarks und Leptonen). Die Kernbausteine aller chemischen Elemente sind Protonen und Neutronen, die aus Quarks aufgebaut sind. Zusammen mit den Elektronen in der Atomhülle bilden sie die Atome des Periodensystems der chemischen Elemente, aus dem die uns bekannten Formen der alltäglichen Materie bestehen. Die moderne Schwerionen- und Teilchenphysik beschäftigt sich mit den elementaren Bausteinen der Materie. Um diese zu untersuchen, sind aufgrund der hohen Bindungskräfte enorme Energien notwendig. Bei den in dieser Arbeit untersuchten Energiebereichen treten relativistische Effekte auf und die kinetische Energie der beschleunigten Ionen wird durch den Zusammenprall mit dem zweiten Kern teilweise in neue Teilchen und Antiteilchen umgewandelt. Die von Einstein postulierte Äquivalenz von Energie und Masse  $E = mc^2$  lässt sich dadurch genauso beobachten wie exotischer anmutende relativistische Phänomene wie die Lorentz-Kontraktion der Länge, die relativistische Erhöhung der Masse und die Zeitdilatation. So verlangsamt sich die Eigenzeit eines sich bewegenden Teilchens im Vergleich zum ruhenden Inertialsystem. Dies lässt sich durch die Beobachtung von Teilchen mit einer bekannten mittleren Lebensdauer beobachten. So lebt ein Teilchen mit einer Geschwindigkeit von 99% der Lichtgeschwindigkeit  $\beta = v/c = 0.99$  betrachtet aus dem ruhenden Laborsystem 10-mal länger, als wenn es sich nicht bewegen würde. Die gleiche Beobachtung lässt sich bei der Höhenstrahlung machen. Hier werden durch Kollisionen der Höhenstrahlung mit der Erdatmosphäre Muonen  $\mu$  erzeugt, die eine mittlere Lebensdauer von  $2.2 \cdot 10^{-6}$  s haben. Licht legt in dieser Zeit eine Strecke von 660 m zurück, das heißt am Erdboden sollten quasi keine Muonen mehr beobachtbar sein. Tatsächlich legen die Muonen durch ihre hohe Geschwindigkeit und ihre damit langsamer ablaufende Eigenzeit eine viel längere Strecke zurück.

Das Standardmodell der Elementarteilchenphysik beschreibt die Wechselwirkungen der elementaren Fermionen über den Austausch von Vektorbosonen. Die Fermionen gliedern sich in Quarks und Leptonen. Es gibt drei Familien von Quarks: up und down, strange und charm, top und bottom. Auch bei den Leptonen gibt es drei Familien: das Elektron und das Elektron-Neutrino, das Muon und das Muon-Neutrino sowie das Tau und das Tau-Neutrino. Die Wechselwirkungsteilchen sind das Photon für die elektronmagnetische Wechselwirkung, das Z- und die W-Bosonen für die schwache Wechselwirkung und das Gluon für die starke Wechselwirkung. Die Gravitation als

---

vierte Wechselwirkung wird nicht durch das Standardmodell beschrieben.

Die Quantenchromodynamik (QCD) beschreibt die starke Wechselwirkung mit ihren drei Farbladungen (rot, grün und blau). Die starke Wechselwirkung unterscheidet sich von den anderen Wechselwirkungen insbesondere dadurch, dass das Wechselwirkungsteilchen Gluon selbst eine Farbladung trägt. Diese Selbstwechselwirkung führt zur Besonderheit, dass die Stärke der Wechselwirkung nicht wie bei den anderen Wechselwirkungen mit zunehmender Entfernung geringer wird, sondern dass die zur Separation der Farbladungen nötige Energie mit größerer Entfernung so stark anwächst, dass es energetisch günstiger wird ein Teilchen-/Anti-Teilchen-Paar zu erzeugen, das die sich entfernenden Farbladungen neutralisiert. Dieses Phänomen zwingt alle farbladungstragenden Teilchen in farbneutrale Hadronen und wird "confinement" genannt. Hadronen bestehen entweder aus einem Quark-/Anti-Quark-Paar (Mesonen), die eine Farb- und eine Anti-Farbladung (z.B. Rot und Anti-Rot) tragen, oder aus drei Quarks (Baryonen), deren drei Farbladungen additiv gemischt ein farbneutrales Objekt bilden.

Kernmaterie besteht aus Baryonen (Protonen und Neutronen), die bei einer Schwerionenkollision zu hohen Temperaturen und Dichten komprimiert werden. Die erzeugten Energiedichten liegen bei über  $1 \text{ GeV}/\text{fm}^3$  und somit über der Energiedichte im Inneren von Protonen. Einige Theorien erwarten, dass sich dabei die Grenzen der Hadronen für die darin enthaltenen Quarks und Gluonen auflösen und ein Zustand mit quasi-freiem Verhalten der Quarks und Gluonen im Reaktionsvolumen über einen Phasenübergang erreicht wird. Dieser Übergang in das sogenannte Quark-Gluon-Plasma (QGP) wird auch als "deconfinement" bezeichnet. Derart extreme Zustände existierten wohl nur direkt nach dem Urknall innerhalb der ersten  $\mu\text{s}$  bis die Energiedichte durch die Volumenausdehnung in den Bereich des sogenannten Hadronen Gases gesunken war. Im heutigen Universum existiert Quark-Gluon-Plasma unter Umständen im Kern von Neutronensternen oder es kann bei der Explosion schwarzer Löcher erzeugt werden.

Das in ultrarelativistischen Schwerionenkollisionen erzeugte Reaktionsvolumen, das auch "Feuerball" genannt wird, existiert nur wenige  $10^{-23} \text{ s}$  und hat eine Größe von etwa  $1.000 \text{ fm}^3$ . Durch die hohe Energiedichte ergibt sich eine sehr schnelle Expansion in das umliegende Vakuum. Zunächst stoppen die Hadronproduktion und die inelastischen Kollisionen beim sogenannten chemischen Ausfrieren (*chemical freeze-out*), danach die rein kinematischen Teilchenreaktionen beim sogenannten thermischen Ausfrieren (*thermal freeze-out*). Im Detektor können nur noch die hadronischen Endzustände dieses Feuerballs beobachtet werden. Verschiedene theoretische Modelle beschäftigen sich mit der Interpretation dieser Observablen in Bezug auf die Eigenschaften des Zustands direkt nach der Kollision. So bietet insbesondere die relative Produktion von Teilchen im Vergleich zu anderen die Möglichkeit, die Bedeutung unter-







---

dell liegt über den Werten für periphere Messungen.

Zukünftige Messungen mit Schwerionen-Strahlen mit einer Energie in der Nähe des Maximums des  $K^+$  zu  $\pi$  Verhältnisses in zentralen Pb+Pb Kollisionen an den Beschleunigern RHIC und FAIR sowie durch das NA49 Nachfolgeexperiment NA61 mit verbesserten Detektoren werden unser Verständnis von Quark Materie und dessen Reflektion in der modernen Schwerionenphysik und -theorie weiter verbessern.



# Contents

<b>1</b>	<b>Introduction</b>	<b>1</b>
1.1	Science and philosophy . . . . .	1
1.2	The hunt for quark matter . . . . .	2
1.3	NA49 results . . . . .	3
1.4	Outline . . . . .	6
<b>2</b>	<b>Theoretical descriptions of heavy ion collisions</b>	<b>9</b>
2.1	The structure of matter and the four elementary forces . . . . .	9
2.2	Standard model . . . . .	10
2.3	Quantum Chromo Dynamics . . . . .	12
2.4	The Quark Gluon Plasma . . . . .	13
2.4.1	MIT bag model . . . . .	13
2.4.2	Lattice QCD . . . . .	14
2.4.3	Phase transition . . . . .	16
2.4.4	Relation to experiment . . . . .	17
2.5	Phenomenological models . . . . .	17
2.5.1	Microscopic models . . . . .	17
2.6	Statistical models . . . . .	19
2.6.1	General features of thermodynamic models . . . . .	20
2.6.2	Superposition models . . . . .	20
2.6.3	Statistical model of the early stage . . . . .	22
<b>3</b>	<b>Experiment</b>	<b>25</b>
3.1	Accelerator and particle beam . . . . .	25
3.2	Beam detectors, target foil, and event selection . . . . .	27
3.2.1	Centrality selection . . . . .	29
3.3	Magnets and momentum determination . . . . .	33
3.4	Time projection chambers . . . . .	34
3.5	Time-of-flight detectors . . . . .	37
3.6	Data recording . . . . .	37
3.7	Data processing . . . . .	38
3.7.1	Space points . . . . .	39
3.7.2	Tracking . . . . .	39
3.7.3	Determination of track momenta . . . . .	41

<b>4</b>	<b>Particle identification</b>	<b>47</b>
4.1	Specific energy loss . . . . .	47
4.2	Determination of the specific energy loss in NA49 . . . . .	50
4.2.1	Calibration . . . . .	51
4.2.2	Calculation of the mean energy loss from cluster charges . . .	55
4.3	Kaon identification . . . . .	57
<b>5</b>	<b>Data Analysis</b>	<b>63</b>
5.1	Data sets, event and track selection . . . . .	63
5.1.1	Data sets and event selection . . . . .	63
5.1.2	Track selection . . . . .	67
5.2	Corrections . . . . .	68
5.2.1	Background correction for $h^-$ analysis . . . . .	68
5.2.2	Simulation for geometrical acceptance and track efficiency . .	71
5.2.3	Decay of kaons into muons . . . . .	73
<b>6</b>	<b>Spectra</b>	<b>79</b>
6.1	Pion . . . . .	79
6.1.1	Pion transverse momentum spectra . . . . .	79
6.1.2	Pion rapidity spectra . . . . .	82
6.1.3	Positive pions . . . . .	83
6.1.4	Systematic cross-checks and determination of systematic error	85
6.2	Kaon . . . . .	89
6.2.1	Kaon transverse momentum spectra . . . . .	89
6.2.2	Kaon rapidity spectra . . . . .	91
6.2.3	Systematic cross-checks and determination of systematic error	95
<b>7</b>	<b>Discussion</b>	<b>101</b>
7.1	Spectra characteristics . . . . .	101
7.1.1	Transverse momentum spectra . . . . .	101
7.1.2	Rapidity spectra . . . . .	106
7.2	Particle multiplicities . . . . .	109
7.2.1	Strangeness conservation . . . . .	109
7.2.2	Relative multiplicities and scaling parameters . . . . .	110
<b>8</b>	<b>Summary and Conclusion</b>	<b>123</b>
<b>A</b>	<b>Kinematics</b>	<b>125</b>
<b>B</b>	<b>Comparison to previous analysis</b>	<b>127</b>
<b>C</b>	<b>Additional plots and numerical data</b>	<b>129</b>
	<b>Bibliography</b>	<b>147</b>

<b>Curriculum Vitae</b>	<b>153</b>
<b>Erklärung</b>	<b>154</b>
<b>Acknowledgment</b>	<b>156</b>

# 1 Introduction

How is the world built up? What are things made of? Questions like these are asked by children, and even the wisest philosophers and scientists have not found the final answer. Nevertheless, our knowledge about the world grows continuously and our scientific models describe the processes in the world with increasing accuracy. One of the main topics of heavy ion physics is the inner structure of matter.

## 1.1 Science and philosophy

As early as 500 BC, greek philosophers wondered about the elementary structure of the things in the world. The theory of the *roots* of matter: water, earth, air, and fire was maintained by Empedocles (490 BC – 430 BC). The attraction between these four elements was communicated by *philia* (love) and the separation by *neikos* (strife). Empedocles also postulated as one of the first a finite velocity of light. One of his disciples was Aristotle (384 BC – 322 BC) who further developed his theory. Aristotle's beliefs became so influential (and were dogmatized by Christianity) that they were not revised until the Renaissance in the early 18th century. Democritus (460 BC – 370 BC) postulated the idea of an indivisible atom (gr. *átomos* – indivisible). It was not until the 20th century, that his idea was declared as the predecessor of modern age atomic theories. In contrast to the historical Greek writings "On Nature" that were based on philosophical thinking, modern science developed its knowledge about the world with theories based on and falsified by experiments. After the discovery of atoms, experiments like the Rutherford scattering lead to detailed models of the atom and nucleus. In the first decades of the 20th century, theories and mathematical descriptions were developed whose predictions were quite successful. Hideki Yukawa predicted the existence of mesons as the carrier particles of the strong nuclear force in 1935. This is not quite correct but the discovery of the  $\pi$  meson in 1947 earned him the Nobel prize. The discovery of more and more mesons discouraged the view of pions as elementary particles and finally lead to the development of the standard model which unifies the theories of the weak, electro-magnetic, and strong force. It describes the make up of hadronic and leptonic matter with three generations of quarks and leptons.

This model proved to be very successful in describing the results of particle accelerator experiments. However, it is known not to be complete since it does not include gravity. Figure 1.1 shows the schematics of the history of the universe.

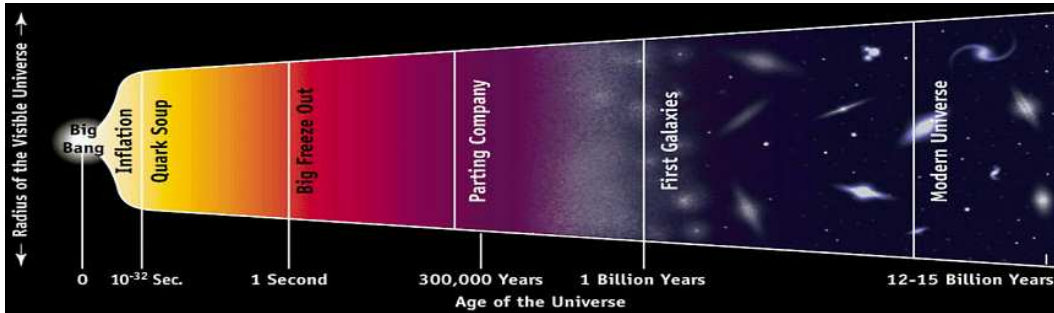


Figure 1.1: Schematic history of the universe [Han03].

## 1.2 The hunt for quark matter

Heavy-ion collisions allow to study nuclear matter at very high densities and temperature. The heaviest stable nucleus is the lead nucleus (Pb) with 208 nucleons (82 protons and 126 neutrons) whose shell structure is so-called double magic. In central collisions of two lead nuclei (Pb+Pb) at the top energy of the particle accelerator Super Proton Synchrotron (SPS) with a center of mass energy of  $\sqrt{s_{NN}} = 17.3$  GeV per nucleon pair over 2000 particles are newly produced. Silicon on silicon which is made up of 14 protons and 14 neutrons produces about 200 and proton on proton about 8 particles per collision at this center of mass energy. The energy densities in Pb+Pb collisions exceed the energy densities in normal nuclear matter by an order of magnitude. Several theoretical models predict the transition to a new state of matter – a Quark-Gluon-Plasma (QGP). Since this state of deconfined quarks and gluons is predicted to last only for about 10-20 fm which is about  $5 \cdot 10^{-23}$ s, no direct observation is possible. Indications for this state of matter have to be found in the composition of the decay products, i.e., the produced particles and their distribution in phase space. Several observables have been proposed by theoretical and phenomenological models to distinguish signatures for a quark gluon plasma: e.g., emission of hard thermal dileptons/photons [Shu78, Kaj81], enhanced strangeness production [Raf82a, Raf82b], flow [Ger86],  $J/\Psi$  suppression [Mat86, Kha94], event-by-event fluctuations [Sto94], and jet-quenching [Bai00]. Some of these models have been disproven by experimental results of the SPS heavy ion program or have been refined over the years. Recent lattice QCD calculations predict a first order phase transition for large baryonic potential ending in a critical point around  $\mu_B = 300$ -400 MeV [Kar03].

For lower baryonic potentials a cross-over region at a temperature of about 170 MeV is predicted (figure 1.2).

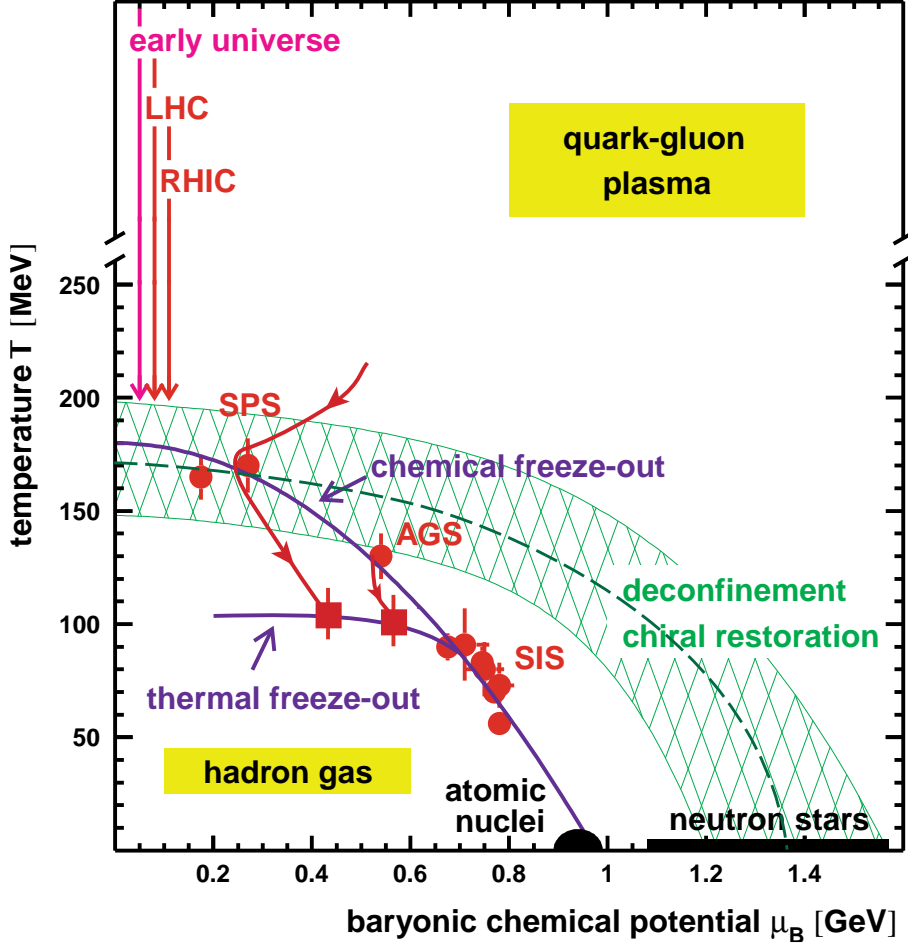


Figure 1.2: Phase diagram of strongly interacting matter showing the phase transition as calculated by lattice QCD [Hei00a].

### 1.3 NA49 results

The SPS heavy ion program has produced many results that indicate the production of a new state of matter [Hei00b]. The NA49 experiment - a large acceptance hadron spectrometer - contributed to this with intensely discussed observations. The evolution of the positively charged kaon to pion ratio with beam energy shows a non-monotonic behavior around 30 A·GeV ( $\sqrt{s_{NN}}=7.6$  GeV) laboratory momentum per nucleon in central Pb+Pb collisions (figure 1.3). The data for proton-proton interactions do not

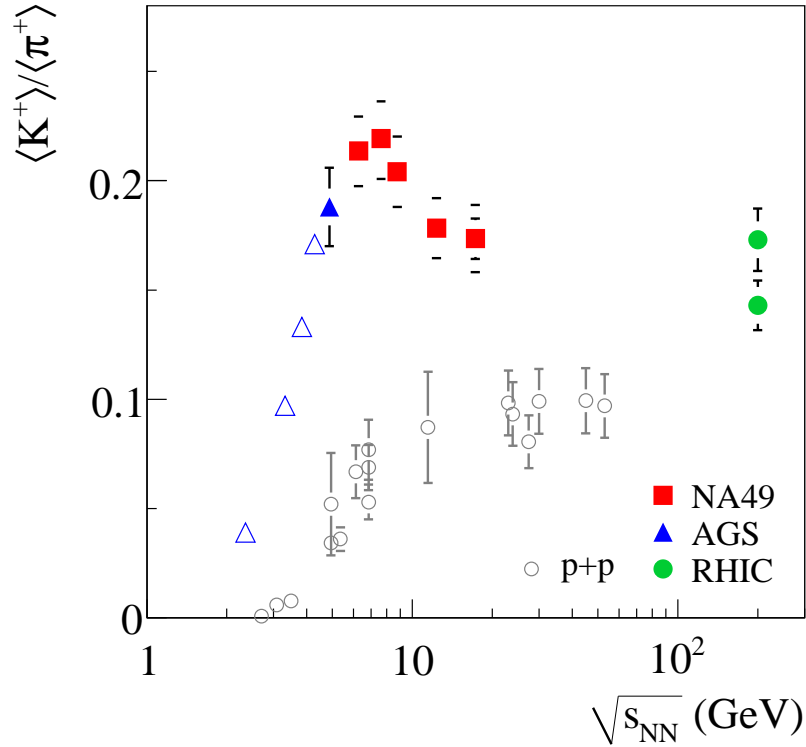


Figure 1.3: Kaon to pion ratio for central heavy ion collisions (full symbols and open triangles) and p+p interactions (open circles) versus beam energy [Gaz04].

show this behavior. However, there are few measurements of these elementary collisions in the energy region around 30 A·GeV ( $\sqrt{s_{NN}}=7.6$  GeV) and the statistical and systematic errors of the results are higher. The question that immediately arises is: "If there seems to be a phase transition to quark matter in central Pb+Pb collisions but none in proton-proton, what is the necessary system size to create an energy density high enough to create a Quark Gluon Plasma?"

First results of the system size dependence from NA49 have been shown at the Quark Matter conference in Torino 1999 [Bac99] (figure 1.4). A detailed analysis of smaller systems at the top SPS energy was published in [Alt04b]. It shows that the number of participants is not the right scaling parameter since the measurement of the central collisions of the smaller system like S+S does not connect with the trend in minimum bias Pb+Pb collisions. Alternative scaling parameters are discussed in this thesis. Figure 1.5 shows the charged kaons,  $\Lambda$ , and  $\phi$  to  $\pi$  ratios from p+p, C+C, and Si+Si as well as S+S (measured by NA35 [Alb97]) and central Pb+Pb versus the number

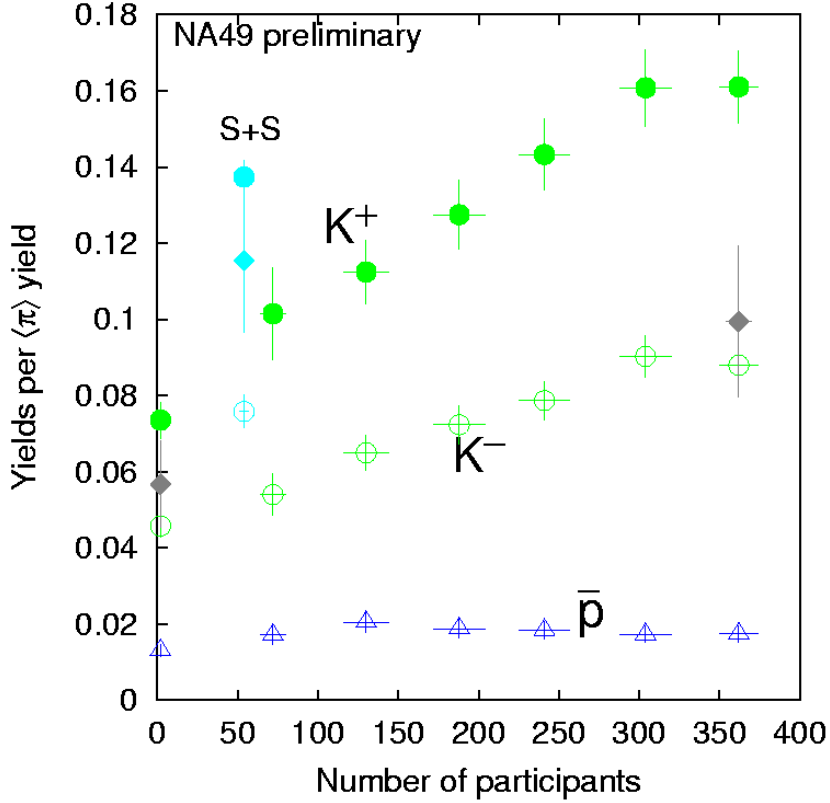


Figure 1.4: Charged kaons and anti-proton to pion ratio for centrality selected minimum bias collisions of Pb+Pb, central S+S, and p+p versus number of participants [Bac99].

of participants. It is important to take into account the differences of the compared systems which are well-studied by classical nuclear physics. First, the structure of the nuclei changes dramatically from the compact cores of light nuclei to the Pb nuclei with extended, dilute surfaces described by a Woods-Saxon potential. Second, in the context of statistical models, the effects from the increase of the reaction volume can be described by a transition from the microscopical conservation laws in p+p interactions via an intermediate canonical ensemble to a grand-canonical ensemble for central Pb+Pb collisions. This canonical strangeness suppression [Ham00, Tou02] is discussed in this thesis focusing on the right determination of relevant volume. This thesis finalizes the preliminary analysis of the data for minimum bias Pb+Pb at the top SPS energy and presents the results for minimum bias Pb+Pb collisions at 40 A·GeV ( $\sqrt{s_{NN}}=8.8$  GeV) beam energy. The lower energy lies slightly above the maximum of the kaon to pion ratio as measured in the energy scan program of central Pb+Pb collisions. The differences between minimum bias results and smaller systems are predicted to be higher than at the top SPS energy.



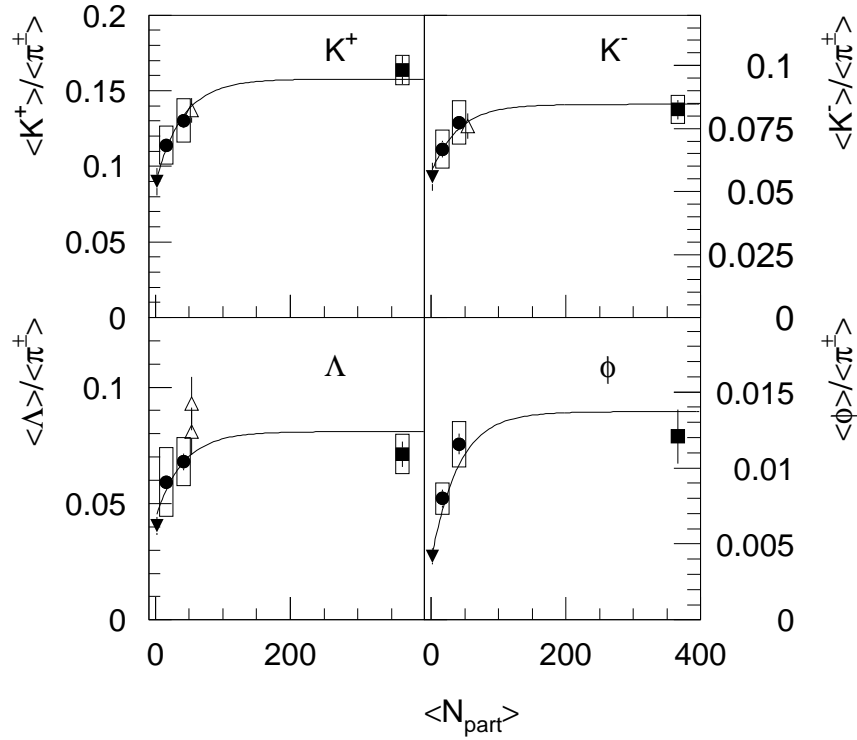


Figure 1.5: Charged kaons,  $\Lambda$ , and  $\phi$  to  $\pi$  ratio for p+p, C+C, Si+Si, S+S, and central Pb+Pb versus number of participants. The curves are shown to guide the eye and represent a functional form  $a - b \cdot \exp(-\langle N_{part} \rangle / 40)$  [Alt04b].

## 1.4 Outline

Chapter 2 gives an overview of the standard model and different theoretical models used for understanding and simulating strong interactions and heavy ion collisions. Chapter 3 describes the setup of the NA49 experiment at CERN SPS and gives an overview over data processing and reconstruction. The following chapter 4 describes particle identification via the mean energy loss of charged particles in the detector gas of the time projection chambers. Chapter 5 presents the general analysis cuts and includes a description of the simulation of the geometrical acceptance and efficiency of the NA49 main detectors. Chapter 6 explains the specific analysis methods used and the results for negative pions and charged kaons. In chapter 7, the results are discussed. By looking at relative particle production and comparing it to the results

from the smaller systems, conclusions are drawn and the implications for the different theoretical models are discussed.



## 2 Theoretical descriptions of heavy ion collisions

This chapter gives an overview of the theoretical concepts used to describe heavy ion collisions. After a short introduction about the structure of matter and the four elementary forces, the standard model and the theory of the strong force Quantum Chromodynamics (*QCD*) are described. The next sections deal with the Quark Gluon Plasma and several models to describe the confinement of quarks and gluons and the conditions necessary for a phase transition to a Quark Gluon Plasma (*QGP*). This is followed by a section on the basics of phase transitions. The final section summarizes the models most prominently used to describe heavy ion collisions.

### 2.1 The structure of matter and the four elementary forces

Figure 2.1 displays the structure of ordinary matter – from the macroscopic appearance to the inner structure of crystal lattice to molecules, atoms, and nuclei. These latter consist of protons and neutrons which are made up of three valence quarks. The electron is the only stable lepton and populates the atomic shell around the nucleus. These elementary particles interact via force-carrying bosons with the four elementary forces: strong, electromagnetic, and weak force as well as gravity. Today, the theoretical model best describing these interactions of elementary particles is the standard model. Since the inclusion of gravity has not been accomplished, the standard model does only include the strong, electromagnetic, and weak force. For the systems usually analyzed in particle physics, gravitational attraction plays no significant role as can be seen in the different relative magnitudes of coupling constants in table 2.1. If the coupling constant is well below 1, a perturbative approach can be used to solve the theoretical equations for the leading resp. next-to-leading order and neglect the following terms. Quantum Electro Dynamics (QED), the theory of the electromagnetic force, has been tested and verified up to an accuracy of  $10^{-15}$ . However, the perturbative approach for Quantum Chromo Dynamics (QCD), the fundamental theory of the

strong force, is not applicable for the observables and the momentum transfer range studied in this thesis since the coupling constant is close to unity and the following orders of the interaction cannot be neglected.

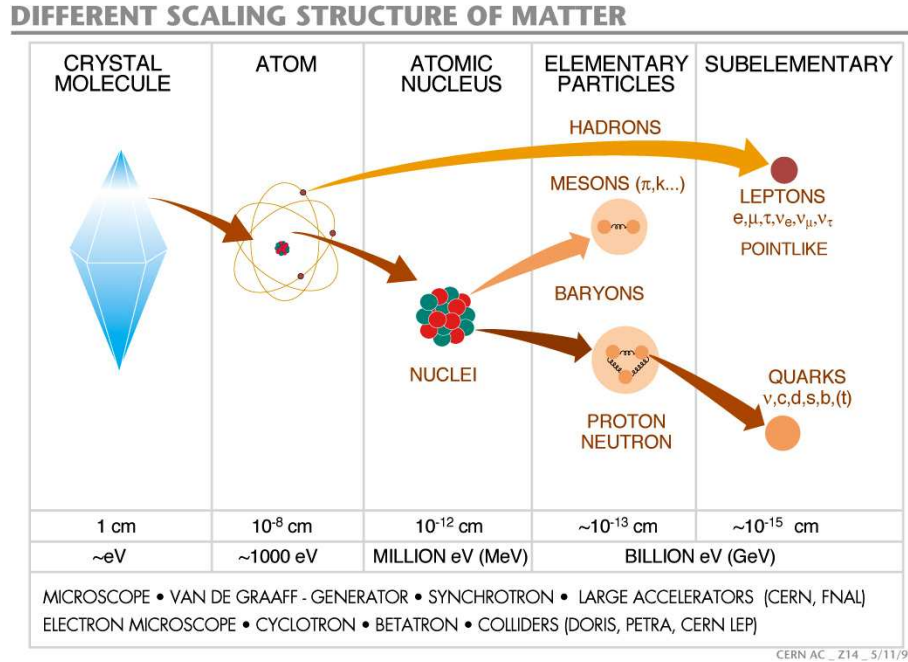


Figure 2.1: Structure of matter seen at different magnitudes of size [Cer05].

force	carrier	mass [ $GeV/c^2$ ]	typical range [ $m$ ]	coupling-constant
strong	gluons	0	$\lesssim 10^{-15}$	$\lesssim 1$
weak	$W^\pm, Z^0$	80.4, 91.2	$10^{-18}$	$10^{-5}$
electromagnetic	photon	0	$\infty$	$10^{-2}$
gravitation	graviton	0	$\infty$	$10^{-38}$

Table 2.1: The four forces, their carriers, their typical ranges and relative strength.

## 2.2 Standard model

All matter is made up from leptons and quarks. Both fundamental particle types carry spin  $\pm \frac{1}{2}$  and, therefore, obey Fermi statistics. They are made up of three generations each and every particle has its anti-particle with opposite charges. Table 2.2 displays their known characteristics. The leptons are electrons, muons, and tau, each accompanied with a neutrino type. Leptons interact via the electromagnetic and weak force.

The quark generations are made up of six flavors: up and down, charm and strange, and top and bottom (sometimes referred to as truth and beauty). The quarks are susceptible to all forces including the strong force. Therefore, in addition to the electromagnetic charge, a color charge is attributed to them. They always form color neutral objects of two or three. So far, no single color carrying particle has been observed. Two quarks form a meson with a color and anti-color carrying quark. Mesons are bosons since the individual spins of the quarks add up to whole numbers. Three quarks form baryons including the predominant protons and neutrons. Baryons are fermions and carry baryon number, which is conserved by all forces. Therefore, new baryons can only be produced together with an anti-baryon carrying a negative baryon number. The flavor of the quarks can only be changed by the weak force.

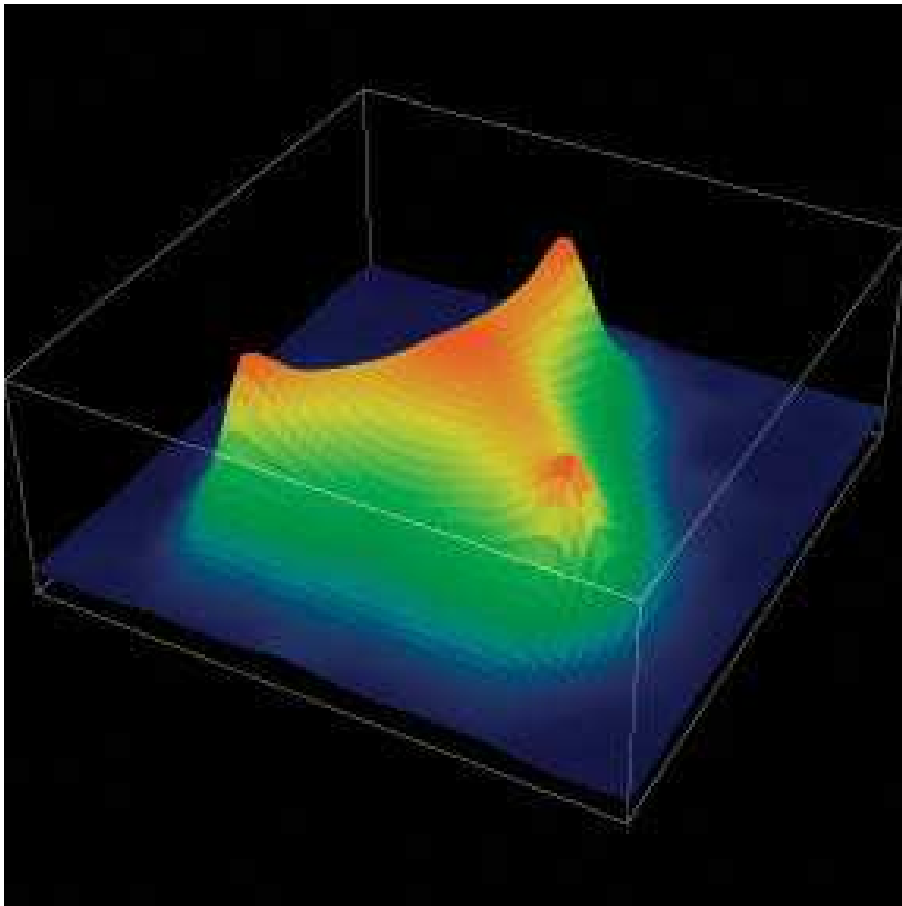


Figure 2.2: The current quarks of a baryon are visible in this presentation of the integral of the action density of a baryon [Lag04].

	Quarks		Leptons	
	up	down	electron	electron neutrino
Mass	$\approx 1.5 - 3.3 MeV$	$\approx 3.6 - 6.0 MeV$	$\approx 0.511 MeV$	$< 2.2 eV$
Charge	$+\frac{2}{3}e$	$-\frac{1}{3}e$	-1	0
	strange	charm	muon	muon neutrino
Mass	$\approx 70 - 130 MeV$	$\approx 1,3 GeV$	$\approx 106 MeV$	$< 0.17 MeV$
Charge	$+\frac{2}{3}e$	$-\frac{1}{3}e$	-1	0
	top	bottom	tau	tau neutrino
Mass	$\approx 4,2 GeV$	$\approx 171 GeV$	$\approx 1.8 GeV$	$< 15.5 MeV$
Charge	$+\frac{2}{3}e$	$-\frac{1}{3}e$	-1	0

Table 2.2: The three generations of quarks and leptons and their main characteristics.

## 2.3 Quantum Chromo Dynamics

QCD is the fundamental theory of strong interactions. The force carriers are massless gluons. There are 8 different types of gluons. Since they carry color themselves, they do also interact strongly. The consequence is a potential  $V_{QCD}$  between two quarks, which is often portrayed as following:

$$V_{QCD} = -\frac{4}{3} \frac{\alpha_s}{r} + kr \quad (2.3.1)$$

where  $\alpha_s$  is the coupling constant,  $k$  a constant factor and  $r$  the distance between the two quarks. At small distances, the QCD potential is dominated by the first term and resembles the Coulomb potential. Due to the momentum transfer respectively distance dependent coupling constant  $\alpha_s(q^2, r)$ , the quarks are in a state of asymptotic freedom within a color neutral particle. At larger distances the second term dominates and rises linearly. This leads to a peculiarity of the strong force, it gets stronger with increasing distance due to the self-interaction of the gluons. Gluons do not spread out isotropically but form a color tube often referred to as a string. If the string energy gets large enough to create a quark/anti-quark pair, it splits into this energetically more favorable state. This is the reason for the confinement of quarks in hadron, since a color charge in vacuum would have infinite energy. The distance respectively momentum transfer dependent form of the coupling constant  $\alpha_s$  is the reason why QCD problems can only be solved perturbatively at small distances or high momentum transfers (so-called hard processes). In heavy-ion collisions at the SPS, most of the particle production happens in the soft regime with low momentum transfers. There, a perturbative approach is not applicable. A numerical approximation analogous to QED perturbation theory is not possible for hadron-hadron interactions.

## 2.4 The Quark Gluon Plasma

Heavy-ion collisions are predicted to result in an initial state in which the energy densities are large enough to dissolve the individual nucleons and create a deconfined state of quarks and gluons. When the nucleons are compressed to distances so small, their individual wave-functions might merge and the quarks can move freely in the extended Quark Gluon Plasma (QGP). The following approaches estimate the energy needed to create this new state of matter.

### 2.4.1 MIT bag model

The MIT bag model [Cho74] is a phenomenological model that tries to describe confinement, e.g., by the observed characteristics of protons. It assumes the quarks to be massless particles moving freely around in a bag of a certain radius on which the vacuum exerts an effective pressure. Within the model, this vacuum pressure is a universal bag constant  $B$  for all hadrons:  $B=234 \text{ MeV fm}^{-3}$  [Won94]. Hence, a quark gluon plasma is an extended medium of quarks and gluons with a pressure exceeding the vacuum pressure. In principal, there are no limits to the extension of this quark gluon plasma whose equilibrium states can be described by thermodynamics. The characteristics of the whole system can be described by a small set of macroscopic parameters like temperature, pressure, energy, and entropy density. The equation of state (EOS) determines the relation between this parameters. The number density of particles  $n_k$  for each state  $k$  which is different for fermions (described by Fermi–Dirac  $FD$ ) and bosons (described by Bose–Einstein  $BE$ ) (see for example [Lan69]) is given by

$$n_k^{FD} = \frac{1}{e^{\frac{E_k}{T}} + 1}, n_k^{BE} = \frac{1}{e^{\frac{E_k}{T}} - 1} \quad (2.4.1)$$

with the energy of the state  $E_k$  and the temperature of the system  $T$ . The energy density can be derived by multiplying the number densities with the energy of the states and integrating over the phase space.

$$\epsilon = \frac{g}{(2\pi)^3} \int E \frac{1}{e^{\frac{E}{T}} \pm 1} d^3p \quad (2.4.2)$$

The factor  $g$  is the degeneracy of the states due to the internal degrees of freedom like



spin, color, and quark flavor, and enhances the energy density. For a gas of massless gluons and quarks, the energy density can be calculated. The assumptions of massless quarks is reasonable if one limits the quark flavors to up and down. These are the two lightest quarks with a mass well below the estimated temperature for a phase transition of about 170 MeV. The resulting energy density is

$$\epsilon = \left( \frac{7}{8}g_q + g_g \right) \frac{\pi^2}{30} T^4 \quad (2.4.3)$$

with the degeneracy of quark states  $g_q = 2 \times 2 \times 2 \times 3 = 24$  (particle/anti-particle, two flavors, each flavor has two spin and three color states) and the degeneracy of gluon states  $g_g = 8 \times 2 = 16$  (8 color states with two polarizations). The pressure can be derived in a similar approach as the energy density. Here, only the momentum components perpendicular to the surface are of importance. For an ideal gas of massless particles the pressure is one-third of the energy density as described by the equation of state  $3P = \epsilon$  [Lan69]

$$P = \frac{1}{3}\epsilon = \left( \frac{7}{8}g_q + g_g \right) \frac{\pi^2}{90} T^4 \quad (2.4.4)$$

A transition to a quark gluon plasma occurs, when the pressure exceeds the bag constant  $P = B = 234 \text{ MeV fm}^{-3} = \frac{1}{3}\epsilon$ . Therefore, the needed energy density is  $\epsilon = 702 \text{ MeV fm}^{-3}$  leading to a critical temperature of  $T = 144 \text{ MeV}$ . Just below the critical temperature, the system consists of a hadron gas composed mainly of pions. Since pions have three charge states but no spin, the degeneracy factor is only three. The energy density rises by a factor of about 10 when changing from a pion gas to a quark gluon plasma.

## 2.4.2 Lattice QCD

Analytical solutions of the QCD Lagrangian to test the possibility of a quark gluon plasma are not possible in the SPS energy region because of the coupling constant being close to unity. However, a series of stationary solutions on a small lattice in space and time can be calculated. At very small distances, the QCD potential can be calculated perturbatively. The amount of computational power needed is very large so several assumptions are made for lattice QCD calculations. Until a few years ago, lattice QCD calculations were limited to vanishing baryonic potential  $\mu_B = 0$ . Figure 2.3 indicates the order of the phase transition dependent on the assumption for

quark masses. Figure 2.4 shows the calculated dependence of  $E/T^4$  on the temperature  $T$  normalized by the critical temperature  $T_c$ .

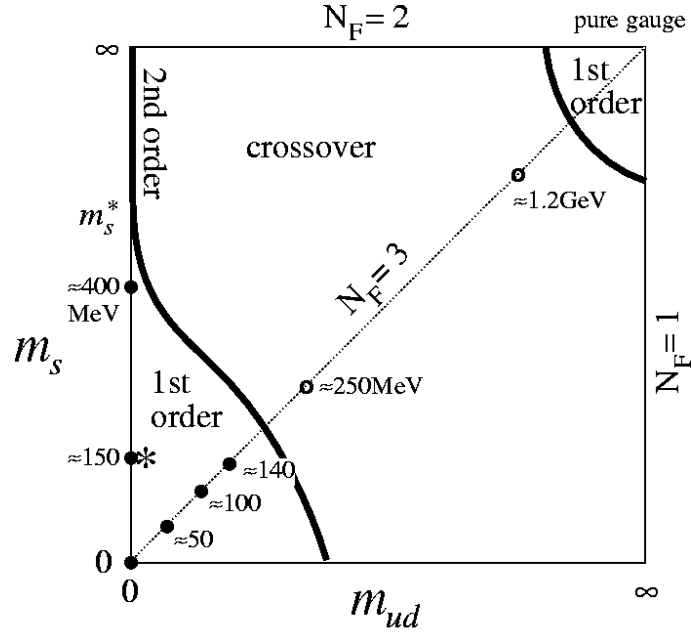


Figure 2.3: Order of the finite temperature QCD transition in the plane of light and strange quark masses [Iwa96].

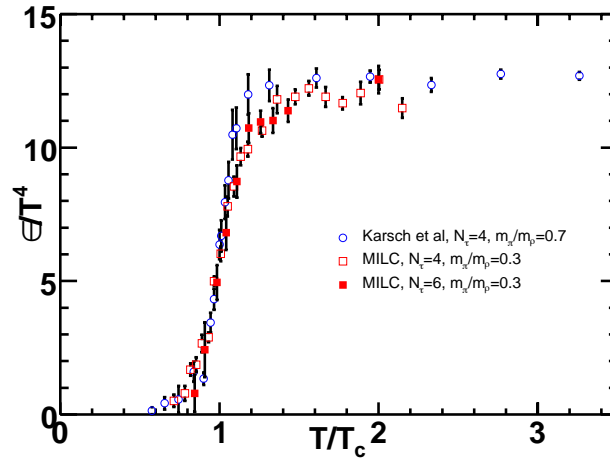


Figure 2.4:  $E/T^4$  dependence on reduced temperature  $T/T_c$  as calculated by lattice QCD [Pet06].

### 2.4.3 Phase transition

#### First order phase transition

In a first order phase transition the following conditions are met: the enthalpy  $g(p, T)$  is continuous. The entropy  $s = \left(-\frac{dg}{dT}\right)_p$  and volume  $v = \left(-\frac{dg}{dp}\right)_T$  with  $\Delta s$  equals latent heat  $c_p$  diverges. Examples are the melting of a solid state, vaporization of a liquid and sublimation of a gas as well as a phase transition from normal conductivity to super-conductivity under influence of an external magnetic field.

#### Second order phase transition

In a second order phase transition enthalpy  $g$  and its first marginals  $s$  and  $v$  are continuous.  $\left(\frac{ds}{dT}\right)_p$ ,  $\left(\frac{ds}{dp}\right)_T$ ,  $\left(\frac{dg}{dT}\right)_p$ ,  $\left(\frac{dg}{dp}\right)_T$  are non-continuous. Second order phase transitions occur in ferromagnetism, super-conducting transition without magnetic field  $H=0$ , and transition from normal fluid  ${}^4He$  to super-fluid  ${}^4He$ . They are closely linked to the critical point of the phase diagram. Since the latent heat equals zero for a second order phase transition, the medium can change phases spontaneously without additional energy. Sub-volumes can be in one or the other phase, leading to large fluctuations in the observed medium properties.

#### Crossover phase transition

In a crossover phase transition the thermodynamic variables and their derivatives show no discontinuity. However, energy and entropy densities rise more rapidly in comparison to pressure close to the critical temperature, leading to a very low velocity of sound. Crossover phase transitions are observed for example in spin studies of Fe(II)-complexes.

#### Gibb's criterion

A phase transition occurs when the pressure of one phase  $P_W$  equals the pressure of the other phase  $P_Q$  at the critical temperature  $T_C$

$$P_W(T_C) = P_Q(T_C). \quad (2.4.5)$$

### 2.4.4 Relation to experiment

The predictions of the theoretical models for the critical temperature and energy necessary for a phase transition to a quark gluon plasma can be related to experimental observables. An estimate of the energy density of heavy ion collisions can be made by measuring the transverse energy  $E_T$  produced in Pb+Pb collisions [Kan02, Bjo82]. For the top SPS energy of  $\sqrt{s_{NN}}=17.3\text{GeV}$  per nucleon, taking the initial volume to be the size of the Lorentz contracted lead nucleus, the observed transverse energy require the initial energy density of the system to be higher than  $3.2\text{ GeV}/\text{fm}^3$ . This value is well above the critical energy density as calculated in the models above. As described below in section 2.6, the temperature at the freeze-out of the system can be determined by analyzing the chemical composition of the decay particles. Statistical model fits result in temperature estimates close to the critical temperature of  $170\text{ MeV}$  [Bra99, Bra03, Bec97b].

## 2.5 Phenomenological models

The main characteristics of heavy-ion collisions and proton-proton interactions are phenomenologically well studied. They can be divided into elastic and inelastic interactions whose relation is dependent on the center of mass energy  $\sqrt{s_{NN}}$  of the collision. In the SPS energy range, the total cross-section  $\sigma_{total}$  of a nucleon-nucleon collision is about  $40\text{ mb}$ , the inelastic part  $\sigma_{inel}$  contributes about  $30\text{ mb}$ .

In principle, one can divide the phenomenological models into microscopic and statistical model approaches. Microscopic models calculate the propagation of individual particles through the system as a cascade of collisions and decays. Statistical models describe the final state of the system with a few parameters taken from the theory of thermodynamics.

### 2.5.1 Microscopic models

Microscopic models use the measured (or estimated) cross-sections of hadron-hadron interactions to predict the evolution of a collision. Particle production stems from

measured cross-sections plus string fragmentation at higher momentum transfers: here, an individual hadron-hadron collision creates a string that decays into several hadrons when the energy of the string is high enough. Since heavy-ion collisions are multi-particle systems, the calculations are complicated. Most of the microscopical models do not include a phase transition. Their results are taken as a reference of a pure hadronic scenario when comparing to experimental observations.

### Fritiof

FRITIOF [Pi92] is a string hadronic model used to simulate nucleon-nucleon as well as nucleus-nucleus collisions. FRITIOF uses different nuclear density distributions for small nucleons and heavy ions. The nuclear density functions of light nuclei ( $A < 16$ ) are approached by a harmonic oscillator model:

$$\rho(r) = \frac{4}{\pi^{3/2}d^3} \left[ 1 + \frac{A-4}{6} \left( \frac{r}{d} \right)^2 \right] e^{-r^2/d^2} \quad (2.5.1)$$

$$d^2 = \left( \frac{5}{2} - \frac{4}{A} \right)^{-1} (\langle r_{ch}^2 \rangle_A - \langle r_{ch}^2 \rangle_p) \quad (2.5.2)$$

For heavier nuclei ( $A > 16$ , i.e. for Si, Pb) FRITIOF assumes a Woods-Saxon distribution.

$$\rho(r) = \frac{\rho_0}{1 + \exp\left(\frac{r-r_0 A^{1/3}}{C}\right)} \quad (2.5.3)$$

$$r_0 = 1.16 \cdot (1 - 1.16 \cdot A^{-2/3}) \text{ fm} \quad (2.5.4)$$

The simulation of many collisions leads to a characteristic spectator energy distribution for sets of mean numbers of wounded nucleons.

### Venus

The Venus model (Very ENergetic NUClear Scattering) [Wer93] is used as an event generator in NA49 and is based on Gribov-Regge theory (GRT) and its calculated cross-sections of soft and semi-hard hadron-hadron scattering. The initial distribution of the nucleons inside the nucleus is determined by the nuclear density function. The starting point is a random impact parameter  $b$  and interactions take place if the geometrical radii  $r$  of the two nuclei overlap. The main process is a color exchange via

the formation of two strings consisting of a di-quark from one nucleon and a single quark of the other. Since the initial momentum of the quarks is not affected up to this moment, the two color-bearing parts of the string move in opposite directions and the kinematic energy is transformed into a strong color-field. If the distance is large enough, the string fragments into several quark/anti-quark pairs. This is the particle production process in string-hadronic models. If two strings or hadrons are close to each other, they fuse and their momenta and additive quantum numbers are combined. The life-time of this excited object corresponds to a known resonance if applicable, else, it is set to  $\tau = 1$  fm.

## UrQMD, HSD

UrQMD (Ultra-relativistic Quantum Molecular Dynamics) [Bas96] is a more advanced microscopic model. Interactions of secondary produced particles and decays are calculated in four-dimensional phase space. Therefore, UrQMD allows to study the evolution of the system with time. The model requires assumptions for hadronic cross-sections that have not been experimentally measured. So several input parameters are not well defined. Also, the predictions for particle multiplicities show significant deviations from measurements. The deviations are especially large for multi-strangeness carrying hyperons like  $\Xi^-$  and  $\Omega$ . HSD (hadron-string dynamics transport approach) [Ehe95, Cas99] has additional features like in-medium selfenergies and is also used to compare to experimental data.

## 2.6 Statistical models

Statistical models describe particle production in heavy ion physics as a statistical ensemble reached either by dynamical equilibration or through phase space dominance of the hadronization process. Hence, the final state is statistically defined by only a few parameters like the temperature  $T$  and the baryo-chemical potential  $\mu_B$ . The model gives no information on the individual particles and their phase-space trajectories but describes the global system properties. To relate to measured multiplicities, the models have to rely on further assumptions like the volume of the system.

### 2.6.1 General features of thermodynamic models

The possibility of the realization of a macroscopic state is defined as the ratio of the sum of all microscopic states fulfilling it to the sum of all possible micro states (both respecting the conservation laws). This sum of all realizations is called  $\Omega$ .  $S \propto \ln \Omega$  is the entropy of the system.

Grand-canonical, thermodynamical systems are fully described by a few macroscopic parameters like the total energy  $E$ , the volume  $V$ , and various potentials  $\mu$  to take the conservation laws for all conserved quantum numbers  $q_i$  into account. This approach seems suitable for heavy ion collisions. The average multiplicities for hadrons  $n_i$  can be derived by integrating the statistical distribution [Bec00]

$$\langle n_i \rangle = (2J_i + 1) \frac{V}{(2\pi)^3} \int d^3p \frac{1}{\gamma_s^{-S_i} \exp[(E_i - \mu_i q_i)/T] \pm 1} \quad (2.6.1)$$

To compare the result to observed particle multiplicities the decay products of unstable resonances have to be added. The so-called strangeness suppression factor  $\gamma_s$  is not used by all thermodynamic models. It is a phenomenological under-saturation factor implemented in the model of Becattini et al. [Bec97a, Bec97b], but not in the hadron gas model of Braun–Munzinger et al. [Bra99, Bra01] and in the model of Redlich et al. [Ham00, Tou02]. Recent approaches to define the relevant ensemble volume like the percolation model [Hoh05] or the Core-Corona model [Bec05, Aic08] describe the data without an under-saturation factor.

### 2.6.2 Superposition models

Superposition models are geometrical models based on the Glauber model [Gla70] and assume that the particle production of nucleus-nucleus collisions can be described by summing an equivalent amount of independent nucleon-nucleon collisions at the same center of mass energy like the wounded nucleon model [Bia76]. Secondary interactions of produced particles are neglected and each collision is treated independent on other reactions. All particle multiplicities are therefore proportional to the number of wounded nucleons  $N_W$ . For example the pion production is predicted as:

$$\langle \pi \rangle_{PbPb} = N_W \cdot \langle \pi \rangle_{NN} \quad (2.6.2)$$

Consequently, all particle ratios should not evolve with system size and single particle spectra like the inverse slope parameter  $T$  are predicted not to change. Experimental

data, however, show a strong evolution with system size. Nevertheless, superposition models are still used as a baseline for comparisons. The Glauber model serves as a basis for more advanced models like Fritiof and VENUS.

### Core-Corona

The Core-Corona-model [Bec05, Aic08] describes Pb+Pb collisions as a mix from almost independent nucleon-nucleon interactions (corona) and a high-density region of multiply colliding nucleons (core). While the core is predicted to have the properties of a fireball that expands collectively and produces particles according to the statistics of a grand-canonical ensemble, the corona should reflect the properties of simple nucleon-nucleon collisions. The mix between the two depends both on the system size and on the centrality of the collision. It is determined by a Glauber model calculation and the ratio  $f(\langle N_W \rangle)$  [Aic09] between the two is dependent on the centrality of the collision (see table 2.3).

Centrality	$\sigma / \sigma_{inel.}$	$f(\langle N_W \rangle)$
Bin 1	0-5.0%	0.89
Bin 2	5.0-12.5%	0.85
Bin 3	12.5-23.5%	0.80
Bin 4	23.5-33.5%	0.74
Bin 5	33.5-43.5%	0.68

Table 2.3: The ratio  $f(\langle N_W \rangle)$  between the contribution from core and corona is dependent on the centrality of the collision [Aic09]. Here, the values are shown for the centrality bins of the NA49 experiment.

Any observable  $X$  dependent on number of wounded nucleons  $N_W$  can be described as

$$X(\langle N_W \rangle) = \langle N_W \rangle (f(\langle N_W \rangle) X_{core} + (1 - f(\langle N_W \rangle)) X_{corona}) \quad (2.6.3)$$

The single nucleon-nucleon interactions contribute with the measured cross-sections from p+p and n+p collisions  $X_{corona}$ , the other with the measured cross-section from central Pb+Pb  $X_{core}$ . This approach describes the results of the centrality dependence of strangeness production at RHIC energies well [Aic08, Tim08, Bec08a]. It describes this centrality dependence without the need for a strangeness suppression factor  $\gamma_s$ .



### 2.6.3 Statistical model of the early stage

The statistical model of the early stage SMES [Gaz98] was developed close to the experimental program of NA49. It makes several assumptions about the collision system: For the volume  $V$ , it takes the Lorentz-contracted volume of an unexcited nucleus given by:

$$V = \frac{V^0}{\gamma} \text{ with } V^0 = 4\pi r_{nucleon}^3 N_W / 2 \text{ and } \gamma = \frac{\sqrt{s_{NN}}}{2m_N} \quad (2.6.4)$$

$r_{nucleon}$  is the radius and  $m_N$  the mass of a nucleon and  $N_W$  is the number of wounded nucleons. Not all of the beam energy leads to the production of new degrees of freedom. A part of the energy is carried by the net baryon number which is conserved during the collision [Gaz98]. The resulting energy available for particle production is reduced by  $\eta \approx 0.67$ :

$$E = \eta (\sqrt{s} - 2m_N) N_W \quad (2.6.5)$$

The corresponding energy density is described as follows:

$$\epsilon = (\sqrt{s} - 2m_N) \gamma = \frac{(\sqrt{s} - 2m_N) - \sqrt{s}}{m_N} \quad (2.6.6)$$

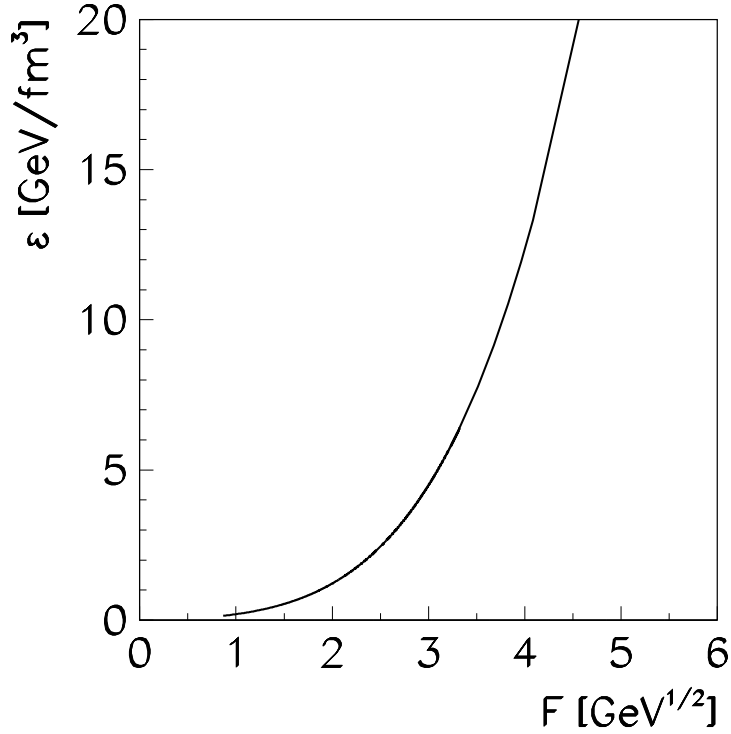


Figure 2.5: Dependence of energy density  $\epsilon$  on the collision energy formulated by using Fermi's collision energy variable [Gaz98].

Figure 2.5 shows the dependence of the energy density  $\epsilon$  on the collision energy formulated by using Fermi's collision energy variable:

$$F = \frac{(\sqrt{s} - 2m_N)^{\frac{3}{4}}}{\sqrt{s}^{\frac{1}{4}}} \approx \sqrt{s}^{\frac{1}{4}} \quad (2.6.7)$$

The SMES derives the particle content at each energy density from the equation of state. It takes the equilibrium state, which is the state with the highest entropy. On the one side, there is the QGP equation of state confined to a finite volume by vacuum pressure and, on the other, a hadron gas with its effective degrees of freedom. The phase transition occurs when the energy density is so low that the entropy in both phases is equal. The transition temperature is fixed at 200 MeV by assuming a Bag constant of 600 MeV/fm<sup>3</sup>. The energy densities for the two phases are different at equal entropy, therefore the model implies latent heat and, hence, a first order phase

transition occurs. Total strangeness and charm as well as entropy are conserved by the phase transition. The main entropy carriers are pions. Each carries about four units of entropy. Pion multiplicity per number of wounded nucleons is proportional to the entropy density  $\sigma$  scaled by the Lorentz contraction  $\gamma$  of the initial volume.

$$\frac{N(\pi)}{N_W} \propto \frac{\sigma}{\gamma} \propto \frac{g^{1/4} \epsilon^{3/4}}{\gamma} \propto g^{1/4} \frac{(\sqrt{s} - 2m_N)^{3/4}}{\sqrt{s}^{frac{1}{4}}} = g^{1/4} F \quad (2.6.8)$$

For a specific collision system, pion multiplicity is proportional to the beam energy measured by Fermi's variable  $F$ . The degeneracy factor is dependent on the number of degrees of freedom in the early state. In this model, the evolution of pion multiplicity with beam energy alone can indicate the equation of state of the initial system after the collision.

In a full model calculation the total number of strange quarks is determined by the initial state. The part of entropy carried by (massless) strange quarks  $S_s$  is

$$S_s = \frac{g_s}{g} S \quad (2.6.9)$$

with  $g_s$  the degeneracy factor of strange quarks,  $g$  the total degeneracy factor and  $S$  the total entropy. The ratio of the total number of strange quarks to total entropy (assuming  $S_s = 4N_s$ ) is given by

$$\frac{N_{s\bar{s}}}{S} = \frac{1}{4} \frac{g_s}{g} \quad (2.6.10)$$

This ratio depends only on the different degeneracy factors at high initial temperatures where the mass of the strange quark  $m_s < T$ . For a QGP this ratio would be  $\approx \frac{1}{4} \cdot 0.22$ .

# 3 Experiment

The results presented in this thesis are based on the experimental program of the NA49 collaboration. The following chapter describes the experimental facility and the setup of the experiment focusing on the main detectors. It concludes with a description of data recording and processing including the basic algorithms to analyze them.

## 3.1 Accelerator and particle beam

As a successor of the NA35 streamer chamber experiment the collaboration built the NA49 detector at the North Area experimental site of the European Organization for Nuclear Research (CERN) in Geneva. The particle beam is accelerated by the Super Proton Synchrotron (SPS), which is part of the CERN accelerator complex and has a circumference of 6.9 km (figure 3.1 and 3.2).

The NA49 detector was built to detect a large fraction of the charged hadrons produced in ultra-relativistic nucleus-nucleus collisions. It is essentially a magnetic spectrometer consisting of four big time projection chambers (TPCs) (figure 3.3). The TPCs combine the momentum determination of charged particles via the curvature of their trajectories in the magnetic field with particle identification via the specific energy loss due to ionization of the detector gas. Additional detectors measure the properties of the incoming beam, the centrality of the reaction, and the time of flight of produced particles. The main detectors are briefly described in this chapter, for a detailed description see [Afa99].

The beam of the SPS accelerator is used by several experiments in the North and West area of CERN. Prior to being injected and accelerated in the SPS, the beam passes through CERN's accelerator complex. Pb ions are pre-accelerated by the linear accelerator LINAC 3 to about 4.2 MeV per nucleon after being extracted from an ion source. A complete ionization of the Pb nuclei in an ion source is impossible due to the enormous binding energy of the inner electrons. Therefore, the accelerated Pb ions pass through so-called stripping foils. In the Coulomb field of the atoms of the



Figure 3.1: Aerial photograph of CERN. Accelerator rings are indicated by white circles [Cer91].

stripping foils the Pb ions lose their electrons until complete ionization. After the linear accelerator, the beam passes through the Proton Synchrotron Booster (PSB), which accelerates the Pb nuclei to about 500 MeV per nucleon. This is the injection energy to the Proton Synchrotron (PS), which accelerates the beam to 9 GeV per nucleon before injecting it to the SPS. Each acceleration cycle takes 15 to 20 seconds. The last two to five seconds are used for the beam extraction at the selected energy.

The highest attainable acceleration of a synchrotron depends on the bending power of its magnets and the charge to mass ratio  $Z/A$  of the ions. At the SPS, the highest attainable energy for protons is 450 GeV. For all other ions it is limited to  $Z/A \cdot 450$  A·GeV, which is further reduced to achieve higher beam intensities. The top SPS energy for Pb nuclei is 158 A·GeV. Measurements at 20, 30, 40, and 80 A·GeV beam energy were also taken within the NA49 energy scan program. Further data were taken with proton, pion, deuteron, carbon and silicon beams. Due to the requirements of other experiments the SPS accelerates proton and lead beams only. The other beams were produced by fragmenting the primary beam inside a converter target (10 mm carbon foil) upstream of the experiment. The desired fragments were selected via their charge to mass ratio. Their momenta are close to that of the primary beam. A distinction between the elements with the same  $Z/A$  is made via their Cherenkov light emission in beam detector S2. For results of the measurements of smaller collision systems see [Fis02, Afa02, Hoh03, Alt04b, Kra04, Lun04, Kli05]. Some of them are discussed together with the results of this analysis in chapter 7.

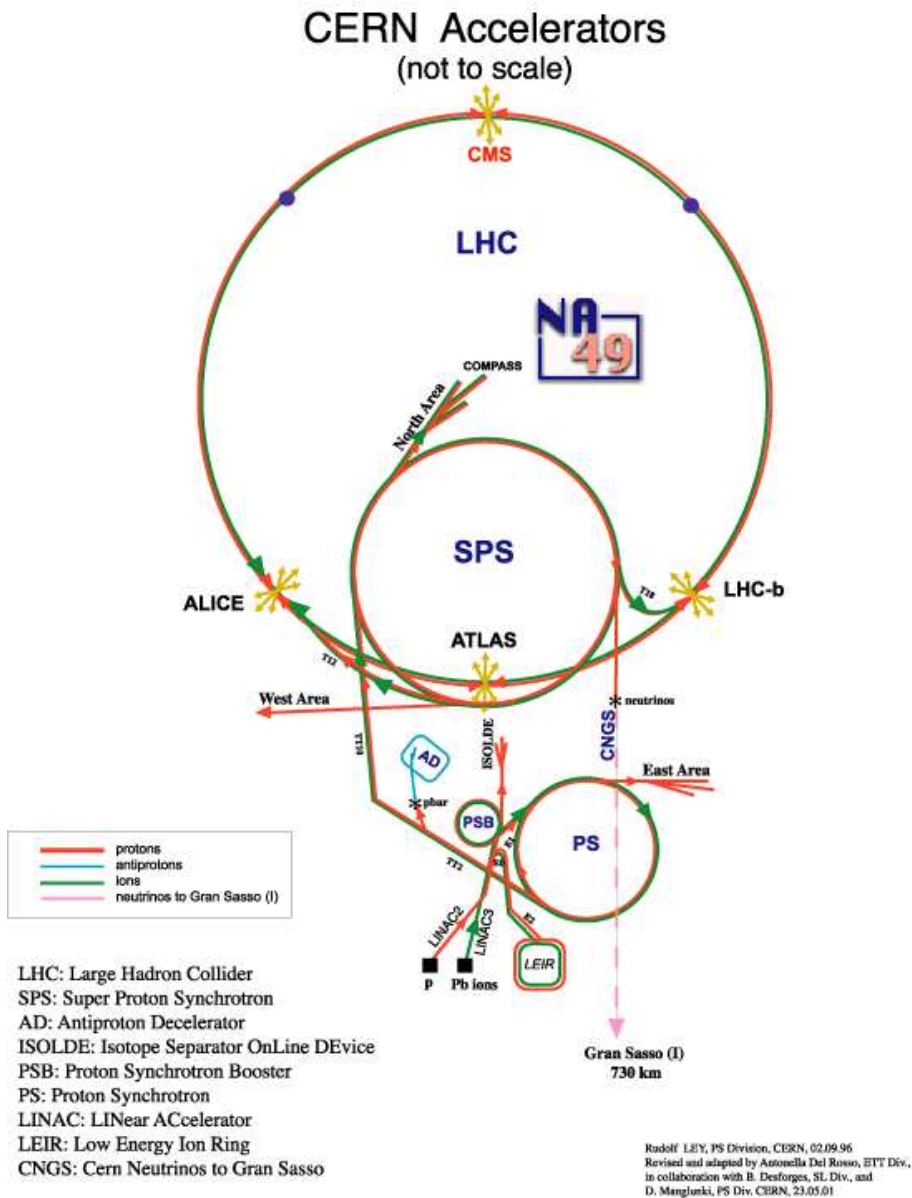


Figure 3.2: The accelerator complex of the European Organization for Nuclear Research CERN [Cer05].

### 3.2 Beam detectors, target foil, and event selection

Three beam position detectors (BPDs) are placed upstream of the target foil to determine the exact trajectory of the beam particle and especially its collision point with

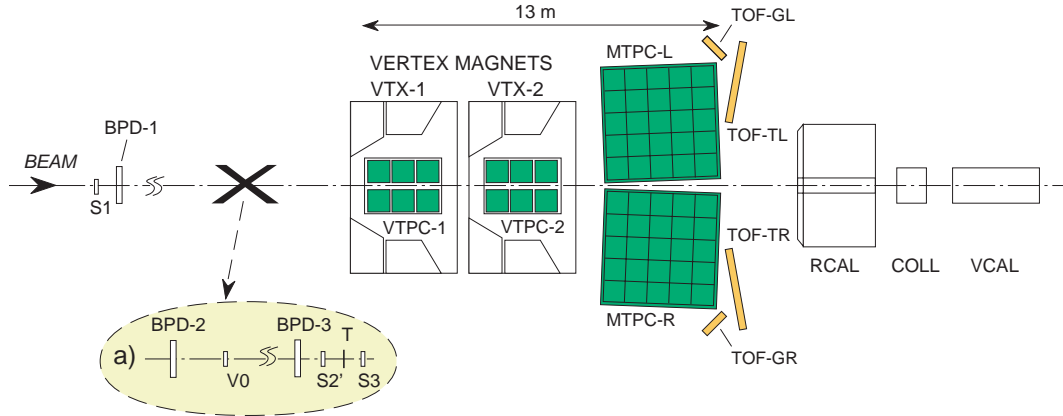


Figure 3.3: Schematic of the NA49 experiment including the target configuration for Pb+Pb collisions [Afa99].

the target foil. The BPDs are small multi-wire proportional chambers about the size of  $9 \text{ cm}^2$  and filled with a gas mixture of 80% argon and 20% methane. The first one is situated 33 m upstream the target foil, the second 10 m, and the third one 0.7 m. The extrapolation of the trajectory of the beam particle allows a determination of the collision point of the beam particle with the target to an accuracy of  $40 \mu\text{m}$  transverse to the beam. It is used as the primary vertex (BPD vertex) for the event reconstruction chain.

In general, the material of the target foil is chosen such that the reaction system is symmetric. For the reactions analyzed in this thesis it was a lead foil with natural composition of isotopes (52.4%  $^{208}\text{Pb}$ , 24.1%  $^{206}\text{Pb}$ , 22.1%  $^{207}\text{Pb}$ , and 1.4%  $^{204}\text{Pb}$ ). The thickness of the foil was  $200 \mu\text{m}$  ( $224 \text{ mg/cm}^2$ ) with a corresponding interaction probability of 0.5% for lead nuclei.

In order to reduce the recorded data volume, there are several selection criteria to determine when a valid event has occurred. The combination of three Cherenkov detectors S1, S2, and S3 as well as the zero degree calorimeter are used as event trigger. S2 is filled with a helium gas mixture and determines the charge of the beam particle to the accuracy of a few elementary charges. This distinction is needed to separate light ions with the same  $Z/A$  ratio in the case of a fragmentation beam. If a signal is detected in S1 and S2, the two detectors upstream the target foil, but no signal in the Cherenkov detector S3 after the target, the level-1 trigger criterion is met: the beam particle interacted between S2 and S3. The centrality of this reaction can be determined by measuring the energy of the projectile spectators in the zero degree calorimeter. The

spectators are made up of protons, neutrons, and light nuclei from the part of the beam particle that has not undergone a reaction (see figure 3.4). Due to the intensity of the collision the wave function of the single nucleus collapses and it fragments as a whole. However, the spectators do not undergo an inelastic collision but fly on-wards with beam energy. Besides the intrinsic energy difference to the nominal beam energy of a few hundred MeV due to the Fermi motion of the nucleons in the nuclei, the trajectories of the spectator nucleons differ by the curvature inside the magnetic field according to the charge to mass ratio of the fragment.

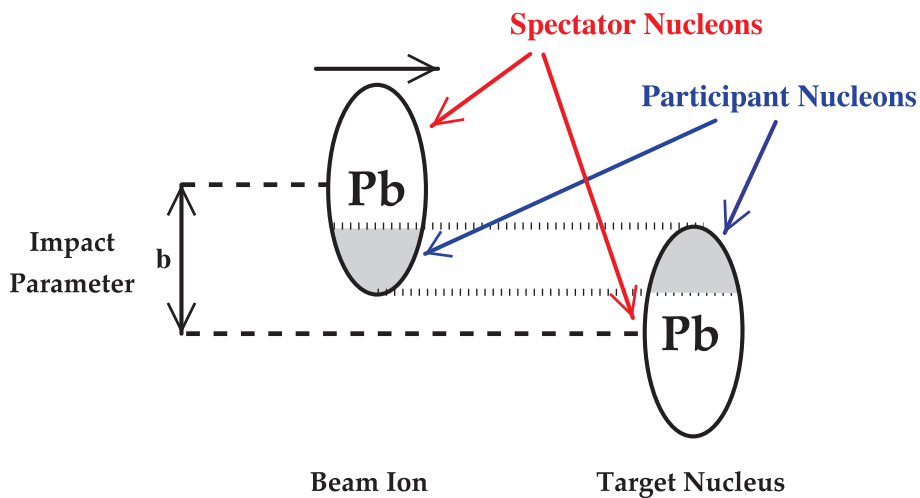


Figure 3.4: Drawing of a peripheral collision of two lead nuclei [Mit07].

### 3.2.1 Centrality selection

The zero degree calorimeter is built up of lead-scintillator and iron-scintillator layers. It is set approximately 14 m downstream of the target. A collimator allows only spectators into the calorimeter. The aperture of the collimator is adjusted for each beam energy and magnetic field, still the background from particles produced in central collisions is measurable [Coo00]. It is possible to define a maximum amount of energy deposited in the zero degree calorimeter as a trigger criterion in order to select more central events with fewer projectile spectators. Therefore the zero degree calorimeter is often referred to as veto calorimeter (VCAL).

Figure 3.5 depicts an anti-correlation of the energy deposited in the veto calorimeter  $E_{Veto}$  and the number of reconstructed tracks. This shows that the measured quantity can be used to determine the centrality of the collision. The nearly linear relation



between the veto calorimeter signal and the event multiplicity suggests that the latter is also linearly dependent on the number of wounded nucleons  $\langle N_W \rangle$ . These are all nucleons participating in the reaction. The relation of this measurement with the impact parameter of the collision requires the use of a model. The VENUS event generator [Wer93] allows to simulate the dependence of  $E_{Veto}$  on the impact parameter  $b$  [fm]. This model uses a Woods-Saxon-profile of the nuclear density distribution and produces a correlation of these quantities as in Figure 3.6. The centrality of a collision can be specified as a ratio of the reaction probability to the total inelastic cross section  $\sigma_{inel}^{tot}$ . In this analysis minimum bias data sets were taken at 40 and 158 A·GeV. This means that all inelastic reactions are recorded which fulfill the event trigger criteria. A small percentage is lost due to the S3 selection criterion.

For the two most peripheral centrality bins (bin 5 from 33.5-43.5% and bin 6 from 43.5% to trigger cutoff) a bias by the event trigger influences the  $E_{Veto}$  distribution and, hence, the selected centrality range. Figure 3.7 shows the  $E_{Veto}$  spectra for different data sets. The main deviation can be seen at the trigger cut-off of the high energies deposited which corresponds to centrality bin 6. Also for bin 5 a difference between the data sets can be observed. This results in a somewhat higher systematic error for bin 5. Since the influence of the trigger bias on the mean centrality selected and, hence, the event multiplicities cannot be fully corrected, bin 6 will not be shown in this analysis due to these uncertainties.

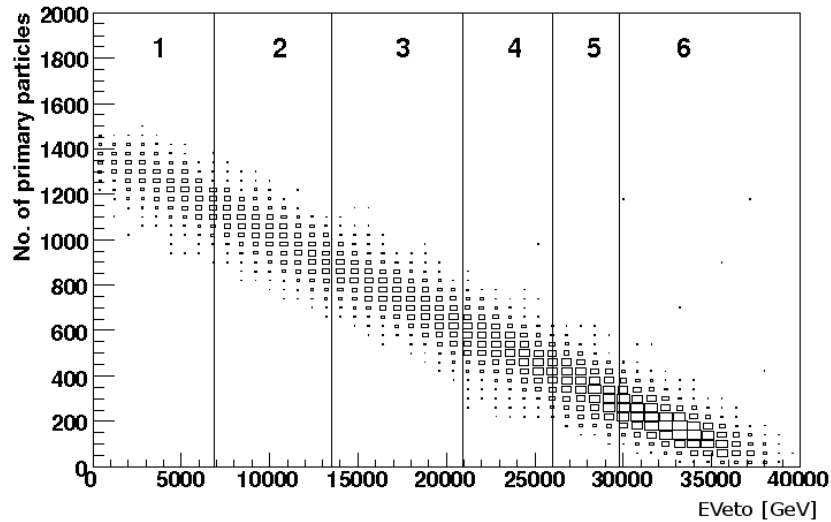


Figure 3.5: Anti-correlation of the particle multiplicity and the energy deposited in the veto calorimeter as measured in minimum bias Pb+Pb collisions at 158 A·GeV. The vertical lines indicate the limits of the centrality classes.

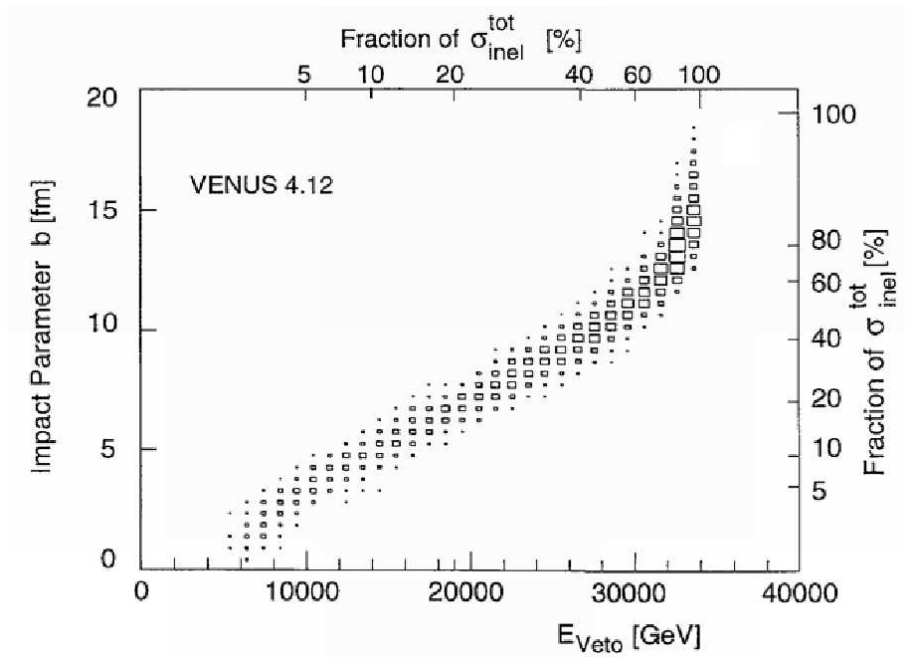


Figure 3.6: Correlation of the energy measured by the veto calorimeter and the impact parameter calculated by VENUS 4.12 [Afa99].

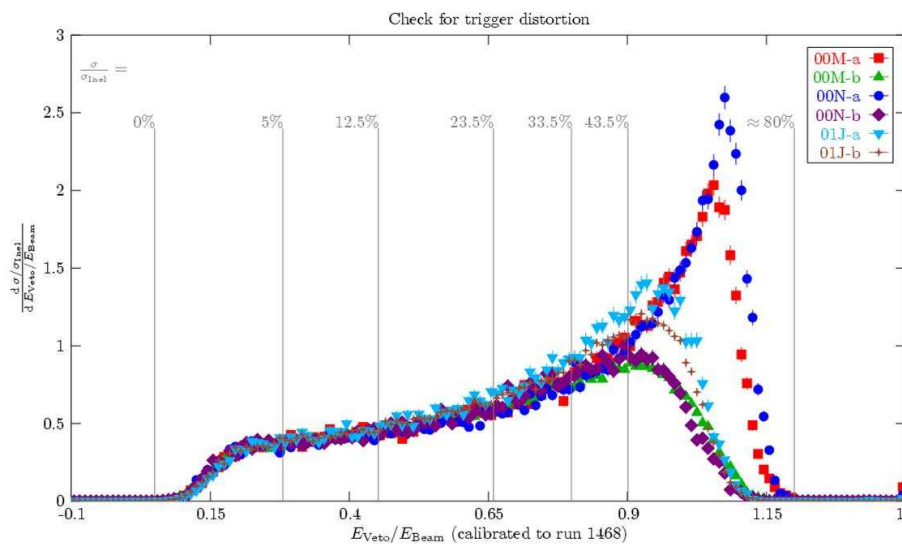


Figure 3.7: The trigger bias in  $E_{Veto}$  spectra for different data sets is clearly visible for  $E_{Veto}$  to  $E_{Beam} \approx 1$  [Las06].

A·GeV	centrality bin	$\sigma / \sigma_{inel.}$	$\langle b \rangle$ [fm]	$\langle N_{wound} \rangle$	$\langle N_{part} \rangle$
40	1	0-5.0%	2.4	351	386
	2	5.0-12.5%	4.3	290	351
	3	12.5-23.5%	6.3	210	291
	4	23.5-33.5%	8.1	142	222
	5	33.5-43.5%	9.4	93	164
158	1	0-5.0%	2.5	352	380
	2	5.0-12.5%	4.8	281	337
	3	12.5-23.5%	6.9	196	266
	4	23.5-33.5%	8.7	128	195
	5	33.5-43.5%	10.0	85	143

Table 3.1: Mean impact parameter  $b$ , mean number of wounded nucleons, and mean number of participants for different centrality bins at 40 and 158 A·GeV [Las06].

### 3.3 Magnets and momentum determination

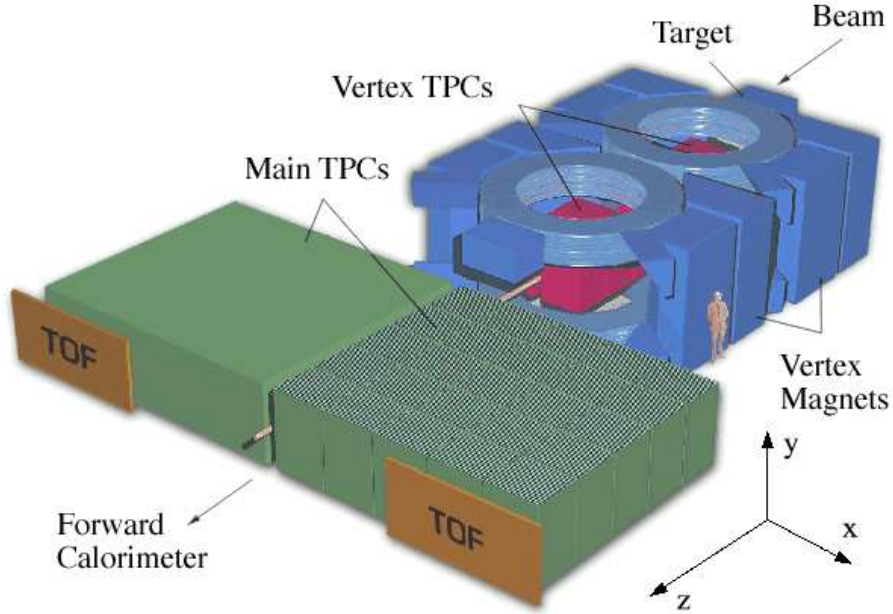


Figure 3.8: Three dimensional illustration of the NA49 experiment including the used coordinate plane.

Sign and momentum of a charged particle can be determined via the curvature of its trajectory in a magnetic field. In the NA49 experiment two super-conducting dipole magnets generate a magnetic field with a maximum bending power of 9 Tm. Inside the two vertex magnets the magnetic field is homogeneous. Thus, the momentum of singly charged particles can be calculated by measuring the radius of curvature  $r$  and the angle  $\lambda$  between the trajectory and the plane vertical to the magnetic field  $B$ :

$$p[\text{GeV}] = 0.3 \cdot q[e] \cdot B[\text{T}] \cdot r[\text{m}] \cdot \frac{1}{\cos \lambda} \quad (3.3.1)$$

The standard configuration of the magnetic field deflects positively charged particles in the positive and negatively charged particles in the negative  $x$ -direction (Figure 3.8). On the edges of the vertex magnets the magnetic field is distorted. The field lines are no longer vertical to the  $x$ -coordinate and the momentum is wrongly determined by the above formula which assumes a homogeneous field. To get a better field map of the real magnetic field a measurement with hall probes has been performed. The

magnetic field was probed in a lattice of  $4 \times 4 \times 4 \text{ cm}^3$  prior to the installation of the TPCs. The results agree within 0.5% to detailed magnetic field calculations (TOSCA) as described in [Afa99]. These calculations are used to expand the magnetic field map used for track reconstruction to regions outside of the hall probe measurements.

For the maximum bending power of 9 Tm a current of 5000 A is required in the superconducting coils. The current is kept within an accuracy of 0.01% during data taking. Measurements of permanently installed hall probes also show deviations smaller than 0.01% of the magnetic field. For lead runs at top SPS energy (158 A·GeV), the strength of the magnetic field is set to 1.5 T for vertex magnet VTX-1 and to 1.1 T for VTX-2. The current is lowered proportional to the ratio to the top energy for lower beam energies to get a similar acceptance of tracks inside the TPCs. A detailed measurement of the magnetic field for the lower energies was not possible because of the installed detectors. A calibration to an accuracy of 1% is applied using the reconstructed masses of  $\Lambda$  and  $K_s^0$ . These particles are identified via their decay topology. Their invariant mass is calculated from the masses  $m_i$  and the momenta  $\vec{p}_i$  of their daughter particles:

$$\begin{aligned}
 m_{inv} &= \sqrt{E^2 - |\vec{p}|^2} \\
 \vec{p} &= \vec{p}_1 + \vec{p}_2 \\
 E^2 &= (E_1 + E_2)^2 \quad \text{mit} \quad E_i = \sqrt{|\vec{p}_i|^2 + m_i^2}
 \end{aligned}
 \tag{3.3.2}$$

This calculation is very sensitive to systematical errors in the determination of the momenta of the decay particles. If the real magnetic field deviates from the calculated one the invariant mass is systematically shifted. At 40 A·GeV this method leads to a calibration of the magnetic field of VTX-1 by 1.4% and of VTX-2 by 1.8%. The calculated magnetic field was adjusted accordingly for the reconstruction of the tracks and their momenta.

### 3.4 Time projection chambers

The four time projection chambers (TPCs) detect the trajectories of charged particles and allow to determine their momenta via their radius of curvature inside the magnetic field. The measurement of the mean energy loss of the tracks through ionization of the detector gas provides a method for particle identification. The two vertex TPCs are installed inside the two magnets. The main TPCs are situated further downstream (see Figure 3.8). The specifications of the time projection chambers feature a good spatial resolution of the measured clusters and the requirement of using a minimal amount of material inside the sensitive volume. The spatial resolution is not only important for the momentum determination but also for the separation of close tracks. Central Pb+Pb collisions at the top SPS energy lead to track densities of up to 0.6 particles per

cm<sup>2</sup>. In order to keep the distributions of the ionization electrons of a track small a special gas mixture (Ne/CO<sub>2</sub> (90/10)) is chosen and the design of the read-out plane is adjusted relative to  $z$ -direction in order to correspond to the expected track angle. The electron diffusion is also limited by the magnetic field being parallel to the drift direction. The specifications of the time projection chambers are shown in Table 3.2.

	VTPC-1	VTPC-2	
Volume [m <sup>3</sup> ]	2 · 2.5 · 0.98	2 · 2.5 · 0.98	
Gas	Ne/CO <sub>2</sub> (90/10)	Ne/CO <sub>2</sub> (90/10)	
Sectors	6	6	
Pad rows per sector	24	24	
Pads per pad row	192	192	
Channels (pads)	27648	27648	
Pad length [mm]	16/28	28	
Pad width [mm]	3.5	3.5	
angle [°]	12-55	3-20	
MTPC-L/R			
Volume [m <sup>3</sup> ]	3,9 · 3,9 · 1,8		
Gas	Ar/CH <sub>4</sub> /CO <sub>2</sub> (90/5/5)		
Sectors	25		
Pad rows per sector	18		
Channels (pads)	63360		
sector type	HR	SR	SR'
Pads per pad row	192	128	128
Pad length [mm]	40	40	40
Pad width [mm]	3.6	5.5	5.5
angle [°]	0	0	15

Table 3.2: Characteristics of the two vertex and the main TPCs [Afa99].

The more material is situated between the target and the sensitive volume the higher is the background of secondary particles that are produced by reactions with the detector material. The time projection chambers consist therefore of a large volume, light structure box filled with gas. An epoxy frame is surrounded by two gas-tight mylar foils. The gap between the two foils is flooded with nitrogen in order to reduce contamination of the detector gas with oxygen. Inside the box a field cage of conducting mylar straps that are covered with aluminum is spanned. They define a homogeneous drift field for the ionization electrons. The mylar strips are attached to ceramic posts in the edges of the TPCs and are set to the nominal potential of the drift field at their individual position by a resistor chain. The whole apparatus hangs from an aluminum frame that holds the read-out electronics, the cooling, and the wire chambers. It serves

as the top plane of the sensitive volume.

A schematic picture shows the mode of operation (Figure 3.9). A charged particle ionizes the detector gas when traversing the TPC. The free electrons drift along the field lines of the electric field to the read-out chambers on top of the TPC. The gating grid wires are set alternately to positive and negative potential thereby shielding the read-out chamber from drifting electrons and neutralizing the detector gas. The cathode grid also referred to as 'Frisch grid' terminates the homogeneous electric field in the drift region. If the gating grid is opened the electrons drift through the cathode plane to the gas amplification plane. This plane consists of grounded  $125\ \mu\text{m}$  field wires and  $20\ \mu\text{m}$  amplification wires with positive potential. Their strong inhomogeneous, electrical field accelerates the electrons far beyond the threshold for gas ionization. Further free electrons are produced who are accelerated and ionize additional gas atoms. This gas amplification on the order of  $10^4$  produces the same amount of positively charged ions. While the knocked-out electrons are absorbed within a few nano seconds by the amplification wires the heavier and, hence, slower positive ions drift to the cathode grid within several micro seconds and induce a negative mirror charge on the pad plane that is read out by the TPC electronics.

The distance between the amplification wires and the pad plane is only 2 mm. The distribution of the induced charge spreads over several pads for each single cluster. Each sector consists of several pad rows parallel to the TPC's entry window. The pads are adjusted to the expected track angle (see Table 3.2). Their width is chosen in a way that each track induces a signal on several pads. The resulting spatial resolution is on the order of  $200\ \mu\text{m}$  orthogonal to the trajectory. In total the TPCs have 182,000 pads. Due to the strong dependence of the drift velocity and gas amplification on air pressure and temperature the TPCs are situated within acclimatized containers which hold the temperature constant on the order of  $0.1^\circ\text{C}$ . In combination with the measurement of the air pressure the variation of the drift velocity during data taking can be calculated. An independent measurement of the drift velocity shows an accuracy better than 0.1% of the calculated drift velocity [Afa99].

The electromagnetic induction on the pad plane is processed by a preamplifier and signal shaper and saved in an analog buffer every 100 ns, 512 times per event. For every charge cluster and therefore every track several samples are collected during read out. By determining the center of gravity of the charge distribution in time and using the calculated drift velocity, the  $y$ -coordinate of the charge cluster is derived. The read-out electronics are mounted together with an analog-to-digital-converter (ADC) directly on the TPCs. The ADC digitizes the measurements of several pads. The data of each sector are transmitted to the control room via fiber optic cable. The particle identification procedure via the energy loss  $dE/dx$  in the TPC gas is discussed in detail in chapter 4.

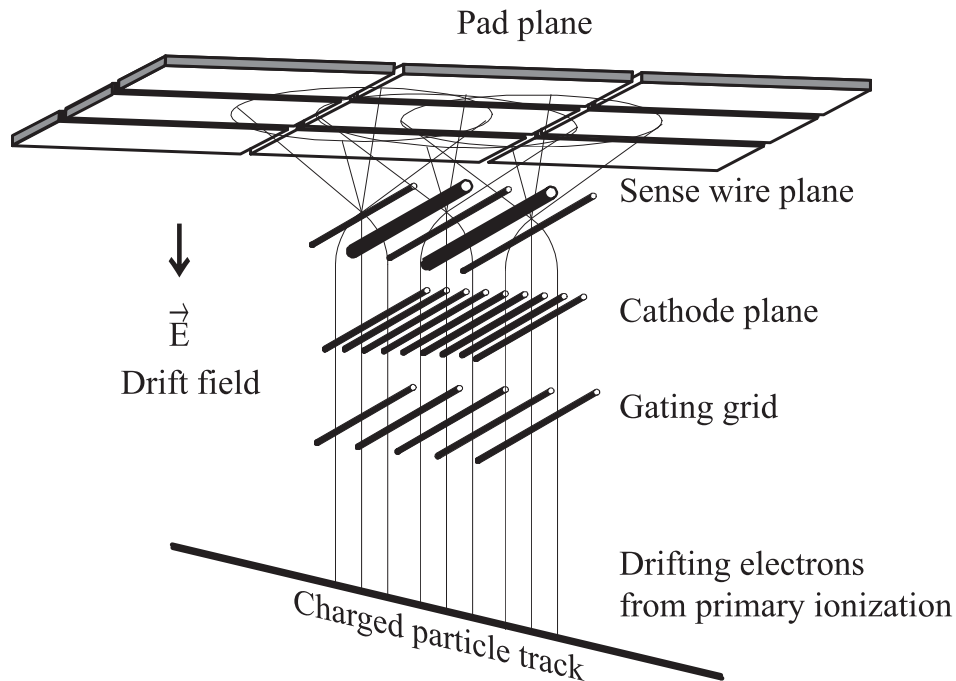


Figure 3.9: Schematic drawing of the operating mode of a time projection chamber TPC [Afa99].

### 3.5 Time-of-flight detectors

For this analysis the results from the mid-rapidity measurements of the time-of-flight (TOF) detectors play an important role. The two main detectors TOF-L1 and TOF-R1 are situated behind the two MTPCs. They expand particle identification to tracks with low momenta by measuring the flight time of a particle from the interaction through the NA49 detector. Approximate 1,000 scintillators are read out by two photo-multipliers each. The time resolution of the TOF is on the order of 60 ps. Double hits can be rejected via signal strength. Each hit is assigned to the nearest track extrapolation from the TPC. For kaon identification, the acceptance of the TOF detector is limited to a small window around center of mass rapidity in the standard setup of NA49.

### 3.6 Data recording

The event rate recorded by the experiment depends on a variety of settings and restrictions. The first factor is the availability of the SPS beam. Each acceleration cycle



(spill) takes about 15 s out of which only the last 5 s are available to extract the beam at the selected energy. The beam intensity is distributed to several SPS experiments. Typically, about 150,000 Pb nuclei per spill traverse the target foil. With a total cross-section of 0.5% and a centrality selection of 10% there are 75 potential triggers per cycle. A higher beam intensity leads to an increased probability of double events. These are reactions of succeeding beam particles during the drift time (50  $\mu$ s) of the TPC. In addition, beam particles can produce very energetic ionization electrons ( $\delta$ -electrons) which spiral in the magnetic field and contaminate the TPC measurement. To reduce the occurrence of double events and the background from  $\delta$ -electrons a low-intensity minimum bias run has been taken. Each TPC event takes 60 ms for digitizing and transmission to the receiver boards. The information from the TPC make up the largest part of the recorded. The dead time of the detector system is therefore determined by the TPC and limits the maximum number of collisions recordable during each spill to 80. For central Pb+Pb collisions the event rate is 40 to 60. The minimum bias rate is close to the detector maximum of 80.

The buffer of the receiver boards in the control room is limited to 32 measured events only. This buffer is read out by a digital signal processor which applies a zero suppression algorithm. Read-out and saving of new events cannot be done in parallel. Therefore, only some of the buffers can be emptied and reused. The full read-out of the buffer takes place during acceleration of the beam. The resulting data rate for central collisions is 28 to 30 events per spill. For minimum bias collisions it is somewhat higher due to the smaller event size.

For this analysis the minimum bias data sets at 40 (magnetic field configuration 1/4std+ and 1/4std-, 2000) and 158 A-GeV (std+ and std- 1996 as well as low beam intensity std+ 2002) were used. For each of these data sets between 300k and 400k events were recorded. A detailed compilation of the available statistics is given in section 5.1.1.

## 3.7 Data processing

The bulk part of the recorded data originates from the TPCs. Each collision leads to a raw data volume of 90 MByte (182,000 pads and 512 time bins). The used storage size on tape shrinks to 8-10 MByte by applying zero suppression. The NA49 experiment uses a special Sony tape drive with a capacity of 100 GByte per tape. Each tape can store up to 13,000 central Pb+Pb events.

The reconstruction chain processes the raw data to a data format which can be easily analyzed. The data storage system is DSPACK [Zyb95]. During reconstruction, the information of a single event is compressed to a size of only 150 kByte. The challenge of the data processing is not to discard any physics information by compressing data to a factor of 600.

The reconstruction chain uses a cluster finding algorithm to condense the recorded

charge distributions to TPC space points. These are used by the tracking algorithm to reconstruct the particle tracks. The goal is to attribute to each track the corresponding momentum, the energy loss through ionization of the detector gas, and the origin (vertex). If the track lies in the acceptance of the TOF detector, the time-of-flight is also determined.

### 3.7.1 Space points

The zero suppressed raw data written on tape have to be decoded to the right space coordinates of the NA49 detector system. Therefore, the known geometrical positions of the pads are used as a basis for the determination of the center of gravity for the  $x$  and  $z$  coordinate together with the drift time in combination with the pressure and temperature dependent drift velocity for the  $y$ -coordinate. A software algorithm (cluster finder) scans the charge information for clusters. The clusters may not be elongated over too many pads or time bins and a charge maximum is required close to their geometrical center in order to define a proper space point. These criteria are necessary to limit the background. Due to the high track density in the Vertex TPCs double clusters appear. This means that the charge distributions of two space points with a distinct charge maximum overlap. The cluster algorithm identifies these double clusters and tries to disentangle them. For each space point the mean drift time and pad position is determined and saved together with the deposited total charge for the  $dE/dx$  analysis.

The drifting electrons follow to first order only the electrical field lines of the drift field. However, there are deviations of the measured space points due to inhomogeneities of the magnetic and electric field. These deviations are strong on the edges of the Vertex TPCs where the magnetic field shows small irregularities and close to the amplification wires where the electric field is inhomogeneous. After the correction for these effects, there are still small deviations from ideal tracks, called residuals. They are on the order of  $100 \mu\text{m}$ . On the edges of TPC sectors they can amount to  $500 \mu\text{m}$ . These deviations are due to inaccuracies of the corrections and the cut-off of the measured charge distribution at sector boundaries. The residual effects are adjusted by a phenomenological approach. This correction is applied to reconstructed data after final reconstruction.

### 3.7.2 Tracking

The space points are the input to the tracking algorithm. It starts with simple track geometries to reduce the number of free space points by attributing them to tracks.

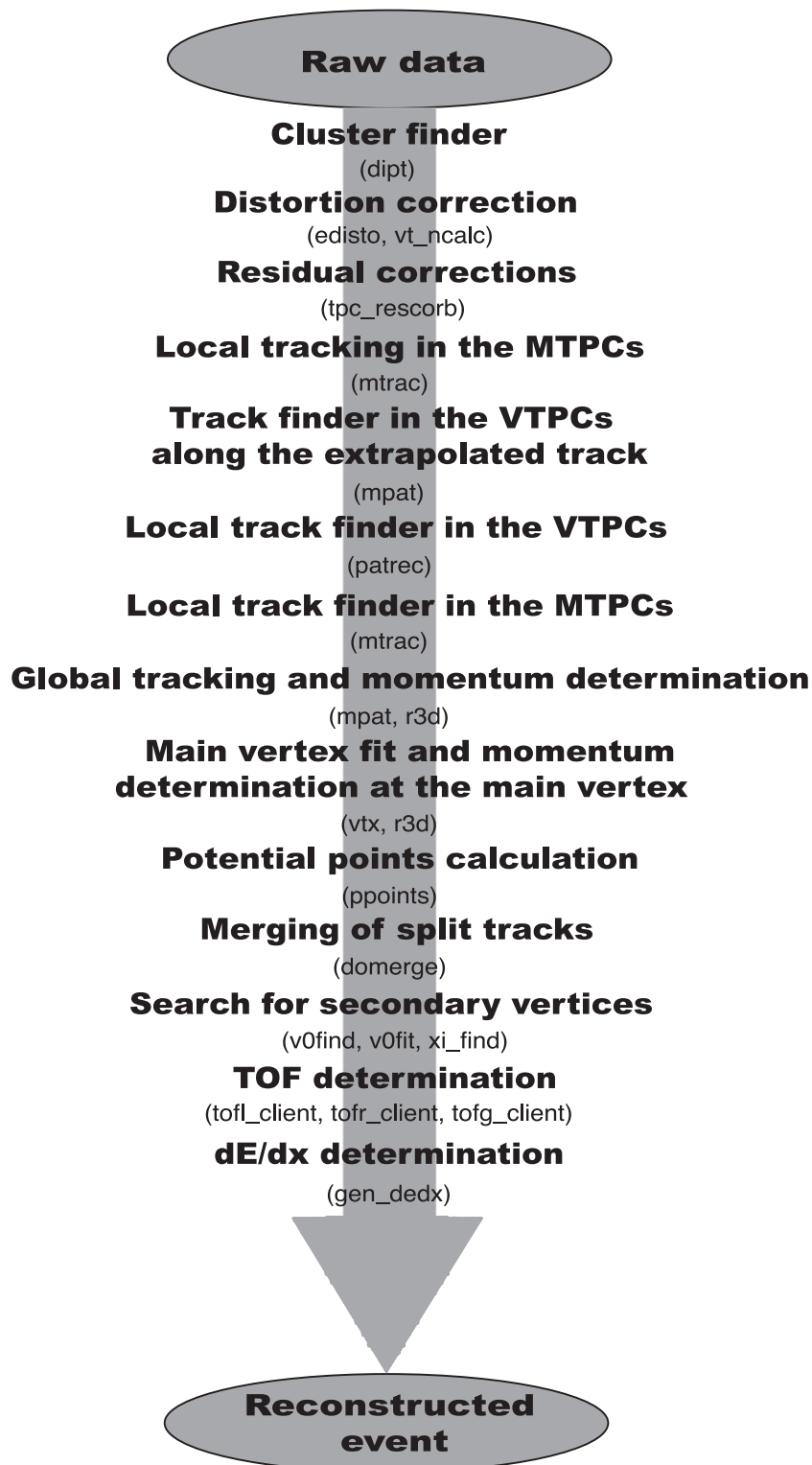


Figure 3.10: Flowchart of the NA49 reconstruction chain [Mit07].

After this, more complicated trajectories can be detected within a reasonable time. Starting point of the algorithm is therefore the MTPC. Here, the tracks are straight and the track density is lowest. These tracks are extrapolated back to the target foil taking into account the magnetic field. If they cross the target plane close-by the main vertex, all space points in VTPC-2 along the trajectory are assigned to it. If there are no space points along the extrapolated trajectory, the MTPC track is rejected and the points are released for further analysis.

From all remaining points inside VTPC-2 the tracking client joins track fragments and extrapolates them through the MTPC and back to the main vertex, assigning close-by points. If there are no track segments inside VTPC-1, also the MTPC piece of the track is discarded. Now, the VTPC-1 space points are put together and the resulting tracks are extrapolated to the MTPC. The tracking algorithm ends with a second track search inside MTPC checking also for decays with a kink.

### 3.7.3 Determination of track momenta

All detected tracks are fitted assuming they originate from the main vertex. This point is defined by the Beam Position Detectors BPDs and the  $z$ -position of the target foil. From the curvature of the magnetic field the momentum of each track is determined. Assuming that systematical deviations of the track position and the curvature are corrected or can be neglected, the relative resolution of the momentum  $dp/p$  depends on the spatial resolution ( $\Delta x$ ) of the TPC and the multiple scattering (*mult.sc.*) on the material along the trajectory.

$$\left(\frac{dp}{p}\right)^2 = \left(\frac{dp}{p}\right)_{\Delta x}^2 + \left(\frac{dp}{p}\right)_{mult.sc.}^2 \quad (3.7.1)$$

The theoretical limit of the momentum resolution can be parameterized by the Coulomb multiple scattering [Boc95]:

$$\left(\frac{dp}{p}\right)_{ms} = \frac{1.2}{\kappa \cdot |\vec{B}|} \cdot \frac{0.015}{\beta \cdot c} \cdot \sqrt{\frac{L}{X_0}} \quad (3.7.2)$$

where  $L$  is the measured track length and  $X_0$  the radiation length normalized to the density. In addition, the limited spatial resolution leads to the following momentum resolution after [Glu63]

$$\left(\frac{dp}{p}\right)_{\text{res}} = p \cdot \frac{1}{q \cdot \kappa \cdot B \cdot L} \cdot \frac{\delta_x}{l} \cdot \sqrt{\frac{K}{N+6}} \quad (3.7.3)$$

where  $p$  is the momentum of the particle,  $L$  is the traversed path in the deflection plane of the magnetic field, and  $l$  the detected track length.  $\delta_x$  is the error on the single point resolution of the pad coordinate,  $N$  is the number of measured points along the trajectory, and  $K$  is a constant factor.

From these equations one can derive that the momenta resolution at 40 A·GeV is somewhat worse due to the lower magnetic field. Figure 3.11 displays the relative momentum resolution derived from a detector simulation as a function of momentum for the magnetic field used at a beam energy of 40 A·GeV. From the formula above you can derive that the quality of the momentum resolution is dependent on the number of measured points.

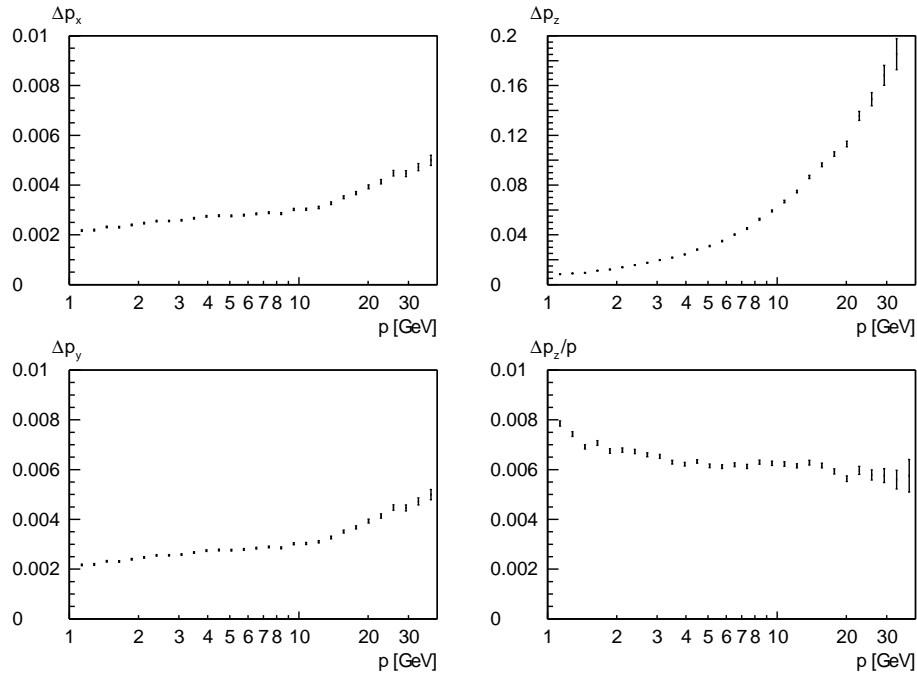


Figure 3.11: Momentum resolution as a function of momentum at 40 A·GeV [Brm01].

Figures 3.12 and 3.13 display the distribution of measured and potential points at 40 and 158 A·GeV. The dashed line indicates the number of measured points. The maxima of the potential point distribution reflects the sector boundaries of the TPCs (VTPC-1: 3x24 Pads, VTPC-2: 3x24 Pads, and MTCP: 5x18 Pads). Due to the efficiency dependence of the cluster finding algorithm on the track density, the difference of

potential and measured points is smaller at lower energies. The highest inefficiencies are seen in VTPC-1 due to the high track density.

The reconstruction chain also detects tracks that are not originating from the main vertex. These particles come from weak decays of hyperons or secondary reactions of the produced tracks with the detector material. Their first momentum fit has to be determined without a known vertex. The distance of the main vertex and the extrapolation of all tracks to the target plane defines the impact parameters  $b_x$  and  $b_y$ . The resolution of the impact parameter is on the order of a few millimeters, but it is strongly dependent on the specific track topology. A single cut on  $b_x$  and  $b_y$  for all tracks and topologies does not lead to a stable reduction of background from secondary tracks. Due to this strong dependence, the possibility of background suppression from weak decays by cutting on these parameters was rejected. Instead, the background correction for the  $h^-$  analysis is determined by the VENUS event generator. Almost all kaons are produced at the main vertex since only particles with small cross-sections like  $\Omega$  decay into kaon. Therefore, the contamination by secondary vertices is negligible and a feeddown correction is not necessary.

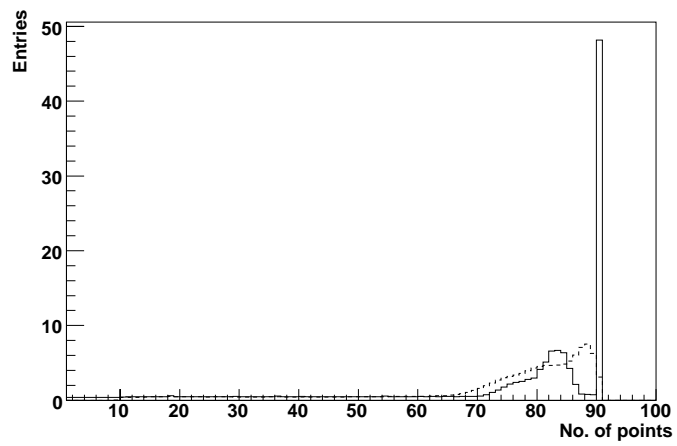
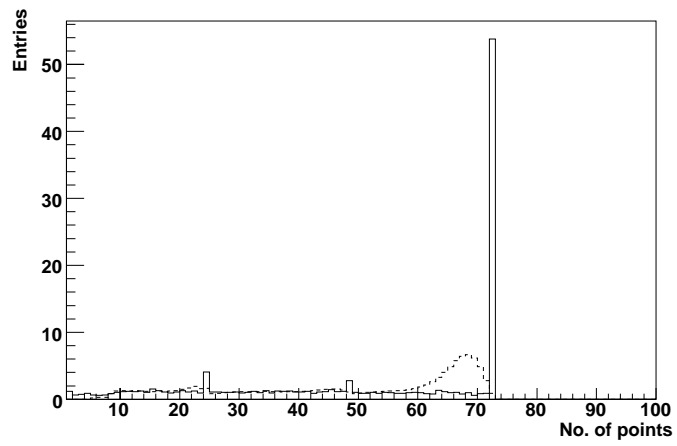
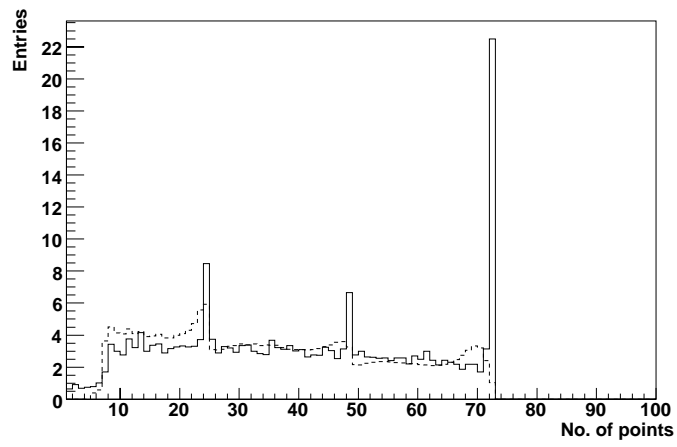


Figure 3.12: Distribution of potential (solid) and measured (dashed) number of points for 40 A·GeV for VTPC1 (top), VTPC2 (center), and MTPC (bottom).

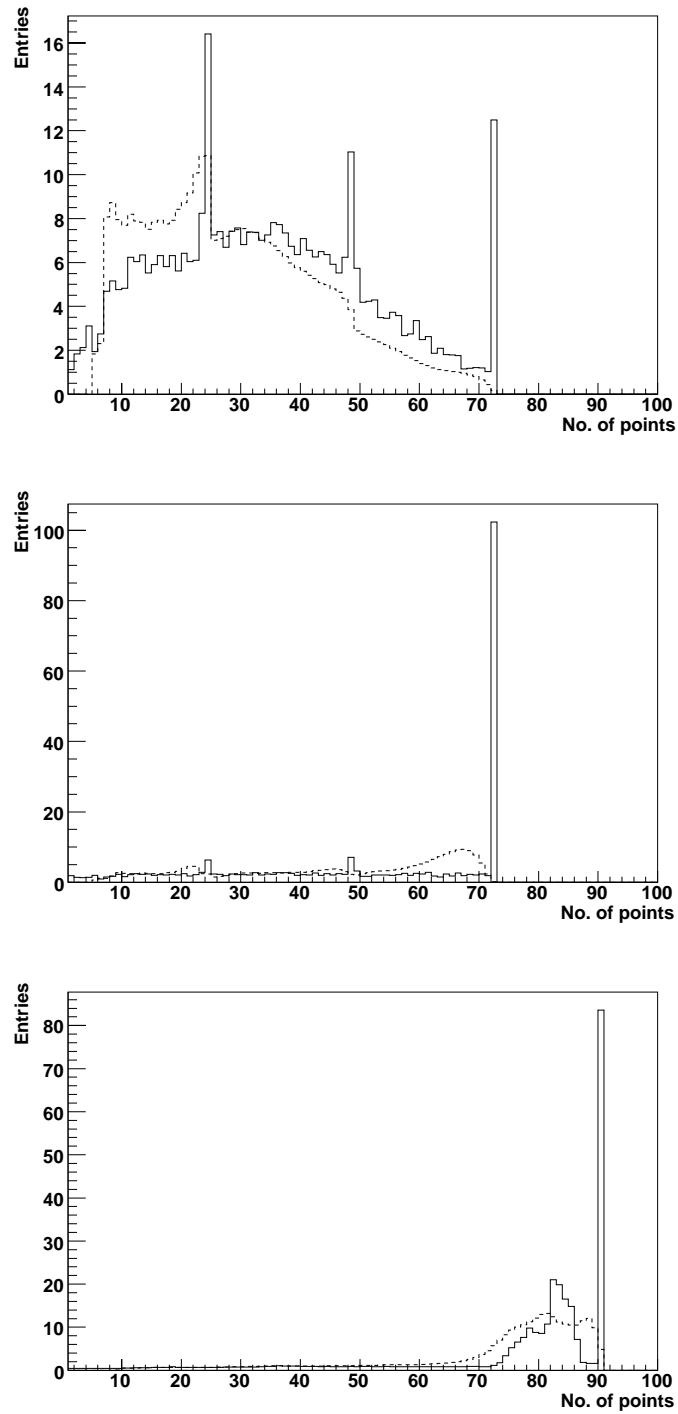


Figure 3.13: Distribution of potential (solid) and measured (dashed) number of points for 158 A-GeV for VTPC1 (top), VTPC2 (center), and MTPC (bottom).





## 4 Particle identification

In order to measure relative particle production particle identification (PID) is necessary. Kaons are identified via an analysis of the mean energy loss of the particles traversing the detector gas in the TPCs. For each of the measured track points the total deposited charge is recorded. The specific energy loss  $dE/dx$  is only dependent on the particle's velocity and the absolute value of the particle's charge (given the detector setup and additional factors assumed to be constant or corrigible for a data-taking period). Combining the determination of the charge signs and momenta of the particles, a statistical decomposition of the particle masses and, hence, types can be derived. Due to the limited  $dE/dx$  resolution and the statistical distribution of the energy loss for each measured charge cluster an individual identification for every particle is not possible. However, a probability of being a specific particle can be assigned to each track after the analysis [Rol00].

### 4.1 Specific energy loss

Charged particles ionize the detector gas while traversing the TPC. Along the track, electrons and positively charged ions are produced. Therefore, the charged particles traversing the detector suffer a specific energy loss  $dE$  per unit path length  $dx$ . The relation between the two values was calculated as a function of velocity by Bethe and Bloch [Bet30, Blo33]. Provided that the gas composition is constant and changes of temperature and pressure are controlled, the energy loss is described as the sum of momentum transfers on gas electrons by the transverse component of a cylindrical electrical field around the travelling particle. Finally the equation (often referred to as Bethe-Bloch-formula) takes the form:

$$\left\langle -\frac{dE}{dx} \right\rangle = \frac{4\pi N e^4}{m c^2} \frac{1}{\beta^2} z^2 \left( \ln \frac{2 m c^2 \beta^2}{I(1 - \beta^2)} - \beta^2 \right) \quad (4.1.1)$$

where  $N$  is the electron density of the medium,  $e$  the elementary charge,  $m c^2$  the electron mass, and  $I$  the mean ionization potential of the medium. The velocity of the particle with the charge  $z$  is given by  $\beta = v/c$  in units of  $c$ . Figure 4.1 displays the dependence of the mean energy loss normalized by the minimal energy loss on  $\beta\gamma$ . The

$1/\beta^2$  dependence at low values changes to a logarithmic rise for higher  $\beta\gamma$ . The minimal energy loss is located around  $\beta = 0.96$ . A detailed analysis of the high velocity region leads to the introduction of two additional parameters. A density correction factor  $\delta(\beta)$  takes the polarization of electrons of the detector gas into account that shields the electro magnetic field of the incoming particles [Fer40]. A maximum energy transfer  $E_{max}$  has to be implemented to exclude  $\delta$ -electrons from the determination of the specific energy loss.  $\delta$ -electrons result from direct scattering of the traversing particle and a gas electron. They carry such a high momentum that they cannot be associated with the original track.

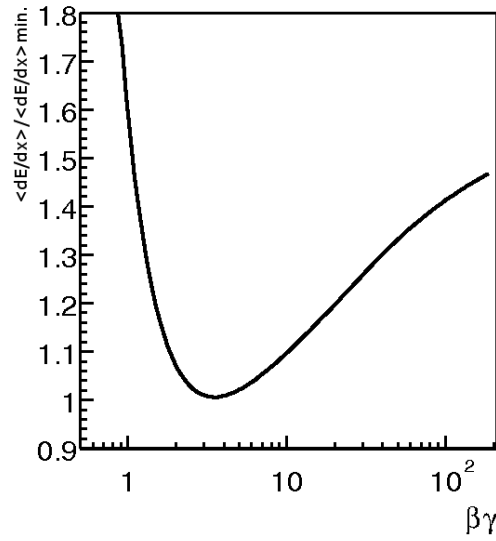


Figure 4.1: Dependence of the mean energy loss normalized by the minimal energy loss on  $\beta\gamma$ .

After introducing these two parameters the formula for the reduced mean energy loss per unit path length is given by:

$$\left\langle -\frac{dE}{dx} \right\rangle = \frac{4\pi N e^4}{mc^2} \frac{1}{\beta^2} z^2 \left( \ln \sqrt{\frac{2mc^2 \beta^2 E_{max}}{I(1-\beta^2)}} - \frac{\beta^2}{2} - \delta \frac{\beta}{2} \right) \quad (4.1.2)$$

The correction terms affect the shape of the distribution for higher velocities. Here, the specific energy loss approaches a constant value – the Fermi plateau – where the growth terms and correction factors balance each other.

The correction factor  $\delta(\beta)$  has been parameterized by Sternheimer and Peierls [Ste71]:

$$\begin{aligned} \delta &= 0 && \text{for } \beta < X_0 \\ \delta &= 2\ln(10)(\beta - X_0) + a(X_1 - \beta)^m && \text{for } X_0 < \beta < X_1 \\ \delta &= 2\ln(10)(X - X_A) && \text{for } X_1 < \beta \end{aligned}$$

where  $X_0$  and  $X_1$  represent the limits for the velocity  $\beta$  of the particle.  $X_A$  and  $a$  are dependent on the density and nuclear charge of the medium. The exponent  $m$  has been determined to be 3. For velocities bigger than  $X_1$  the Fermi plateau is reached, for velocities smaller than  $X_0$  the correction term  $\delta(\beta)$  disappears. The deviation of the actual correction from this parameterization is smaller than 2%.

The parameters that depend on the detector material have not been determined directly during the run of the NA49 experiment. Instead a phenomenological approach was applied to adjust the curve of the reduced mean energy loss per unit path length to the experimental data [Amb86]:

$$\left\langle -\frac{dE}{dx} \right\rangle = E_0 \frac{1}{\beta^2} (K + \ln(\gamma^2) - \beta^2 - \delta(\beta, X_A, a)) \equiv f_{BB}(E_0, K, X_A, a; p, i) \quad (4.1.3)$$

After fixing the four free parameters to the detector setup,  $f_{BB}$  is only dependent on the particle momentum  $p$  and type  $i, i \in (e^\pm, \pi^\pm, K^\pm, p^\pm)$ . The free parameter  $E_0$  comprehends all constant factors of the Bethe-Bloch-formula 4.1.2.  $K$  determines the shape of the curve in the region of the minimum ionization.  $X_A$  adjusts the region of the relativistic rise.  $a$  specifies the transition to the Fermi plateau. The parameters  $X_0$  and  $X_1$  of equation 4.1.4 can be determined from  $X_A$  and  $a$  assuming a smooth and continuous transition.

$$X_0 = X_A - \frac{1}{3} \sqrt{\frac{2 \ln(10)}{3a}}, X_1 = X_A + \frac{2}{3} \sqrt{\frac{2 \ln(10)}{3a}} \quad (4.1.4)$$

Figure 4.2 shows the Bethe-Bloch parameterization for electrons, pions, kaons, and protons. The energy loss is normalized to the minimum ionization  $\langle \frac{dE}{dx} \rangle_{min}$  of the Bethe-Bloch formula at  $\beta\gamma \approx 3$ .  $f_{BB}$  (equation 4.1.3) is plotted versus particle momentum, leading to different curves for the particle masses. These curves are well separated in the laboratory momentum region between  $p \approx 3 - 100$  GeV.

The resolution of  $dE/dx$  is defined by the width of the Gaussian distribution of  $dE/dx$  for pions normalized by its mean. The difference of the mean ionization of pions,

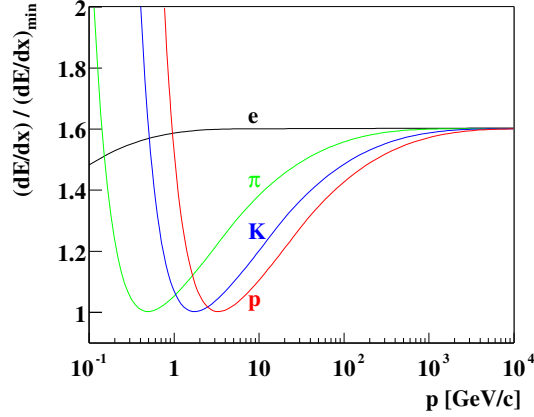


Figure 4.2: Bethe-Bloch parameterization for electrons, pions, kaons and protons.

kaons, and protons is on the order of 10%. To deconvolute the Gaussian distributions of the different particles, the experimental resolution has to be smaller. It is limited by the total cluster charge – respectively the pad length  $l_{pad}$  – and the number of pad rows which defines the maximum number of measured points  $N_{dE/dx}$ . Therefore, the maximum number of measured points lead to the following Landau distribution:

$$\frac{\sigma_{dE/dx}}{\langle -dE/dx \rangle} = A \cdot \left( \frac{\langle -dE/dx \rangle}{\langle -dE/dx \rangle_{min}} \right)^\lambda \cdot \frac{1}{N_{dE/dx}^\mu} \quad (4.1.5)$$

Analysis of the resolution for a fixed number of points and  $\langle -dE/dx \rangle$  resulted in parameters  $A = 40.5$  and  $\lambda = 0.5$  (VTTC) respective  $A = 29.5$  and  $\lambda = 0.7$  (MTTC) and  $\mu = 0.5$ . This leads to a TPC dependent maximum resolution of about 4% in the MTTCs and 6% in the VTTCs. In low density events, i.e., peripheral Pb+Pb or light-ion collisions, a combination of the  $dE/dx$  measurements from all TPCs with up to 234 measured points leads to a resolution of about 3% [Sam00].

## 4.2 Determination of the specific energy loss in NA49

In order to calculate the specific energy loss for each measured track, the cluster charge is determined first (compare section 3.4). It is assumed that the measured charge deposition is proportional to the energy loss of the particle. The cluster charge is dependent

on the detector geometry and the track angle, the pressure of the detector gas, the temperature and gas composition, the read-out electronics as well as the cluster finding model. Different corrections were implemented in the reconstruction clients `dipr`, `recharge`, and `gen_dedx`. Figure 4.3 shows the flowchart of the  $dE/dx$  determination.

### 4.2.1 Calibration

Before calculating the mean  $dE/dx$  value from the cluster charges (subsection 4.2.2), several corrections and calibrations are applied.

#### **Krypton calibration**

Differences in the amplification of the electronic channels is corrected for by calibrating the detector with the known energy of krypton decay  $^{83}\text{Kr} \rightarrow ^{83}\text{X} + e^-$ . This procedure was developed by the ALEPH collaboration [Blu89]. Radioactive krypton  $^{83}\text{Kr}$  decays inside the detector gas and the deposited energy is read-out by the electronics. The  $\beta$  decay energy is 41.55 keV. That is about a magnitude larger than the average  $dE/dx$  energy loss per pad row, so the TPC electronics have to be operated with lower amplification voltages. Therefore, only the relative amplification of the signals by the electronic channels is recorded. In addition, the signal propagation delay is determined by test pulses for each channel. This correction is applied together with the Krypton calibration when reading raw data [Moc97, Gab98].

#### **Baseline shift**

The baseline of each measurement is dependent on the subsequent tails of previous measurements due to positive feedback of the read-out electronics. This influences the ADC threshold as well as the total charge determination. It is corrected for by shifting the baseline correspondingly for each electronic channel.

#### **Hardware corrections**

The lateral cross talk effect comes from the reaction of the voltage on the amplification wires to the extraction of amplification electrons. Therefore it is strongly dependent on track density. After a short voltage dip (about 1 time bin) a RC network restores nominal voltage. This takes up to  $50 \mu\text{s}$  and affects 30 wires. The current in the amplification wires induces a signal on the read-out pads. The short voltage dip influences only the next time bin whereas the re-charge process alters the baseline. This effect has to be taken into account for up to 3 pad rows in the MTPC and was parameterized and implemented in the cluster charge reconstruction [Rol00].

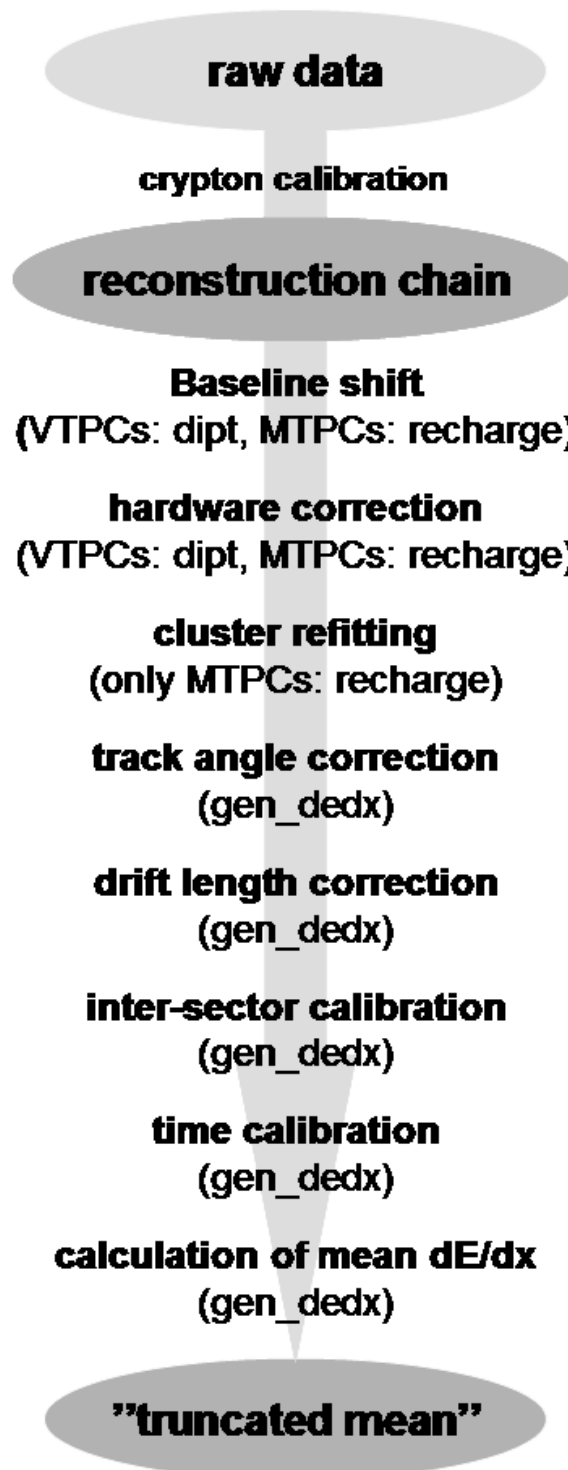


Figure 4.3: Flowchart of the determination of  $dE/dx$ .

### Pressure and temperature dependence

Due to the strong dependence of the gas amplification on the temperature  $T$  and pressure of the detector gas, the temperature is kept constant by air conditioning with an accuracy of  $\pm 0.1^\circ C$ . The air pressure is monitored and all measurements are corrected to a nominal pressure of  $p_{atmosphere} = 970$  mbar ( $\Delta p = p_{measured} - p_{atmosphere}$ ). The corrected cluster charge  $I_1$  is determined by

$$I_1 = I_{track} \cdot \frac{1}{1 - C_1^p \cdot \Delta p + C_1^p \cdot C_2^p \cdot \Delta p^2} \quad (4.2.1)$$

with  $C_1^p = 0.00328$  mbar $^{-1}$  and  $C_2^p = 0.0061$  mbar $^{-1}$ .

### Time dependence

After all corrections, there remains still a time dependence of the mean energy loss. One run out of the data set is chosen as a reference and the relative deviations of the charge deposited  $C_{jk}^{time}$  are determined for all read-out modules  $j$  in small time intervals  $k$  ( $\approx 1$  min). A detailed description of this method can be found in [Moc97]. The corrections are applied to the cluster charge in a second pass during data reconstruction.

$$I_2 = I_1 \cdot \frac{1}{C_{jk}^{time}} \quad (4.2.2)$$

### Refitting of clusters and track angle dependence

The measured distribution of ADC values is fitted by a Gaussian distribution in pad and time direction in the MTPCs. Here the track angle is small and the track density is low. At the VTTPCs a track angle dependent cluster model has to be used which has been implemented by [Ver00] for p+p data. This was not applied to the analyzed data sets due to the high track density of central Pb+Pb collisions. A first order correction is applied that corrects for the actual pad row passing length  $dx$  in dependence of the track angle.

$$I_3 = I_2 \cdot \cos \lambda \cos \Phi \quad (4.2.3)$$

$\lambda$  is the angle relative to the  $y$ - $z$  plane and  $\Phi$  the angle relative to the  $x$ - $z$  plane.

### Charge loss due to electron drift length

The contamination of the detector gas by oxygen (about 3 ppm) absorbs about 3% of the charge of the drifting electron cloud per meter drift length [Wen95]. Due to



diffusion of the electron cloud with longer drift time the tails of the distribution might fall below the ADC threshold of 5 counts. Due to the baseline shift, this effect is dependent on the total charge deposited in the detector chamber. The charge loss can be parameterized as  $C^{drift} = C^{absorb.} + const. \cdot I_{tot.}$ . The drift correction is given by

$$I_4 = I_3 \cdot \frac{1}{1 - l_{drift} \cdot C^{drift}} \quad (4.2.4)$$

where  $l_{drift}$  is the drift length. The total charge loss is about  $C^{drift} \approx 10\text{-}12\%/m$ .

### Inter-sector calibration

The krypton calibration implies the necessity for a relative calibration of the sectors at the actual amplification voltage. Different high voltage power supplies provide the current for the gas amplification in each sector. The procedure determines the mean energy loss for pions in each sector  $j$  (62 in total) originating from the main interaction vertex. Pions are chosen by selecting a narrow window around the Bethe-Bloch parameterization  $f_{BB}$  (see figure 4.2) for pions. The momentum dependence is taken into account. After several iterations the relative amplification of every read-out module is defined by  $C_j^{sec.}$  and used for calibration.

$$I_5 = I_4 \cdot \frac{1}{C_j^{sec.}} \text{ with } C_j^{sec.} = \frac{I_{meas.,j}(p, \pi)}{f_{BB}(p, \pi)} \quad (4.2.5)$$

### Adjusting Bethe-Bloch parameterization

During the process of inter-sector calibration the Bethe-Bloch function is adjusted to the measured energy loss. The adjustment is influenced by a correlation of track topology and read-out module. This effect is cancelled by building the ratio  $r_{i,j}$  of the ionization of different particles  $i, j \in (e^\pm, \pi^\pm, K^\pm, p^\pm)$  for a given momentum bin:

$$r_{i,j} = \frac{f_{BBp,i}}{f_{BBp,j}} = \frac{C_c^{sec.} \cdot \langle -\frac{dE}{dx} \rangle(p, m_i)}{C_c^{sec.} \cdot \langle -\frac{dE}{dx} \rangle(p, m_j)} \quad (4.2.6)$$

### Normalization

The measured pulse heights saved in ADC counts are normalized to the minimum ionization  $\langle -\frac{dE}{dx} \rangle_{min}$  of the Bethe-Bloch parameterization.

$$I_6 = \frac{I_5}{ADC_{min.ionization}} \quad (4.2.7)$$

## 4.2.2 Calculation of the mean energy loss from cluster charges

The specific energy loss of a particle is calculated from the ADC values for each pad row. For each track, there are several measurements in the TPCs to be averaged (about 10 to 100 clusters). The appropriate averaging method is given by the probability distribution of the single measurements. Landau [Lan44] was the first in determining the probability distribution for the energy loss of charged particles in airy absorbers:

$$F(\Delta_E) = \frac{1}{\sqrt{2\pi}} \cdot e^{-\frac{1}{2}(\Delta_E + e^{-\Delta_E})} \quad (4.2.8)$$

$\Delta_E$  is the deviation from the most probable energy loss  $\Delta E_p$  normalized to the mean energy loss  $\langle \Delta E \rangle$ :

$$\Delta_E = \frac{\Delta E - \Delta E_p}{\langle \Delta E \rangle} \quad (4.2.9)$$

For very many interactions of the charged particle with the medium, this distribution approximates a Gaussian distribution with the mean  $\langle \Delta E \rangle$ . For the NA49 setup, there are too few interactions for this approximation. The mean value is not the most probable energy loss  $\Delta E_p$ . Harder collisions lead to the characteristic tail which follows the shape of the Landau distribution (figure 4.4).

The arithmetic mean is biased by the high charge values of the harder collisions. A better approach is provided by the truncated-mean method. After rejection of some part of the tails of the distribution the arithmetic mean is calculated. This method is more stable and reduces the variance of the mean value. The resulting distribution of the truncated mean resembles a Gaussian for long tracks. The optimum for the NA49 setup is 35% of the high charge clusters and 0% for the lower tail. Figure 4.5 shows the cluster charge distribution for a MTPC track with 90 points and the determination of the truncated mean.

For tracks with a small number of measured points the mean value  $\langle \frac{dE}{dx} \rangle_{TM}$  is systematically shifted to lower charges. In this case, the weight of the tail of the Landau distribution is higher than for longer tracks. This is corrected by a phenomenological approach [Sam00]:

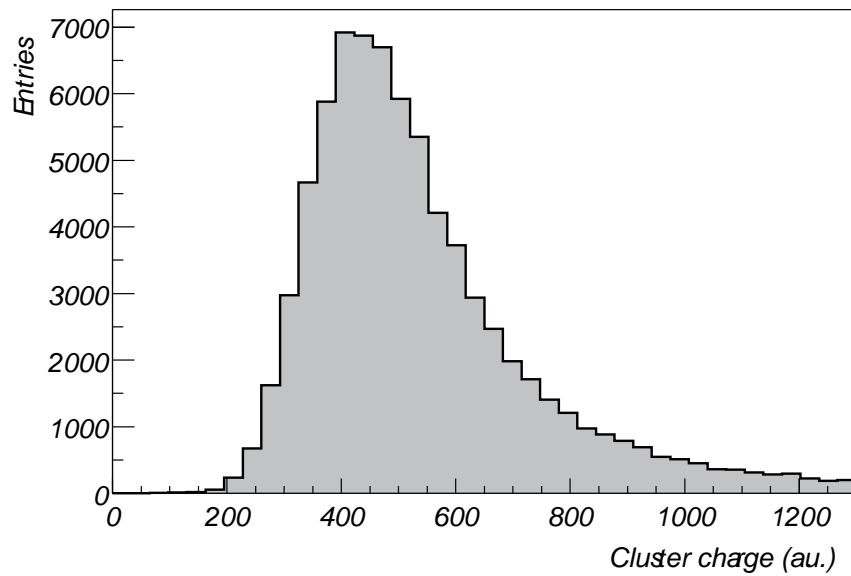


Figure 4.4: The distribution of cluster charges for tracks with a high probability of being pions at similar momentum has the shape of a Landau distribution [Kog01].

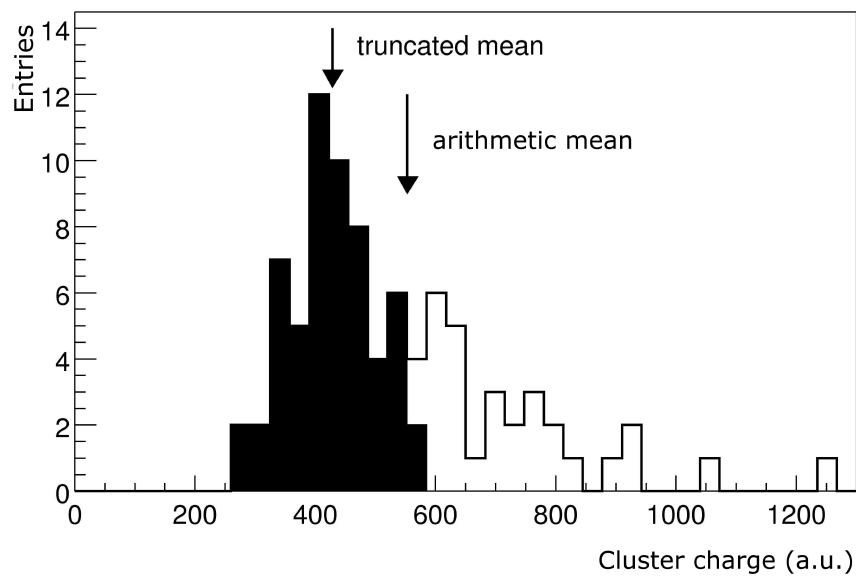


Figure 4.5: Truncated mean determination of a MTPC track with 90 points. The black area highlights the clusters used for the determination of the truncated mean [Kog01].

$$\left\langle \frac{dE}{dx} \right\rangle = \left\langle \frac{dE}{dx} \right\rangle_{TM} \cdot \left( C_A^{N_p} + C_B^{N_p} / N_{points} \right) \quad (4.2.10)$$

$N_{points}$  is the number of used measurements and  $C_A \cong 0.9965$  as well as  $C_B \cong 0.25$  are derived from the observed shift. Short tracks are mainly low momentum tracks in VTPC-1 which are bent out of the sensitive volume by the magnetic field. Finally, the mean energy loss calculated in ADC units is normalized to unity for minimum ionizing particles  $\left\langle -\frac{dE}{dx} \right\rangle_{min} = 1$ .

The  $dE/dx$  value is calculated for each particle separately in each TPC. A combination of these values should be favorable for tracks that cross all TPCs. The higher number of points should decrease the fluctuations of the mean value. Since the TPC gas mixtures are different and therefore the Bethe-Bloch parameterizations, no common truncated mean method for all space points can be applied. [Sam00] developed a procedure to normalize the different TPC measurements to a global Bethe-Bloch parameterization. However, the calculation of the global  $dE/dx$  did not improve the  $dE/dx$  resolution for high density regions. In central Pb+Pb collisions, the quality of VTPC-1 points is bad. This is due to merged cluster caused by the high track density. An inclusion of these points for the  $dE/dx$  analysis of MTPC tracks worsens the resolution. Only in proton-proton and peripheral Pb+Pb collisions, the global calculation of  $dE/dx$  leads to improvements [Sik00]. In the present analysis, local  $dE/dx$  information of the MTPC was used to identify kaons.

### 4.3 Kaon identification

After applying the track cuts specified in the previous chapter, the tracks are filled in a  $dE/dx$  container. This is a class to store the truncated mean and the number of points distributions for 20 logarithmic total (from 0 to 2 – bin width = 0.1) and 20 transverse momentum (from 0.0 to 2.0 GeV – bin width = 0.1 GeV) bins as well as for the two opposite charges. All bins are fitted by the  $dE/dx$  analysis function which is the sum of five asymmetric Gaussians.

$$f(x; C, x_0, \sigma, \delta) = \left\{ \frac{C}{\sigma\sqrt{2\pi}} \exp\left(-\frac{1}{2} \frac{x - x_0}{(1 + \delta)\sigma}\right) \right\} \text{ for } x > x_0 \quad (4.3.1)$$

Each Gaussian represents one of the observed particle species - electrons, pions, kaons, protons, and deuterons. The asymmetry parameter  $\delta$  is the same for all particle species.

It is fixed to the average value of the fitted asymmetry parameter of the analysis of central collisions [Lee03]. The contribution of varying fixed asymmetry parameters to the systematic error of the analysis will be discussed in section 6.2.3. The width of the  $dE/dx$  peak for each species varies with the position scaled by an exponent  $\alpha = 0.625$

$$\sigma_i = \sigma x_i^\alpha. \quad (4.3.2)$$

The width is further dependent on the number of clusters on each track. The mean number  $l$  was recorded for each bin leading to a scaling factor of  $\sqrt{l}$  and the following function for each particle species:

$$g_i(x; A_i, x_i, \delta, \sigma, \alpha) = A_i \sum_l l \frac{n_l}{N_{tot}} \exp - \frac{1}{2} \left( \frac{x - x_i}{(1 \pm \delta)\sigma_{i,l}} \right)^2, \text{ with } \sigma_{i,l} = \frac{\sigma x_i^\alpha}{\sqrt{l}} \quad (4.3.3)$$

The parameterization of the  $dE/dx$  distribution has in total 12 parameters. The width  $\sigma$ , the asymmetry parameter  $\delta$ , and five positions and amplitudes for the different particle species. Since particle multiplicities vary for the bins, being close to zero for certain particle species, it is impossible to accurately determine all of these parameters in each bin. Several findings in well populated total momentum bins for the transverse momentum distribution are therefore extrapolated to full phase-space to constrain the fits. The relative position of the kaon, proton, and deuteron peak relative to the pion peak does not vary with transverse momentum  $p_T$ . Also, the asymmetry parameter  $\delta$  is held constant with  $p_T$ . It is assumed that these values are the same for negative and positive particles.

Figure 4.6 show the  $dE/dx$  spectra for negative particles for two total momentum bins from 10.0 GeV to 12.6 GeV (left) and from 31.6 GeV to 39.8 GeV (right) and a transverse momentum of 0.5 to 0.6 GeV at 158 A·GeV for centrality bin 1. The separate Gaussians for kaons (green line) and pions (red line) can be nicely seen. The anti-proton (blue line) contribution is small relative to the kaons.

For positive particles the proton contribution relative to the kaons is much higher. For larger total momentum the proton peak dominates and the relative kaon yield is strongly dependent on the fit (figure 4.7).

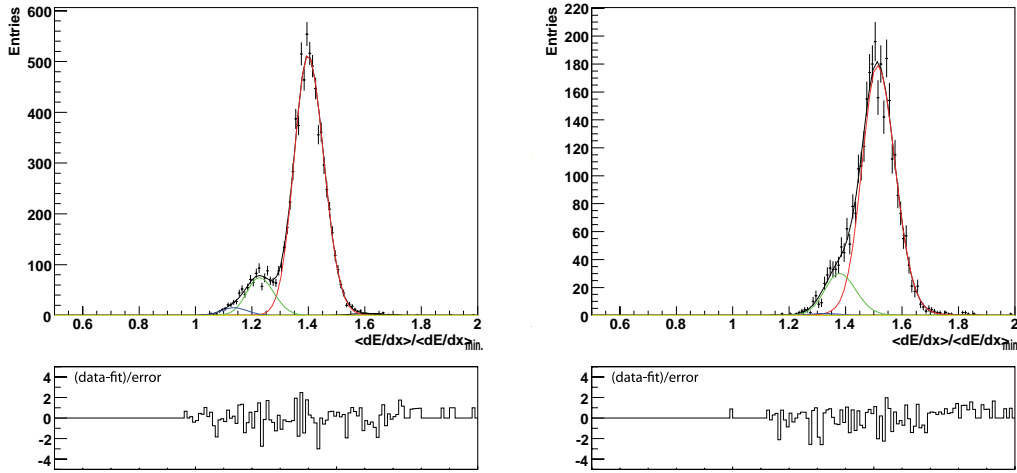


Figure 4.6:  $dE/dx$  spectra for negative particles for two total momentum bins from  $10.0 \text{ GeV} < p_{tot} < 12.6 \text{ GeV}$  (left) and from  $31.6 \text{ GeV} < p_{tot} < 39.8 \text{ GeV}$  (right) and a transverse momentum of  $0.5 < p_t < 0.6 \text{ GeV}$  at  $158 \text{ A}\cdot\text{GeV}$  for centrality bin 1.

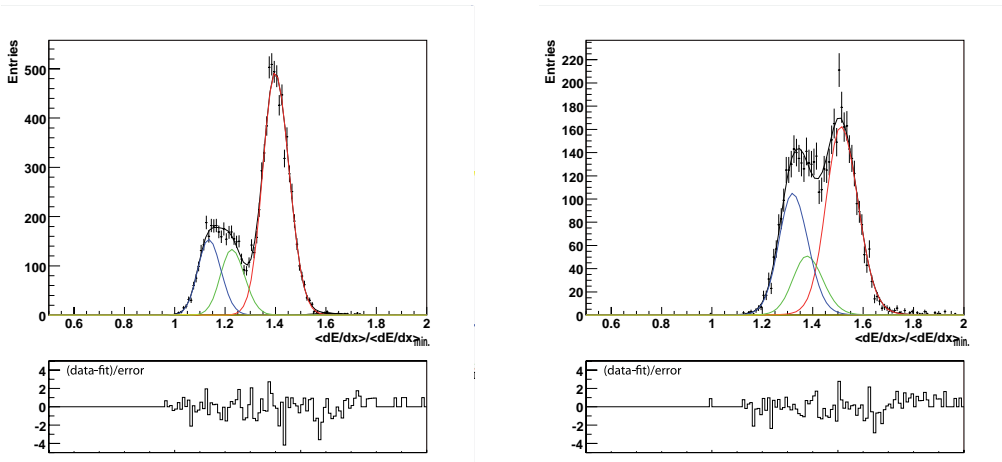


Figure 4.7:  $dE/dx$  spectra for positive particles for two total momentum bins from  $10.0 \text{ GeV} < p_{tot} < 12.6 \text{ GeV}$  (left) and from  $31.6 \text{ GeV} < p_{tot} < 39.8 \text{ GeV}$  (right) and a transverse momentum of  $0.5 < p_t < 0.6 \text{ GeV}$  at  $158 \text{ A}\cdot\text{GeV}$  for centrality bin 1.

For less central collisions (and for lower beam energies) the track density is lower and the  $dE/dx$  resolution is better. Figure 4.8 shows two spectra at the same total

momentum as above.

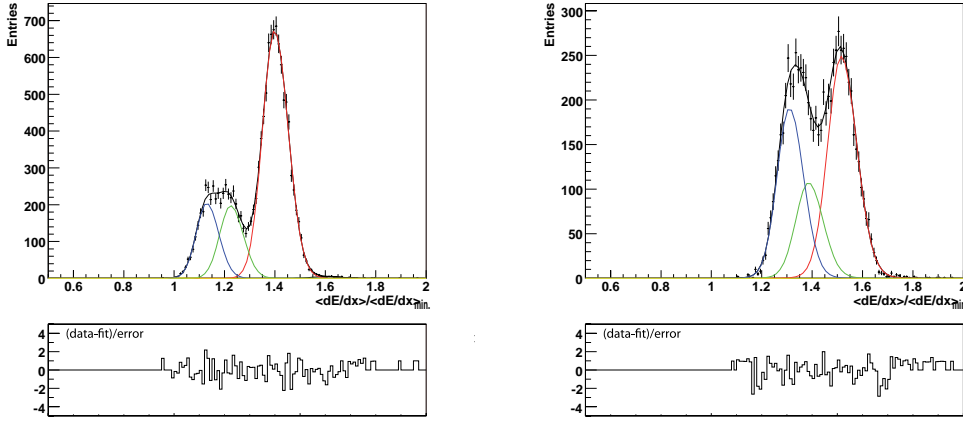


Figure 4.8:  $dE/dx$  spectra for positive particles for two total momentum bins from  $10.0 \text{ GeV} < p_{tot} < 12.6 \text{ GeV}$  (left) and from  $31.6 \text{ GeV} < p_{tot} < 39.8 \text{ GeV}$  (right) and a transverse momentum of  $0.5 < p_t < 0.6 \text{ GeV}$  at  $158 \text{ A}\cdot\text{GeV}$  for centrality bin 1.

The fitted position for the particles relative to the Bethe-Bloch-parameterization allows for a cross-check if the fit to the observed data follows the assumptions (see figure 4.9 for  $158 \text{ A}\cdot\text{GeV}$  and figure 4.10 for  $40 \text{ A}\cdot\text{GeV}$  for centrality bins 1, 3, and 5).

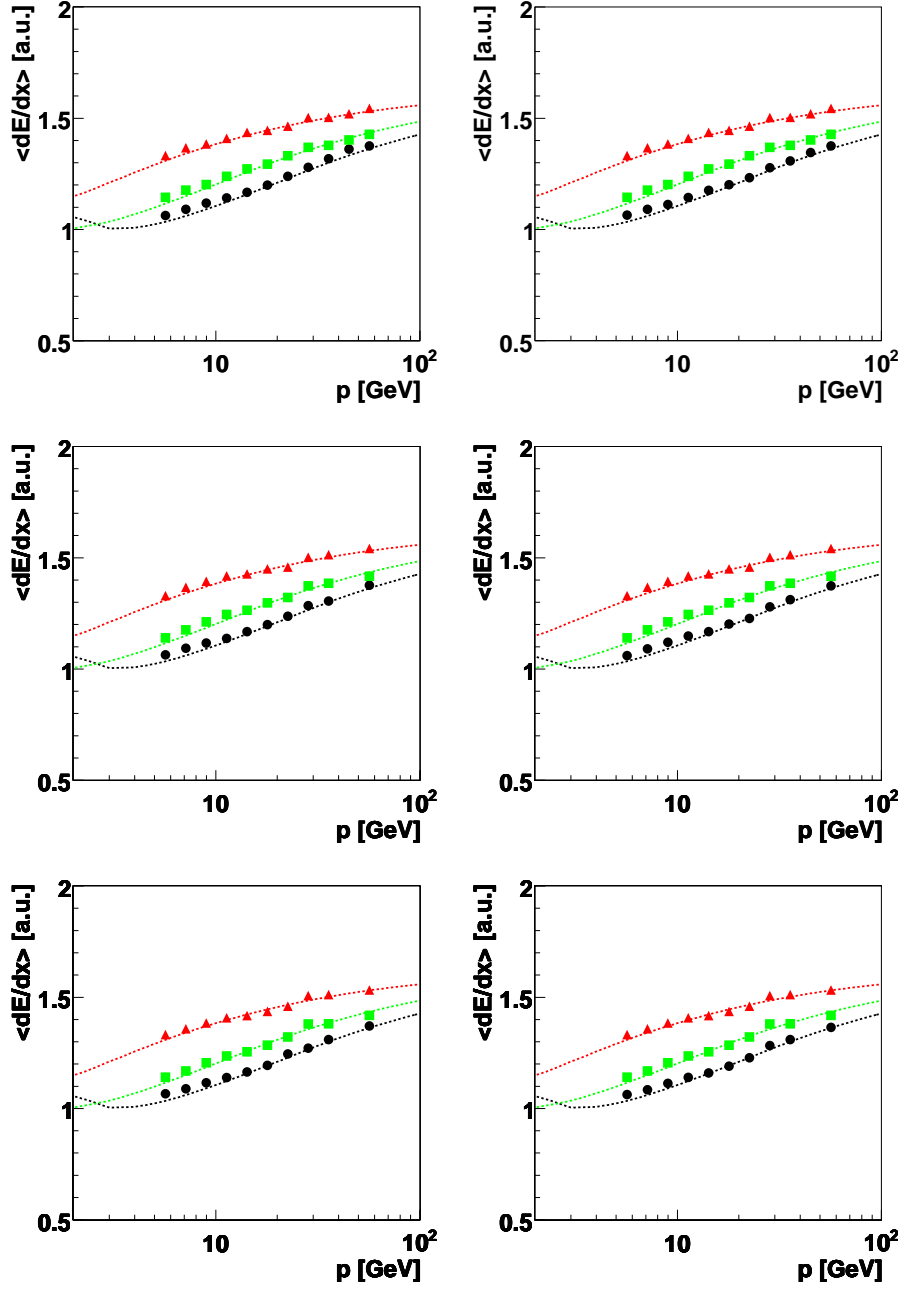


Figure 4.9: Fitted particle positions (symbols) relative to Bethe-Bloch-parametrization (line) at 158 A·GeV for negatively charged (left) and positively charged (right) particles for centrality bin 1 (top), 3 (middle), and 5 (bottom).



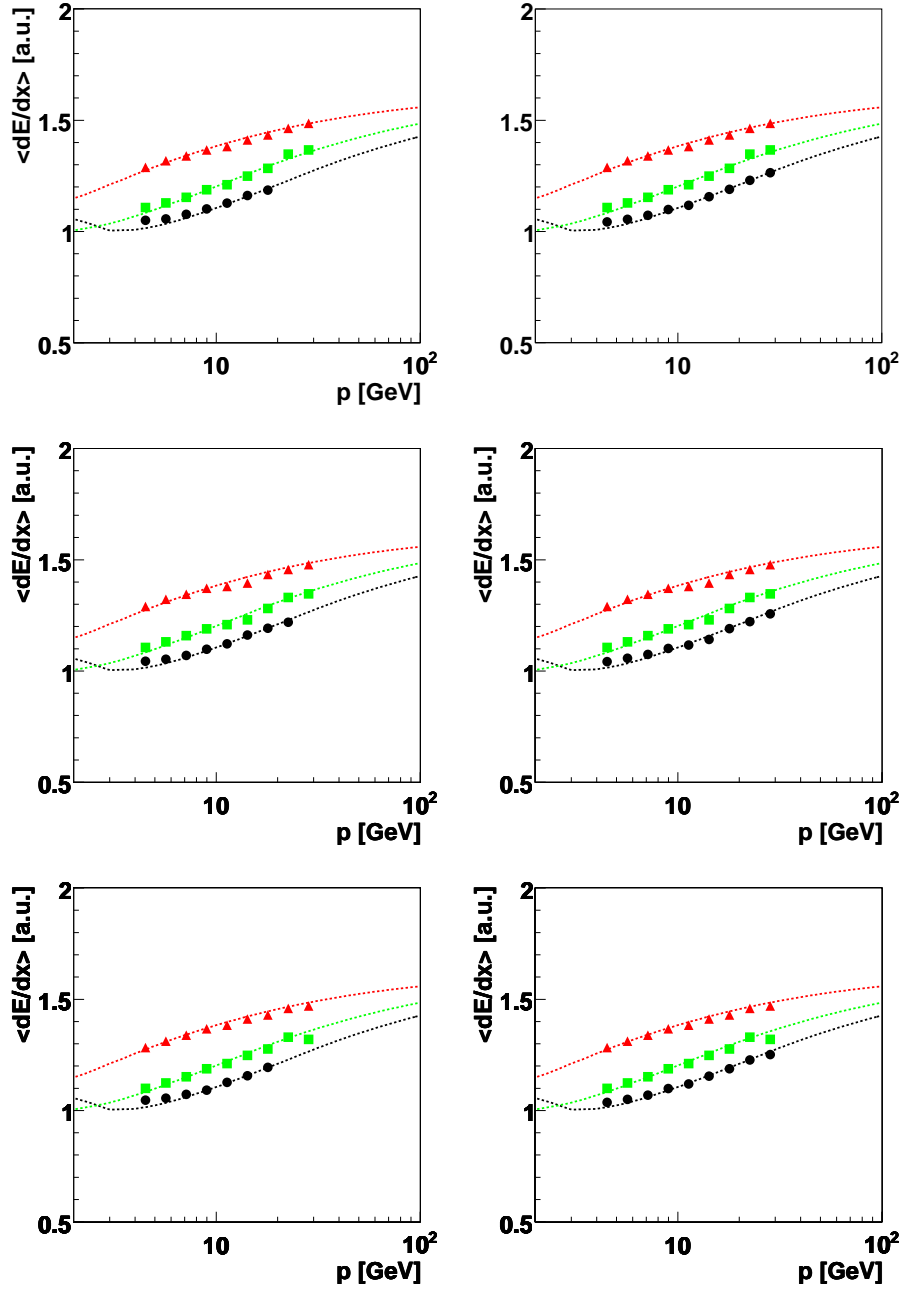


Figure 4.10: Fitted particle positions (symbols) relative to Bethe-Bloch-parametrization (line) at 40 A·GeV for negatively charged (left) and positively charged (right) particles for centrality bin 1 (top), 3 (middle), and 5 (bottom).

# 5 Data Analysis

In the previous chapters, the setup of the NA49 experiment and the track reconstruction from raw data as well as the particle identification by analyzing the mean energy loss in the detector gas have been described. The following sections describe the methods of correcting for detector inefficiencies, acceptance, and background contribution as well as extracting the mean particle multiplicities per event.

## 5.1 Data sets, event and track selection

NA49 has taken several minimum bias data sets which are used in this analysis. To assure the analysis of valid events and well defined tracks, several selection criteria are used. The minimum bias events are subdivided into centrality classes to study the dependence of the analysis results on the size of the collision system.

### 5.1.1 Data sets and event selection

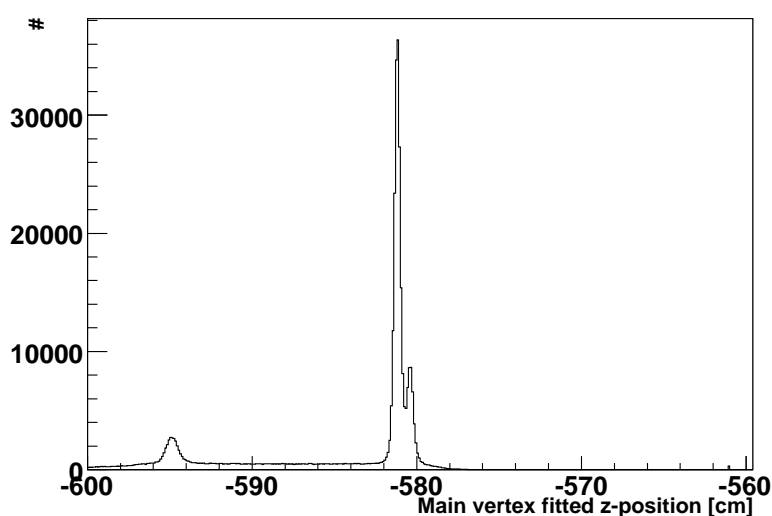
Table 5.1 shows a summary of the data taken and the available statistics. There are sets with different magnetic field polarities to rule out biases of the single TPCs. In 2000, minimum bias data have been recorded with lower beam intensity (data set 01J). This was done to minimize background from beam particles traversing experimental setup during read-out that also suffer energy loss and may build up space charge inside the TPC.

#### Event cuts

The main event cuts limit the vertex position. The vertex position is in general well defined for valid events by the  $z$ -position of the target foil and the extrapolated trajectory

Beam energy	production tag	magnetic field	available events
40 A·GeV	02C	1/4 std+	390,583
40 A·GeV	01D	1/4 std-	360,210
158 A·GeV	00M	std+	203,847
158 A·GeV	00N	std-	113,109
158 A·GeV	01J low int.	std+	338,163

Table 5.1: Minimum bias data sets taken by NA49 collaboration.

Figure 5.1: Distribution of the fitted  $z$ -vertex position in minimum bias events at 158 A·GeV.

of the beam particle in  $x$ - and  $y$ -direction as measured by the beam position detectors. Event reconstruction calculates the vertex position by fitting the reconstructed main vertex tracks. This fitted vertex position is compared to the nominal position determined by the BPDs and the target foil. Figure 5.1 shows the fitted  $z$ -vertex distribution of minimum bias events at 158 A·GeV. Above a nearly constant background originating from beam-air interactions the target foil is clearly visible at -582 cm with a resolution of about 1 cm. The smaller peak on the right shoulder of the distribution is from a sub event sample with a slightly shifted target position. Also visible is a peak at the position of the beam position detector. Its interaction probability is higher than for air due to its higher density. By fixing the cut around the nominal target foil, these interactions are cut out. The cut on the signal from the S3 detector further reduces beam-air interactions. For the vertical position of the interaction point in  $x$  and  $y$  a cut value relative to the extrapolated position determined by the measurements of the

beam position detectors has been selected. The difference between the extrapolated position and the fitted position lies within the accuracy of the measurement as seen in figures 5.2 and 5.3.

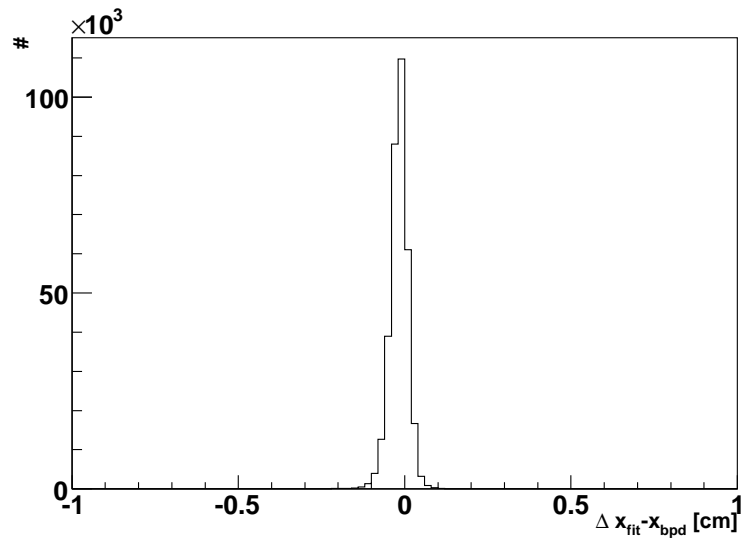


Figure 5.2: Distribution of difference between the fitted  $x$ -vertex position and the  $x$ -bpd position in minimum bias events at 158 A·GeV.

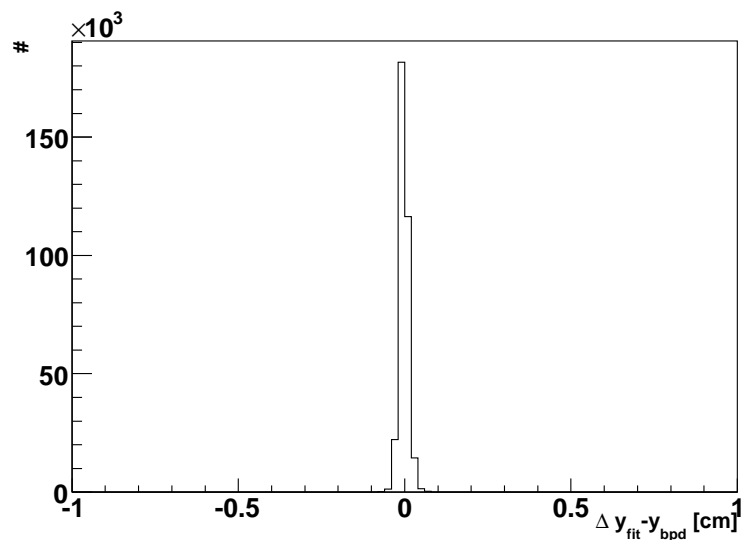


Figure 5.3: Distribution of difference between the fitted  $y$ -vertex position and the  $y$ -bpd position in minimum bias events at 158 A·GeV.

Cut	Minimum value	Maximum value
40 A·GeV Pb+Pb std+ 02C		
Fit vertex iflag	=0	
BPD vertex iflag	=0	
BPD x - fit x	-0.1503	0.1233
BPD y - fit y	-0.08998	0.08042
Target foil z - fit z	-0.8453	0.7947
158 A·GeV Pb+Pb low intensity std+ 01J		
Fit vertex iflag	=0	
BPD vertex iflag	=0	
$z_{fit}$ run 4016-4019	-581.0	-579.6
$z_{fit}$ run 4078-4102	-581.9	-580.5

Table 5.2: Event cuts for data presented in this thesis.

### Centrality selection

The centrality selection is done by subdividing the minimum bias data into different centrality classes of the deposited veto energy which represents the energy of the beam spectators. Since there is a time variation of the efficiency of the photo-multipliers of the calorimeter, a phenomenological correction of the time dependence has been implemented [Lun08]. Figure 5.4 display the measured distribution of the energy deposited in the veto calorimeter for a sample of events at 158 A·GeV. The vertical lines indicate the cuts between the centrality classes. Table 5.3 summarizes the numerical values and available statistics for each centrality bin.

A·GeV	centrality bin	$\sigma/\sigma_{inel.}$	available statistics
40 02C	1	0-5.0%	13,034
	2	5.0-12.5%	22,971
	3	12.5-23.5%	34,035
	4	23.5-33.5%	32,668
	5	33.5-43.5%	32,071
158 01J	1	0-5.0%	15,306
	2	5.0-12.5%	23,548
	3	12.5-23.5%	37,053
	4	23.5-33.5%	34,554
	5	33.5-43.5%	34,583

Table 5.3: Statistics for data presented in this analysis at 40 (data set 02C) and 158 A·GeV (data set 01J low intensity).

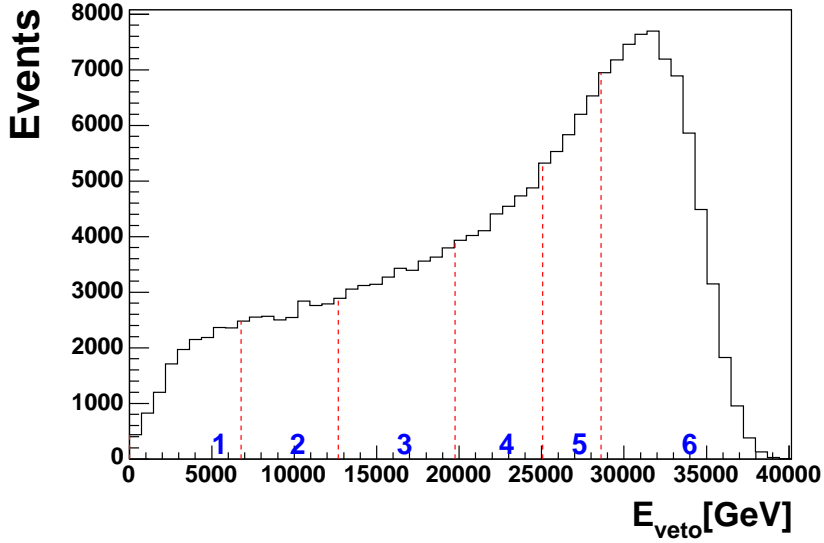


Figure 5.4: Distribution of  $E_{veto}$  for 158 A-GeV. The vertical lines indicate the cuts between the centrality classes.

### 5.1.2 Track selection

For every valid event the tracks are analyzed to identify the relative particle production. Since there are background tracks from secondary interactions and since the resolution of the  $dE/dx$  analysis is dependent on certain track criteria, several quality cuts are used to select well defined main vertex tracks for the kaon analysis. The pion analysis uses much looser cuts. Here, the background is subtracted by analyzing VENUS [Wer93] events. VENUS is used to simulate a full Pb+Pb collision and the tracks are reconstructed analogous to the embedding procedure described below. Table 5.4 lists the criteria for both analyses. The most important cut for the kaon analysis is the number of points cut which determines the  $dE/dx$  resolution. The  $b_x$  and  $b_y$  cut, which restricts the maximum distance to the nominal main vertex position in the plane of the target foil, limit the analysis to main vertex tracks. In order to determine systematical error, several variations of the track cuts have been studied. The main variations were the number of points required and the width of the wedge cut in phi angle.

Cut name	minimal value	maximal value
Pion analysis		
Number of measured points	30	192
NPoint to NMaxPoint	>0.5	
Phi wedge (right side)	-30°	+30°
rTrack iflag		=0
$p_x$ [GeV]		<0
$z_{first}$ [cm]		<-150
Kaon analysis		
No. of points in VTPC (if potential points > 10)	>0	
No. of points in MTPC	50	192
NPoint to NMaxPoint	>0.5	
Phi wedge (right side)	-30°	+30°
$b_x$ [cm]	-2.0	+2.0
$b_y$ [cm]	-1.0	+1.0

Table 5.4: Quality cuts to select valid tracks.

## 5.2 Corrections

Kaon production is derived by analyzing the mean energy loss of the produced particles traversing the detector gas as described in the preceding chapter. By splitting the particles into total and transverse momentum bins, the  $dE/dx$  distribution measured reflects the amount of particles of each species in the covered phase-space. The identification of pions is done in a different way than kaons. Due to their lower mass and the implicit momentum cut for MTPC  $dE/dx$  analysis, pions could only be identified at relatively large forward rapidities. The uncertainty of extrapolating to full phase-space would increase the systematic error. Since about 90% of all negative particles are pions, a different approach is used. To derive total pion multiplicity and spectra all negative particles are analyzed subtracting the background from kaons and anti-protons as well as negative particles from secondary decays and  $\gamma$ -conversions. The so-called  $h^-$  analysis stores all negative particles which fulfill the above specified track cuts in rapidity and transverse momentum bins assuming pion mass.

### 5.2.1 Background correction for $h^-$ analysis

In order to subtract the background contribution to negatively charged particles for the  $h^-$  analysis of pion yields fully reconstructed VENUS [Wer93] (see section 2.5)

events are analyzed. For the analysis of kaon yields this background correction is not necessary due to the negligible contribution from secondary processes and weak decays. Since the relative particle ratios simulated by VENUS do not reflect the measured particle ratios in real experiments [Mit06, Mit07] the background contributions are weighted globally for this difference. Where measured ratios are not available, the predicted ratio from a statistical model calculation [Bec05] was taken. For scaling factors see tables 5.5 and 5.6. A cross-check has been done with background contribution from VENUS events that have been scaled only by a global factor for the particle multiplicities vs. VENUS events where the  $K^-$  distribution has been scaled differentially in  $y - p_T$  in order to reflect the measured  $y - p_T$  spectra. The difference of the total yield lies below a maximum of 2% which does not contribute significantly to the overall systematic error.

Centrality bin	Particle	Scaling factor
1 & 2	$K^0$	1.11
	$\Lambda$	1.26
	$\Sigma$	0.98
	$\Xi$	0.71
	$K^-$	0.91
	$\bar{p}$	0.23
3 & 4	$K^0$	0.966
	$\Lambda$	1.13
	$\Sigma$	0.88
	$\Xi$	0.5
	$K^-$	0.76
	$\bar{p}$	0.17
5 & 6	$K^0$	0.90
	$\Lambda$	0.93
	$\Sigma$	0.73
	$\Xi$	0.29
	$K^-$	0.71
	$\bar{p}$	0.13

Table 5.5: Scaling factors for VENUS particle yields for different centrality bins at 40 A·GeV.

The background contribution is derived in rapidity and transverse momentum bins. The main contributions to the background are negative kaons and anti-protons from the main vertex as well as pions out of secondary vertices of weakly-decaying particles like  $\Lambda$ ,  $\Sigma$ ,  $K_s^0$ , and  $\Xi^-$ . Another contribution comes from muons and electrons. Most muons originate from  $\pi^-$  decays, while electrons are produced by  $\gamma$ -conversions. The muons contribute mainly at backward rapidity, i.e., for slow moving pions having the highest probability to decay inside the detector due to the lower velocity and, hence,



Centrality bin	Particle	Scaling factor
1 & 2	$K^0$	1.04
	$\Lambda$	0.99
	$\Sigma$	1.15
	$\Xi$	0.62
	$K^-$	0.88
	$\bar{p}$	0.345
3 & 4	$K^0$	1.01
	$\Lambda$	0.91
	$\Sigma$	1.06
	$\Xi$	0.48
	$K^-$	0.88
	$\bar{p}$	0.35
5 & 6	$K^0$	1.01
	$\Lambda$	0.92
	$\Sigma$	1.06
	$\Xi$	0.39
	$K^-$	0.88
	$\bar{p}$	0.43

Table 5.6: Scaling factors for VENUS particle yields for different centrality bins at 158 A·GeV.

faster proper time relative to the particles closer to beam velocity. The  $\gamma$ -conversions contribute significantly at low transverse momentum around mid-rapidity. Figure 5.5 and 5.6 show the background correction factors for 40 and 158 A·GeV for the centrality bins 1 and 5.

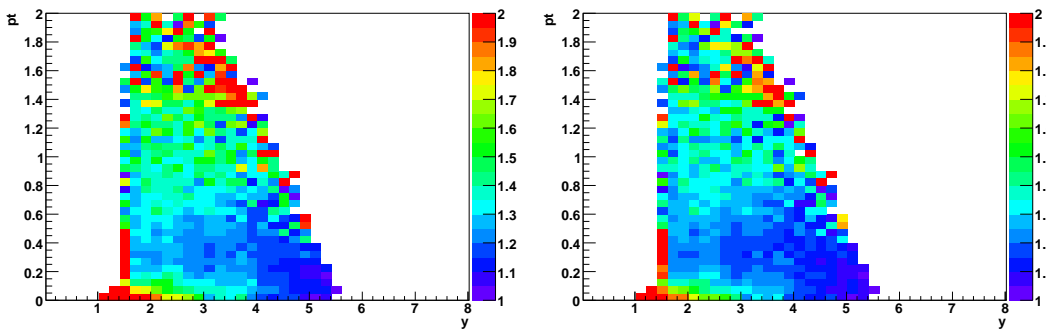


Figure 5.5: Background correction for  $\pi^-$  centrality bin 1 (left) and centrality bin 5 (right) at 40 A·GeV.

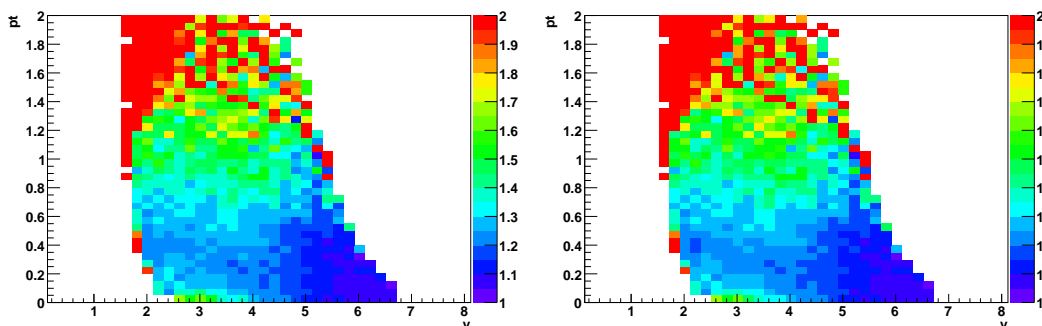


Figure 5.6: Background correction for  $\pi^-$  centrality bin 1 (left) and centrality bin 5 (right) at 158 A·GeV.

## 5.2.2 Simulation for geometrical acceptance and track efficiency

In order to correct for the geometrical acceptance of the detector and the limits set by the track cuts, a simulation is needed. The NA49 experiment uses GEANT [GEA93] to simulate particle trajectories, interaction with detector material, and particle decay. These simulated tracks are embedded into real data by simulating the raw charge distribution of the respective track and the corresponding detector response with `mtsim` [Toy99, Coo00] and reconstructing the event with the full reconstruction chain. By matching simulated, embedded tracks to reconstructed ones, the geometrical acceptance and detector efficiency can be derived. The following figures present the combined correction factor for efficiency and geometrical acceptance for pions at 40 A·GeV (figure 5.7) and 158 A·GeV (figure 5.8) in rapidity and transverse momentum bins. These correction factors are derived for each centrality bin. At 40 A·GeV the efficiency is above 90% for almost all of the acceptance but at the high track density region at mid-rapidity and low transverse momentum and at around 0.5-0.7 unit of rapidity forward of beam rapidity due to the tracking inefficiencies between the Vertex and MainTPCs. At 158 A·GeV the tracking inefficiency due to high track density is very prominent up to 1.0 unit of rapidity forward of mid-rapidity and up to a transverse momentum of 400 MeV. The high density effect almost disappears for the lower multiplicity events in centrality bin 5 in both energies. Since the track quality selection criteria are looser for pions than for kaons, the acceptance tends to be higher whereas the efficiency decreases.

For kaons, the efficiency correction is very homogeneous in transverse and total momentum bins. Most kaons originate directly from the main interaction vertex. Since the

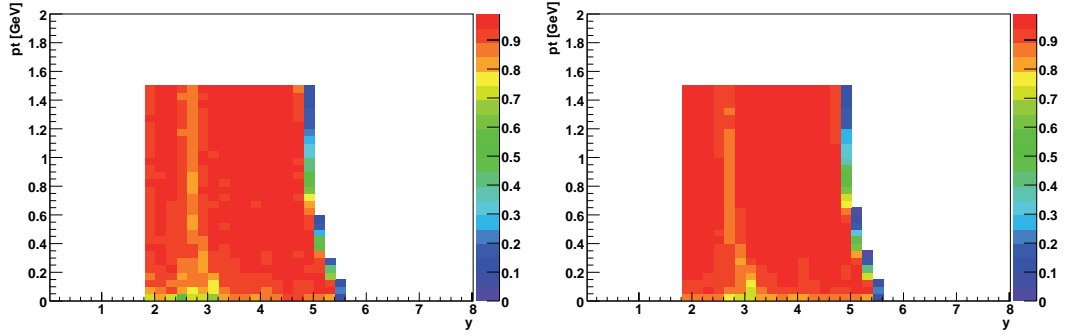


Figure 5.7: Track reconstruction efficiency and geometrical acceptance for  $\pi^-$  centrality bin 1 (left) and centrality bin 5 (right) at 40 A-GeV with minimum number of points  $> 30$  and phi-wedge  $\pm 30^\circ$ .

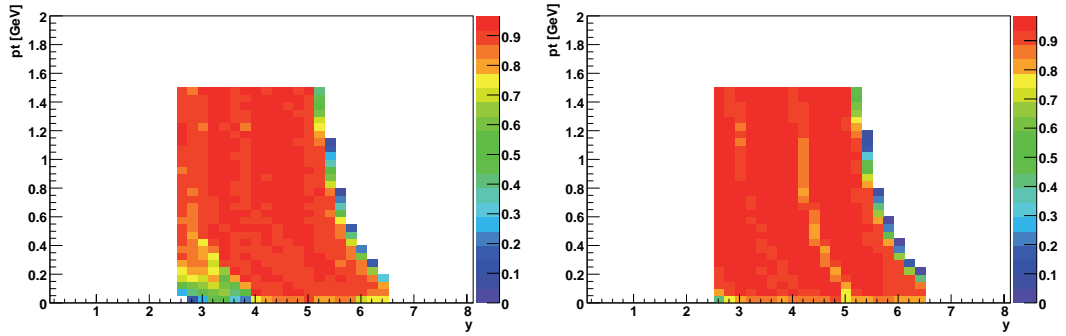


Figure 5.8: Track reconstruction efficiency and geometrical acceptance for  $\pi^-$  centrality bin 1 (left) and centrality bin 5 (right) at 158 A-GeV with minimum number of points  $> 30$  and phi-wedge  $\pm 30^\circ$ .

$dE/dx$  analysis requires stringent quality cuts, the reconstruction efficiency for kaons is very high, generally on the order of 98%. Since kaons decay after  $\tau = 1.238 \cdot 10^{-8}$ s, the geometrical and decay correction shows a stronger dependence on total momentum. The combined correction factor in rapidity and transverse momentum bins is shown for  $K^+$  in figure 5.9 for 40 A-GeV and in figure 5.10 for 158 A-GeV as well as for  $K^-$  in figure 5.11 for 40 A-GeV and in figure 5.12 for 158 A-GeV.

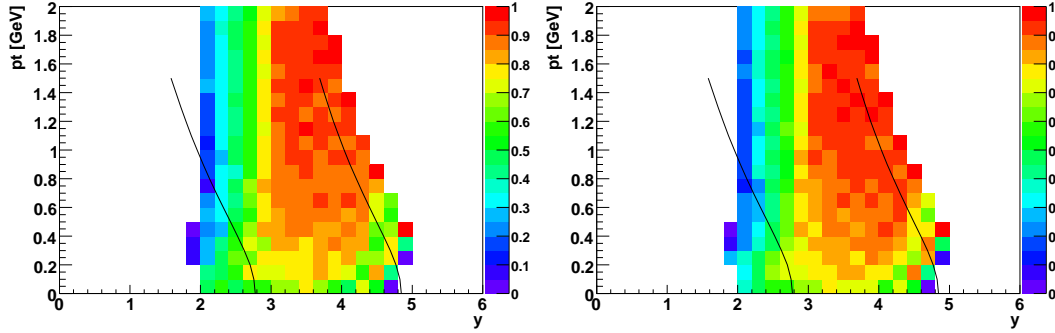


Figure 5.9: Track reconstruction efficiency and geometrical acceptance for  $K^+$  for centrality bin 1 (left) and centrality bin 5 (right) at 40 A·GeV with minimum number of points  $> 50$  and phi-wedge  $\pm 30^\circ$ . The lines indicate the total momentum limits used for the  $dE/dx$  analysis.

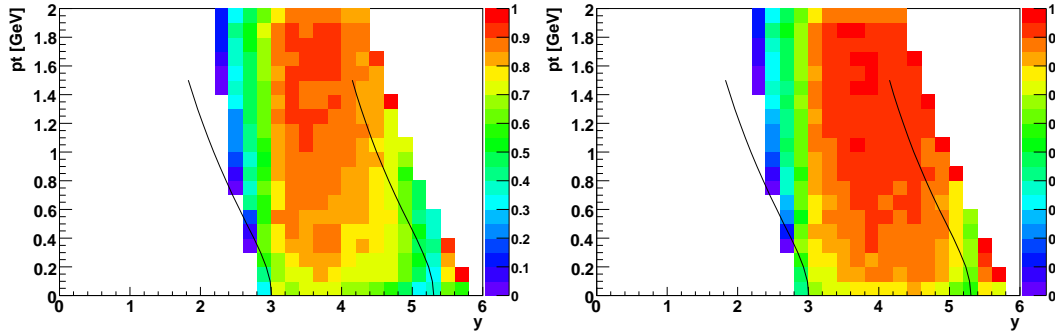


Figure 5.10: Track reconstruction efficiency and geometrical acceptance for  $K^+$  for centrality bin 1 (left) and centrality bin 5 (right) at 158 A·GeV with minimum number of points  $> 50$  and phi-wedge  $\pm 30^\circ$ . The lines indicate the total momentum limits used for the  $dE/dx$  analysis.

### 5.2.3 Decay of kaons into muons

Since the mean lifetime of kaons is  $1.238 \cdot 10^{-8}$ s, which corresponds to about 30m flight length at  $\gamma=8$ , up to 35% of all kaons produced in a Pb+Pb collision at 40 A·GeV decay inside the NA49 detector (strongly depending on rapidity and transverse momentum and, hence, gamma factor as seen in figure 5.13). At 158 A·GeV the maximum fraction of kaons decaying into muons is 20% due to the higher gamma factor at mid-rapidity.

The reconstruction efficiency for kaons decaying into muons is lower than for non-

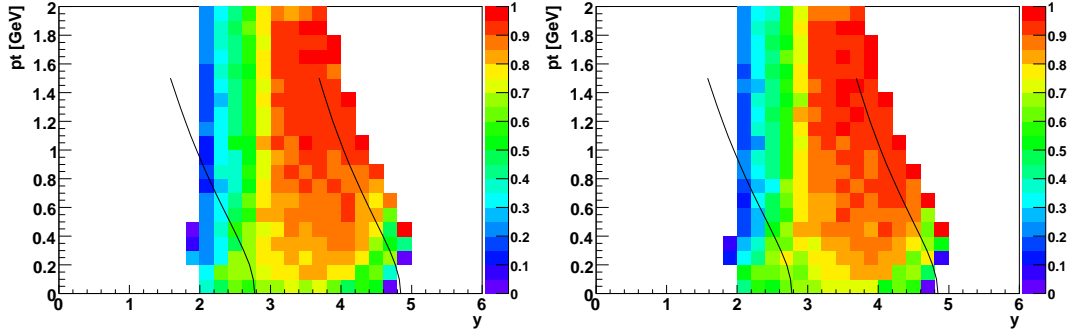


Figure 5.11: Track reconstruction efficiency and geometrical acceptance for  $K^-$  for centrality bin 1 (left) and centrality bin 5 (right) at 40 A-GeV with minimum number of points  $> 50$  and phi-wedge  $\pm 30^\circ$ . The lines indicate the total momentum limits used for the  $dE/dx$  analysis.

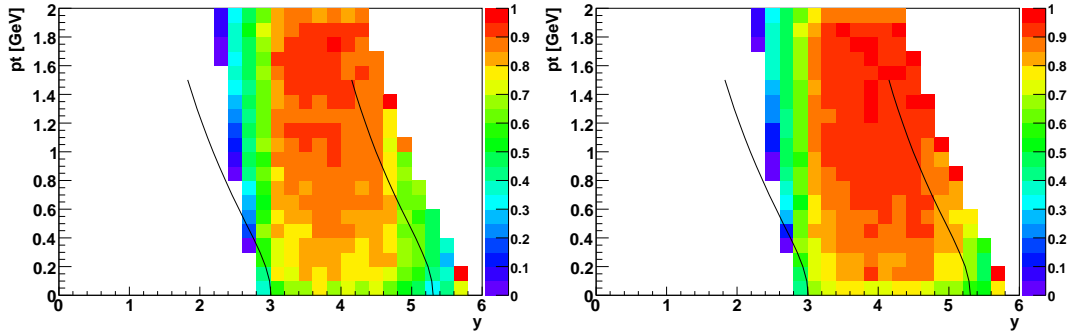


Figure 5.12: Track reconstruction efficiency and geometrical acceptance for  $K^-$  for centrality bin 1 (left) and centrality bin 5 (right) at 158 A-GeV with minimum number of points  $> 50$  and phi-wedge  $\pm 30^\circ$ . The lines indicate the total momentum limits used for the  $dE/dx$  analysis.

decaying kaons due to shorter track length and changed momenta of the muon track after the decay. The combined factor is about 60-70% (figure 5.14). At 158 A-GeV it is slightly lower but still between 60-70%.

Since the kaon and the muon track are often reconstructed as one track, there is a possible mismatch between simulation and real data. Since the reconstruction chain combines the muon track to the kaon track the number of points relative to the maximum number of points and the track length increases. The simulation generally takes the combined track as a valid reconstruction of a kaon track. The  $dE/dx$  value of a real data kaon track, however, is shifted by the muon part, which has a higher observed

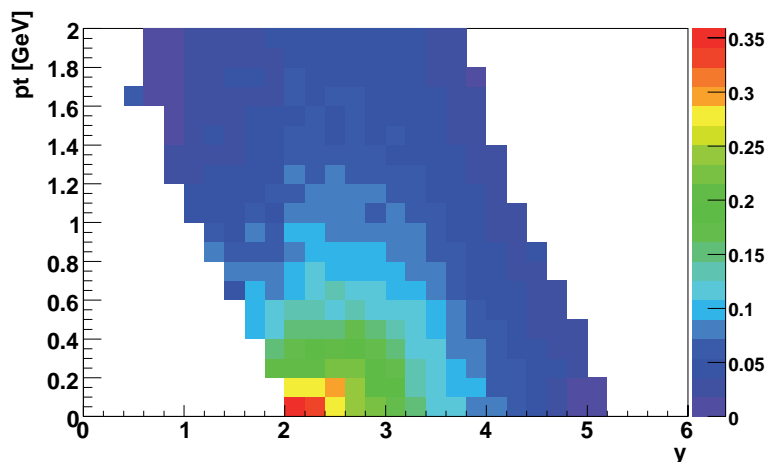


Figure 5.13: Fraction of kaons decaying into muons that have points inside the TPCs compared to all simulated kaons at 40 A·GeV.

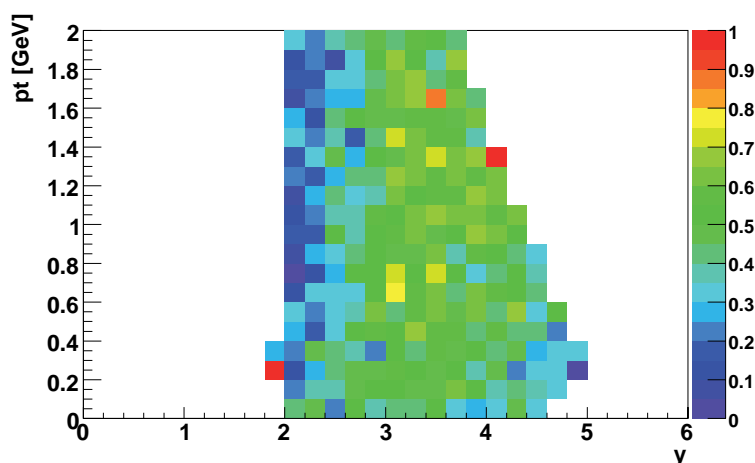


Figure 5.14: Acceptance and reconstruction efficiency for kaons decaying into muons at 40 A·GeV.

mean energy loss in the observed momentum range due to its higher velocity. In the unfolding of the  $dE/dx$  spectra this track can be lost due to its shifting towards the pion nominal position. The maximum possible contribution could be limited to the fraction of all reconstructed and accepted kaon tracks decaying into muons divided by all reconstructed and accepted kaon tracks (figure 5.15 and 5.16). It is around mid-rapidity at about 6-7% at 40 A·GeV and about 3-4% at 158 A·GeV. If one only looks at combinations that have a long muon track length by requiring the combined track to have more than 30% more matched points than maximum number of points on the

kaon track, the maximum percentage of possible wrongly identified tracks shrinks to a maximum of 3% at 40 A·GeV and 2% at 158 A·GeV (figure 5.17 and 5.18). This contributes to the systematical error.

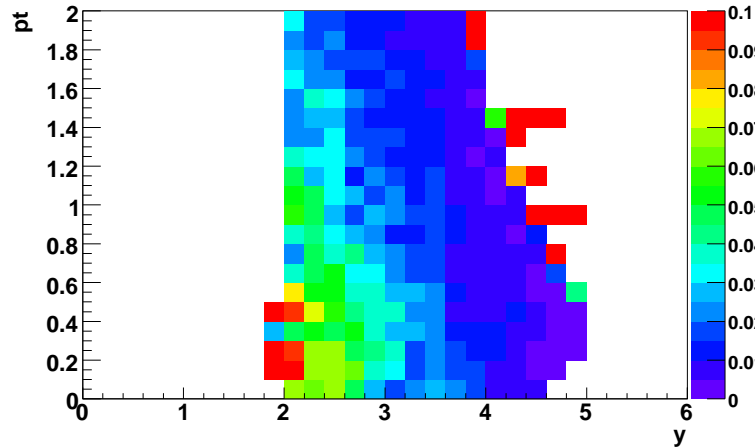


Figure 5.15: Fraction of reconstructed and accepted kaons decaying into muons compared to all reconstructed and accepted kaons at 40 A·GeV.

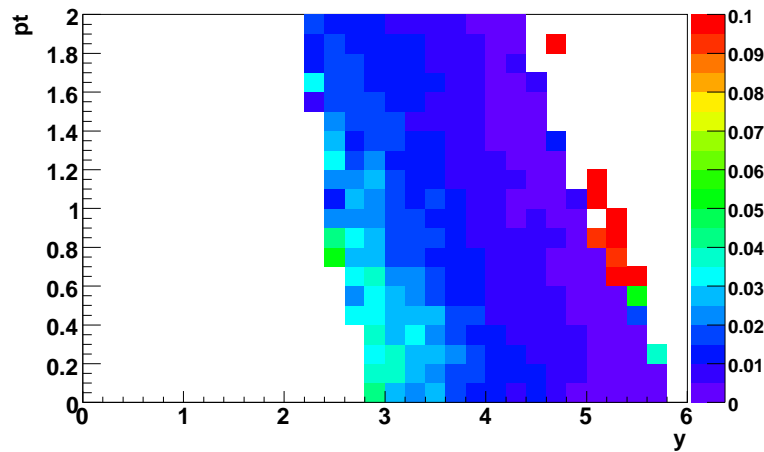


Figure 5.16: Fraction of reconstructed and accepted kaons decaying into muons compared to all reconstructed and accepted kaons at 158 A·GeV.

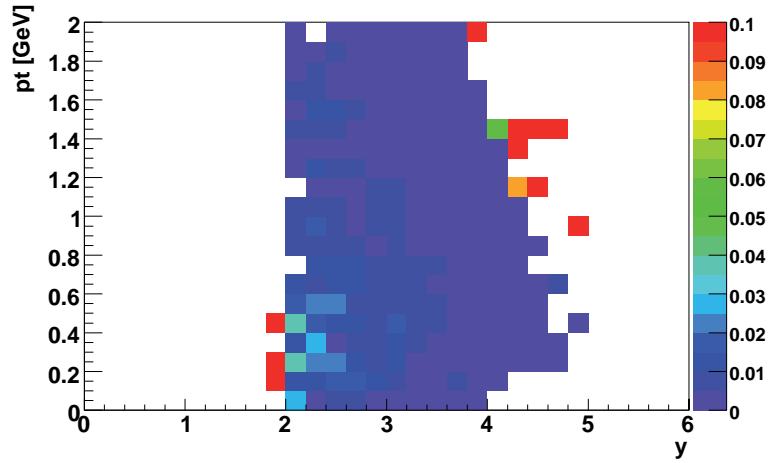


Figure 5.17: Fraction of reconstructed and accepted kaons decaying into muons with a number of points to number of maximum points ratio of higher than 1.3 compared to all reconstructed and accepted kaons at 40 A·GeV.

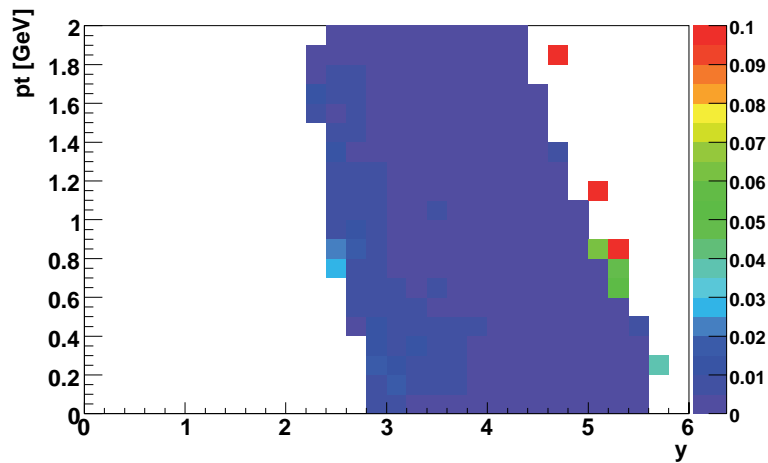


Figure 5.18: Fraction of reconstructed and accepted kaons decaying into muons with a number of points to number of maximum points ratio of higher than 1.3 compared to all reconstructed and accepted kaons at 158 A·GeV.





# 6 Spectra

## 6.1 Pion

The derived correction factors for background contributions and efficiency and geometrical acceptance (chapter 5) are applied to all negatively charged particles in the respective rapidity and transverse momentum bins. For each rapidity bin the  $p_T$ -distributions are summed up to derive the  $dN/dy$  yield. At the edges of the geometrical acceptance at lower and higher rapidities either the high or the low  $p_T$  region is not covered by the detector. Here, an extrapolation with a single exponential function is used to derive the full  $dN/dy$  yield. The measured part of the full yield is close to 1 for most of the acceptance, rapidity bins with less than 70% of total yield measured are not considered for this analysis.

### 6.1.1 Pion transverse momentum spectra

Figure 6.1 presents the derived transverse momentum spectra  $1/p_t dN/dp_t$  at different rapidities for centrality bin 1 at 40 A·GeV, figure 6.2 at 158 A·GeV (for other centrality bins see Appendix C). The values for the single rapidity bins are scaled by the factors stated in the legend to allow for a presentation in a single plot. The lines indicate a fit by the sum of two exponential functions

$$\frac{dN}{dp_T} = c_1 \cdot \exp\left(-\frac{m_T}{T_1}\right) + c_2 \cdot \exp\left(-\frac{m_T}{T_2}\right) \quad (6.1.1)$$

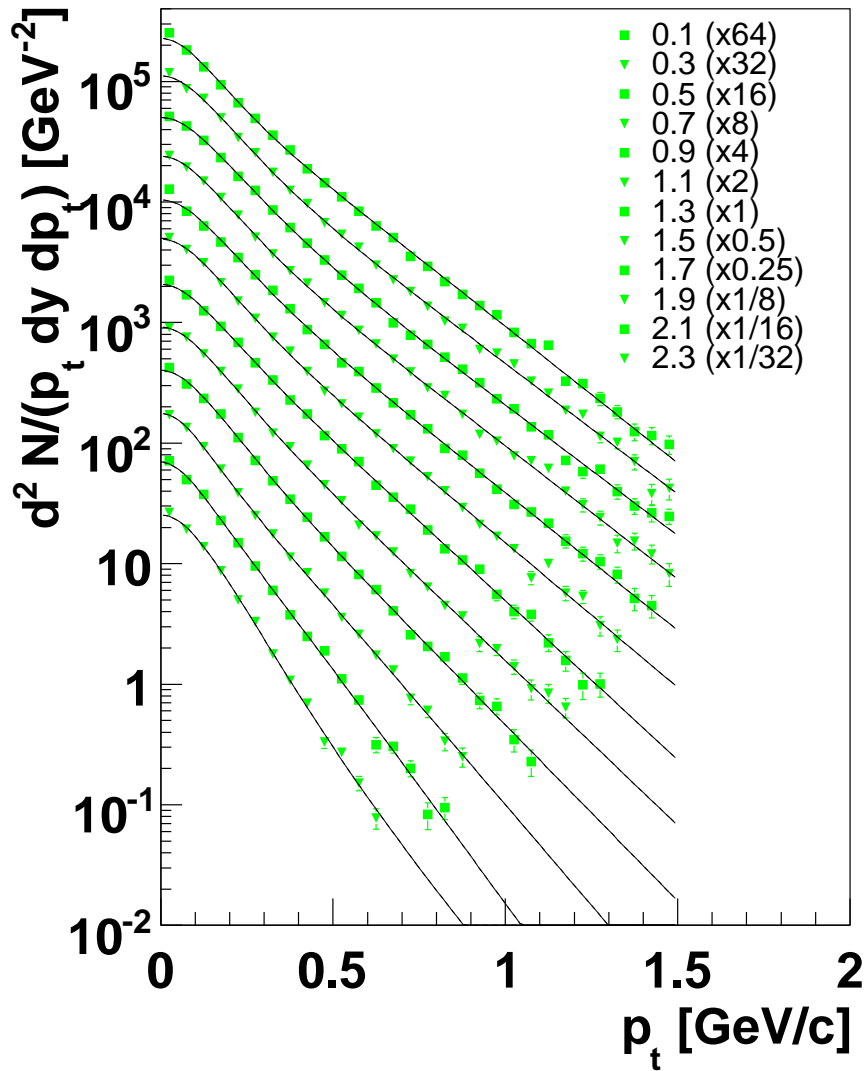


Figure 6.1: Transverse momentum spectra  $1/p_t dN/dp_t$  for  $\pi^-$  for different rapidities (mid-rapidity on top) for centrality bin 1 at 40 A·GeV. The lines indicate a fit by the sum of two exponential functions.

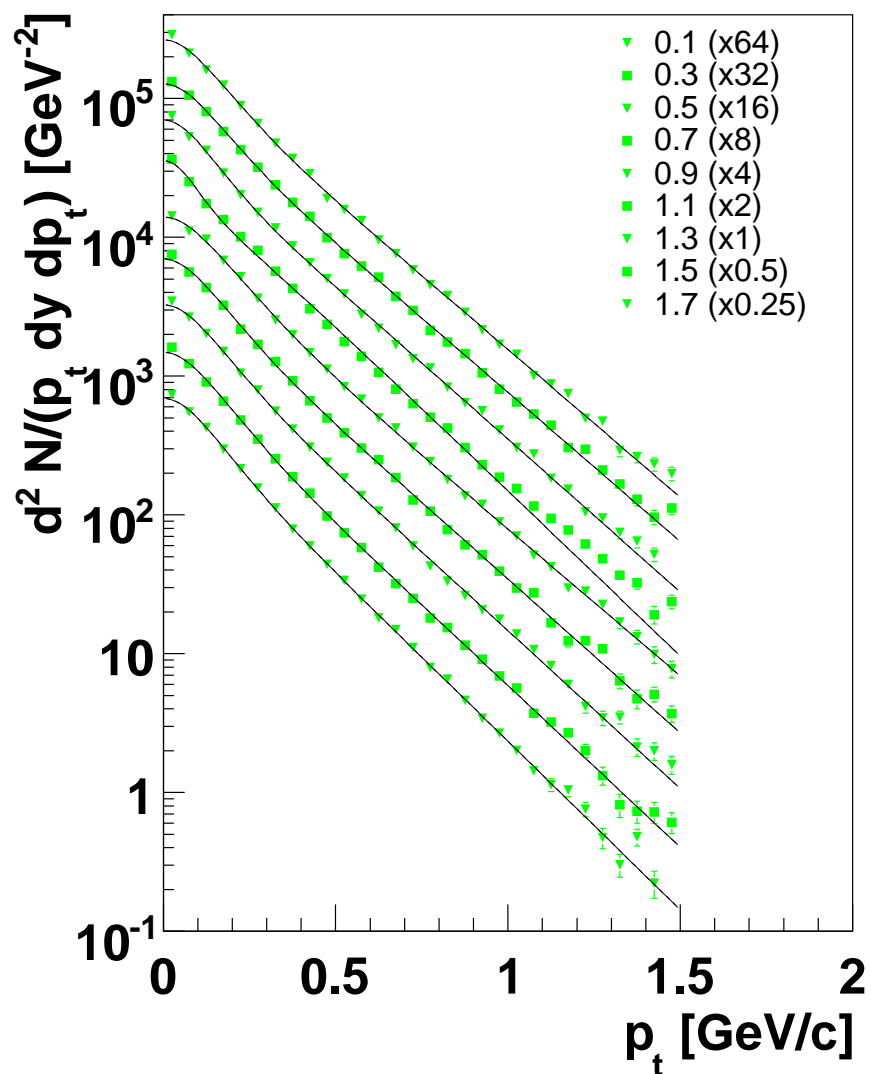


Figure 6.2: Transverse momentum spectra  $1/p_t dN/dp_t$  for  $\pi^-$  for different rapidities (mid-rapidity on top) for centrality bin 1 at 158 A·GeV. The lines indicate a fit by the sum of two exponential functions.

### 6.1.2 Pion rapidity spectra

The resulting rapidity distributions are fitted by a double Gaussian.

$$\frac{dN}{dy} = c \left( \exp -\frac{(y - y_0)^2}{2\sigma_y^2} + \exp -\frac{(y + y_0)^2}{2\sigma_y^2} \right) \quad (6.1.2)$$

Due to the rising correction factors at backward rapidity, only forward rapidity measurements are taken and reflected at mid-rapidity.

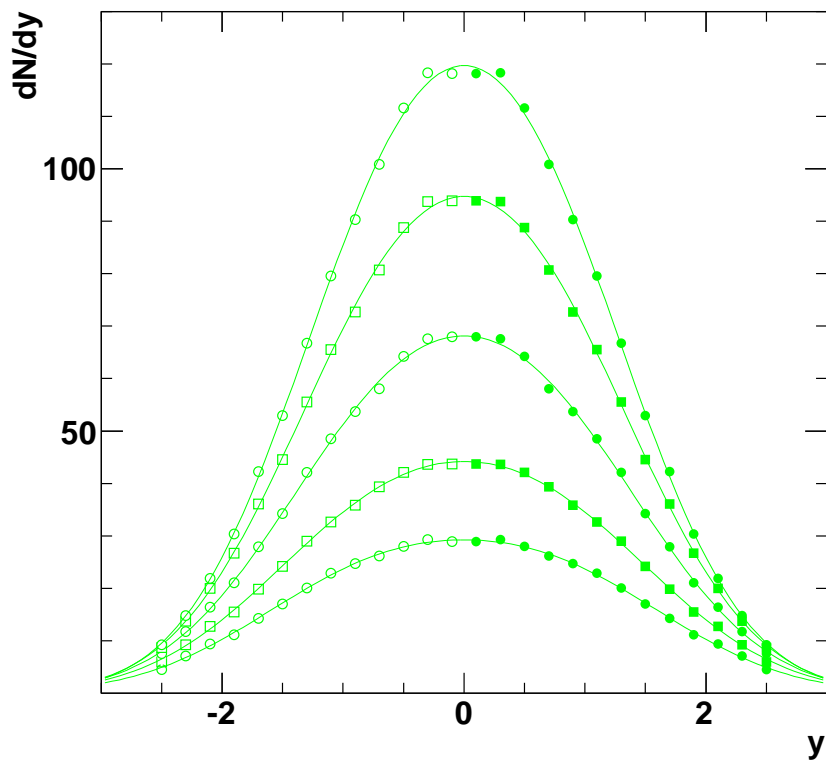


Figure 6.3:  $\pi^-$  rapidity distributions  $dN/dy$  for different centrality bins at 40 A·GeV. Open symbols indicate the reflection of the measured points at mid-rapidity. Neighboring centrality bins are represented alternately with circles and squares starting with centrality bin 1 at the top. The lines indicate a double Gaussian fit.

Centrality bin	Mean multiplicity	$dN/dy_{(y=0)}$	Integral	$y_0$	$\sigma_0$
1	$348.2 \pm 2.4 \pm 17.4$	$118.2 \pm 0.6 \pm 11.8$	348	0.63	0.91
2	$285.8 \pm 2.4 \pm 14.3$	$93.8 \pm 0.4 \pm 9.4$	286	0.66	0.94
3	$213.7 \pm 2.4 \pm 10.7$	$67.7 \pm 0.3 \pm 6.8$	214	0.69	0.98
4	$146.2 \pm 2.2 \pm 7.3$	$43.6 \pm 0.3 \pm 4.4$	146	0.74	1.01
5	$101.0 \pm 1.9 \pm 10.1$	$29.1 \pm 0.2 \pm 2.9$	101	0.80	1.01

Table 6.1: Mean multiplicities and fit parameters for double Gaussian fit of  $\pi^-$   $dN/dy$  spectra for different centrality bins at 40 A·GeV.

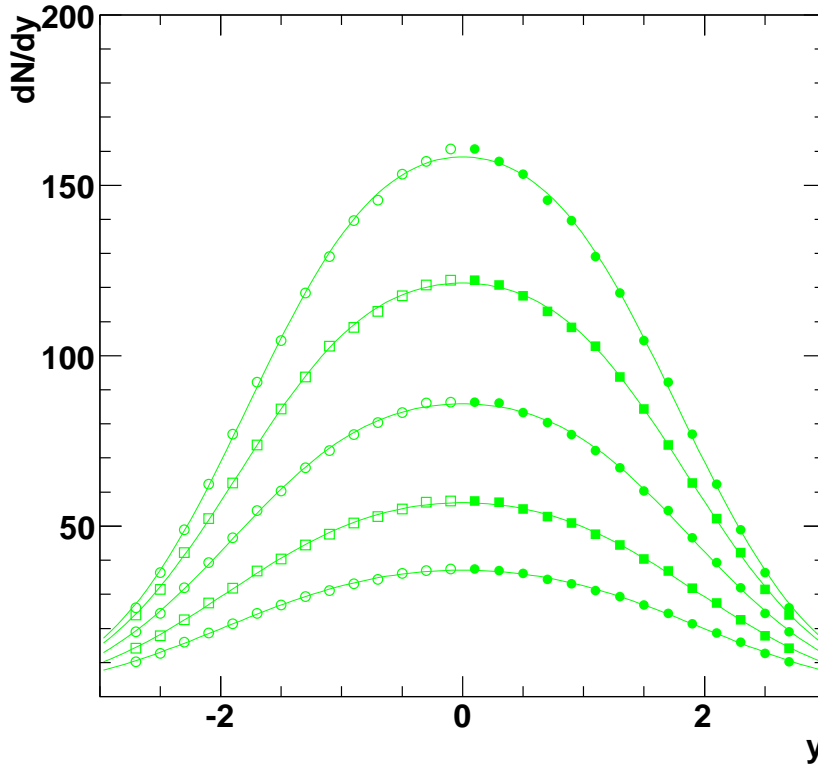


Figure 6.4:  $\pi^-$  rapidity distributions  $dN/dy$  for different centrality bins at 158 A·GeV. Open symbols indicate the reflection of the measured points at mid-rapidity. Neighboring centrality bins are represented alternately with circles and squares starting with centrality bin 1 at the top. The lines indicate a double Gaussian fit.

### 6.1.3 Positive pions

The  $h^-$ -analysis for negative pions cannot be used for positive particles since the systematic error is much higher due to the contribution of projectile and target protons to

Centrality bin	Mean multiplicity	$dN/dy_{(y=0)}$	Integral	$y_0$	$\sigma_0$
1	$601.8 \pm 4.7 \pm 30.1$	$158.8 \pm 0.7 \pm 15.9$	602	0.90	1.07
2	$479.8 \pm 4.5 \pm 24.0$	$121.4 \pm 0.6 \pm 12.1$	480	0.94	1.09
3	$348.7 \pm 3.2 \pm 17.4$	$86.2 \pm 0.5 \pm 8.6$	349	0.96	1.13
4	$236.6 \pm 3.8 \pm 11.8$	$57.2 \pm 0.4 \pm 5.7$	237	0.97	1.20
5	$158.7 \pm 3.4 \pm 15.9$	$37.2 \pm 0.3 \pm 3.7$	159	0.99	1.27

Table 6.2: Mean multiplicities and fit parameters for double Gaussian fit of  $\pi^-$   $dN/dy$  spectra for different centrality bins at 158 A·GeV.

the total multiplicity. Via time-of-flight measurement the  $\pi^+$  and  $\pi^-$  multiplicity can be determined precisely at mid-rapidity. At 158 A·GeV a centrality dependent TOF analysis for charged pions exists [Kol06] which shows no dependence on centrality. Figure 6.5 shows the energy dependence of the  $\pi^+$  to  $\pi^-$  ratio. This ratio is used as a factor to determine the  $\pi^+$  yield from the  $\pi^-$  multiplicity. At 40 A·GeV the factor is 0.90, at 158 A·GeV it is 0.93 [Alt07].

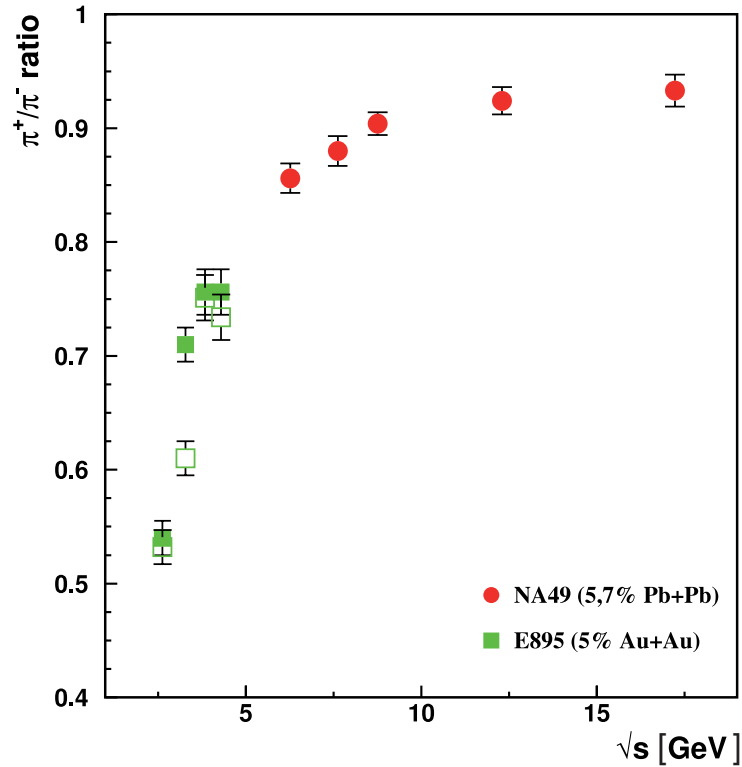


Figure 6.5:  $\pi^+$  to  $\pi^-$  ratio around mid-rapidity depending on the center of mass energy of the collision [Kol06].

### 6.1.4 Systematic cross-checks and determination of systematic error

In order to test the simulation and the corrections applied to the measured data, the track cuts are systematically varied. For the pion analysis, the total number of points were set to 30 and 50 and the corrections were derived from the simulation respectively. In addition, a  $dE/dx$  cut was applied to remove electrons. Figure 6.6 shows the normalized truncated mean vs. the logarithmic total momentum of the tracks for centrality bin 1 and 5. The solid lines indicate the Bethe-Bloch-parameterization of  $e^-$ ,  $\pi^-$ ,  $K^-$ , and  $\bar{p}$ . The dashed lines present two applied  $dE/dx$  cuts at the pion parameterization plus 0.25 and 0.35 units respectively. The  $dE/dx$  resolution for centrality bin 1 does not allow a clear separation between the pions and electrons. In bin 5 a separation of the two particles is possible and the  $dE/dx$  cut was determined as the pion parameterization plus 0.25 units.

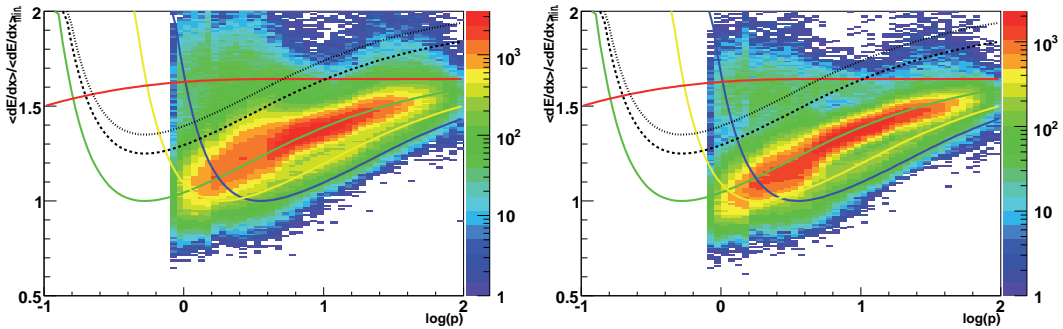


Figure 6.6: Particle energy loss  $dE/dx$  vs. logarithmic momentum  $\log(p)$  for centrality bin 1 (left) and centrality bin 5 (right) at 158 A·GeV. Solid lines indicate Bethe-Bloch-parameterization of different particle species. The dashed line indicates the used cut value (pion Bethe-Bloch-parameterization + 0.25) for electron removal. The dotted line indicates an alternative cut value (pion Bethe-Bloch-parameterization + 0.35).

Figure 6.7 show  $\pi^-$  transverse momentum distributions for three analyses with a minimum number of 30 resp. 50 points, and electron removal via  $dE/dx$  for centrality bin 1 (left) and 5 (right) at 158 A·GeV. In general, the difference is up to 5-10%. However, at low transverse momentum the acceptance and efficiency correction does not fully correct for the losses of tracks with a minimum number of 50 points.



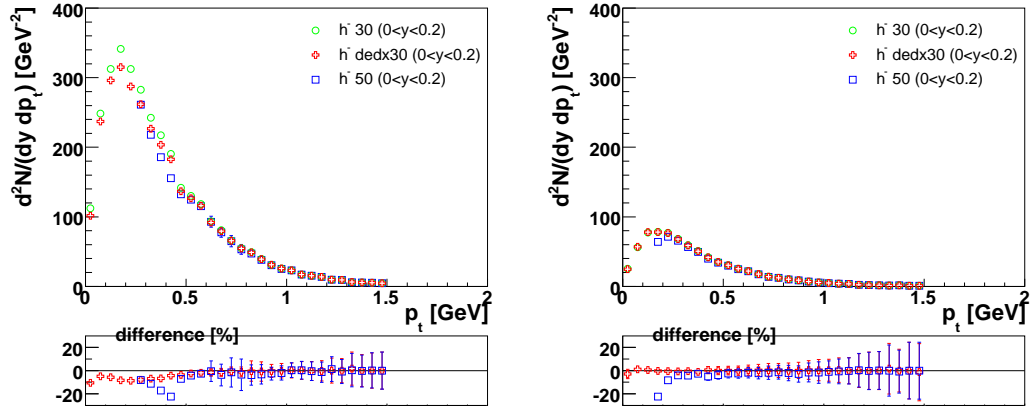


Figure 6.7:  $\pi^-$  transverse momentum distributions are shown on the top part at mid-rapidity ( $0.0 < y < 0.2$ ) for the  $h^-$  analysis with a minimum number of 30 resp. 50 points, and electron removal via  $dE/dx$  for centrality bin 1 (left) and 5 (right) at 158 A·GeV. On the bottom part, the difference relative to the standard analysis with 30 points is shown.

At higher rapidities, the systematic differences are smaller than the statistical error (see figure 6.8). At 40 A·GeV systematic deviations are seen only for transverse momenta below 100 MeV (see figure 6.9).

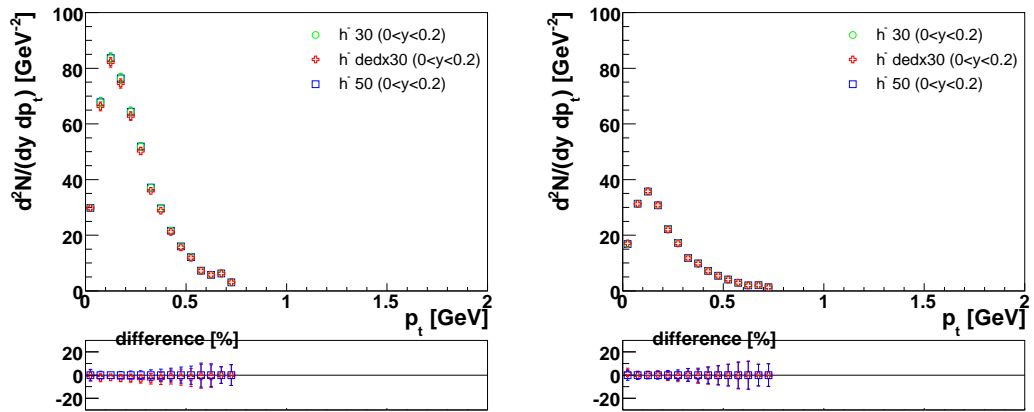


Figure 6.8:  $\pi^-$  transverse momentum distributions are shown on the top part at  $2.6 < y < 2.8$  for  $h^-$  analysis with a minimum number of 30 resp. 50 points, and electron removal via  $dE/dx$  for centrality bin 1 (left) and 5 (right) at 158 A·GeV. On the bottom part, the difference relative to the standard analysis with 30 points is shown.

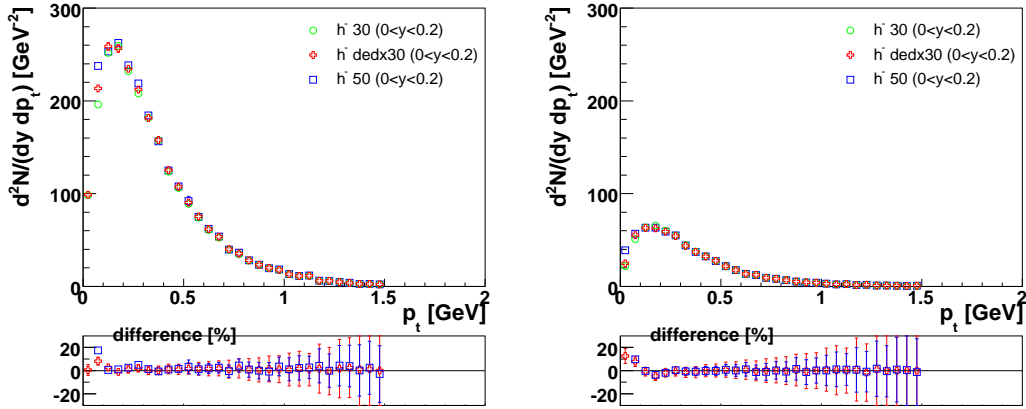


Figure 6.9:  $\pi^-$  transverse momentum distributions are shown on the top part at mid-rapidity for  $h^-$  analysis with a minimum number of 30 resp. 50 points, and electron removal via  $dE/dx$  for centrality bin 1 (left) and 5 (right) at 40 A·GeV. On the bottom part, the difference relative to the standard analysis with 30 points is shown.

Figure 6.10 shows the derived mean multiplicity for negatively charged pions at 158 and 40 A·GeV for different systematic variations. The systematic error of the total yield is about 5% for the centrality bins 1 to 4 and 10% for centrality bin 5. This higher error is due to the uncertainties of the event selection for the most peripheral centrality bin. Analysis 5 of the 00Ma data set in figure 6.10 deviates as much from the standard analysis. The midrapidity measurement has a systematical error of about 10% due to the higher background corrections.

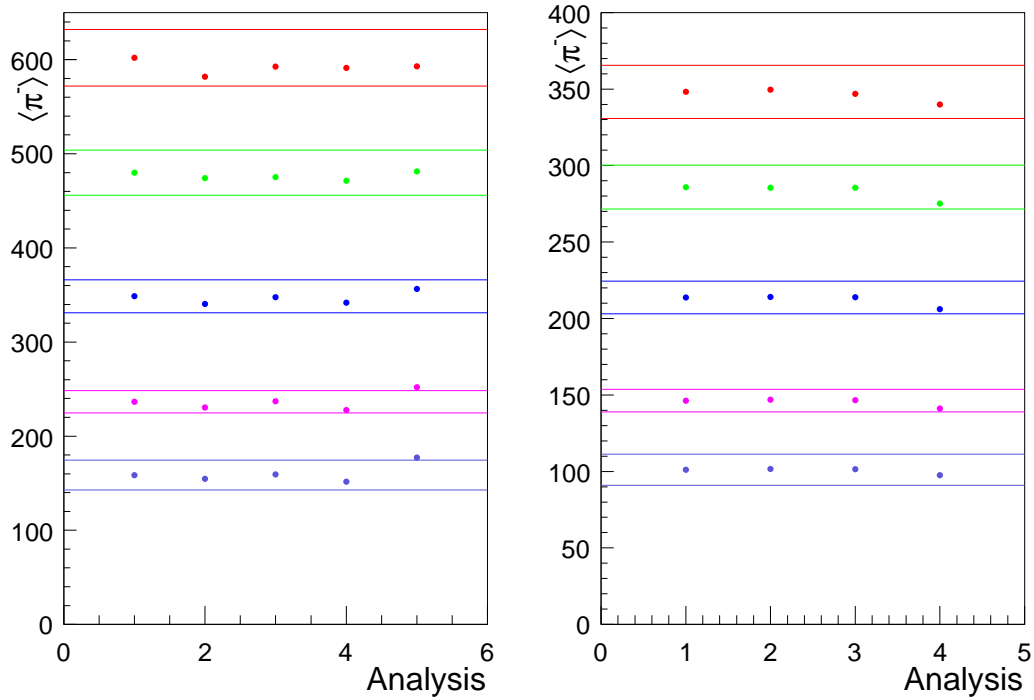


Figure 6.10: Mean multiplicities for  $\pi^-$  at 158 (left) and 40 A-GeV (right) for the different centrality bins. Analysis 1 is the standard analysis with a minimum number of 30 points, analysis 2 with a minimum number of 50, analysis 3 with a minimum number of 30 and electron removal via  $dE/dx$ , analysis 4 shows the standard analysis with a minimum number of 30 points for a data sample with negative magnetic field configuration, analysis 5 shows the result for the 00Ma data set with the track selection from the standard analysis. The colored lines indicate the systematic errors of 5% for centrality bin 1 to 4 and 10% for centrality bin 5.

## 6.2 Kaon

After fitting the  $dE/dx$  spectra, all bins are corrected for geometrical acceptance, kaon decay, and reconstruction efficiency as described in chapter 5. The feeddown from weak decays to kaons is negligible. The logarithmic total momentum bins are transformed into rapidity bins and for each the transverse momentum distribution is fitted with an exponential function (equation 6.2.1):

$$\frac{dN}{dp_T} = c \cdot p_T \exp\left(-\frac{m_T}{T}\right) \quad (6.2.1)$$

with  $p_T$  the transverse momentum,  $m_T$  the transverse mass, and  $T$  the inverse slope parameter.

### 6.2.1 Kaon transverse momentum spectra

The fitting region for the extrapolation is unrestrained from a transverse momentum of 0.0 up to 1.5 GeV. To derive the inverse slope parameter  $T$ , the range is constrained from 0.2 to 0.7 GeV to allow comparisons with previous measurements. The relative yield in each rapidity bin  $dN/dy$  is derived by summing up the  $dN/dydp_T$  measurements where available and extrapolating the fitted exponential function to the region not measured. Figures 6.11 and 6.12 show transverse momentum spectra of  $K^+$  and  $K^-$  for centrality bin 1 at 40 and 158 A·GeV (for other centrality bins see Appendix C).

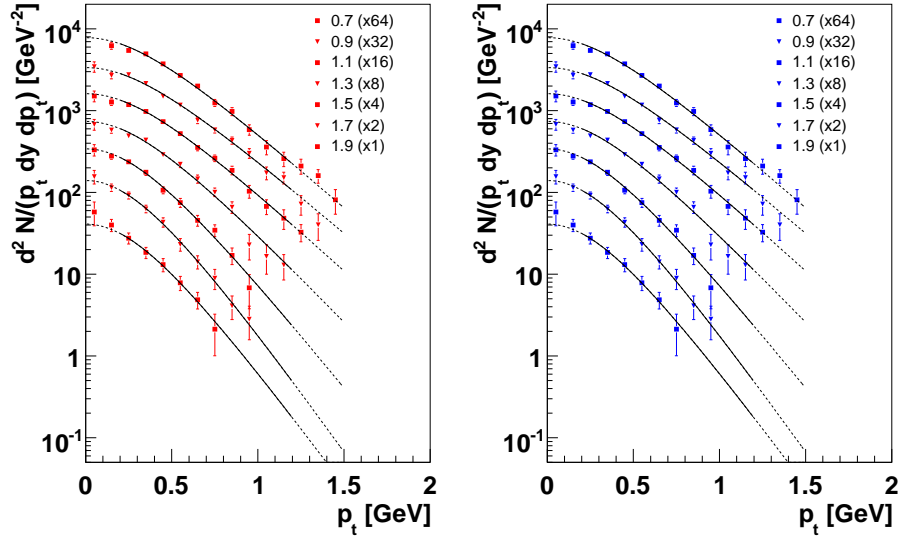


Figure 6.11: Transverse momentum spectra  $1/p_t dN/dp_t$  for  $K^+$  (left) and  $K^-$  (right) for different rapidities (mid-rapidity on top) for centrality bin 1 at 40 A·GeV. The lines indicate a fit by a single exponential function (solid for fitting range).

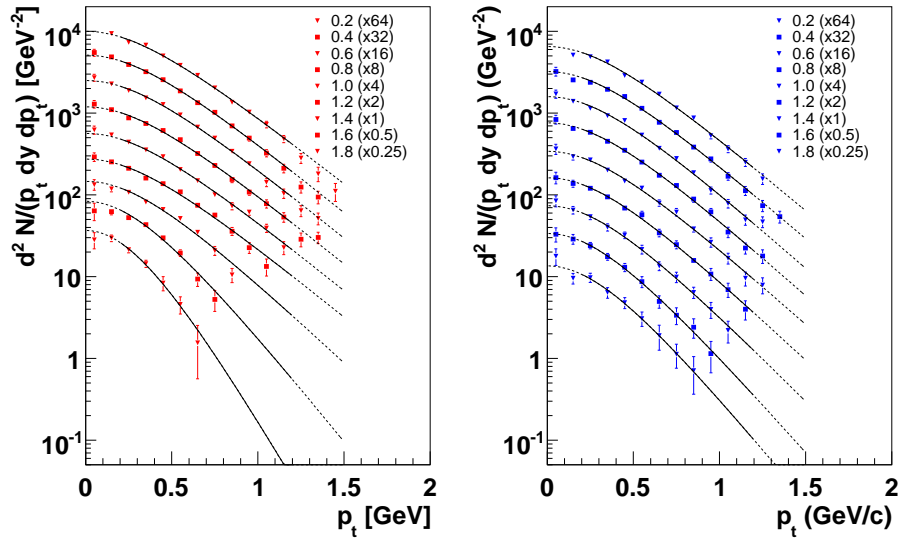


Figure 6.12: Transverse momentum spectra  $1/p_t dN/dp_t$  for  $K^+$  (left) and  $K^-$  (right) for different rapidities (mid-rapidity on top) for centrality bin 1 at 158 A·GeV. The lines indicate a fit by a single exponential function (solid for fitting range).

## 6.2.2 Kaon rapidity spectra

The resulting rapidity distribution is fitted by a double Gaussian (see equation 6.2.2). By including the measurements from the time-of-flight (TOF) analysis, the full forward hemisphere is covered at 158 A·GeV. At 40 A·GeV, there is a gap in the rapidity distribution not covered by TOF and  $dE/dx$  analysis. Total kaon multiplicity is derived by summing up the measured  $dN/dy$  and taking the fitted double Gaussian to interpolate between TOF and  $dE/dx$  acceptance.

$$\frac{dN}{dy} = c \left( \exp -\frac{(y - y_0)}{2\sigma_y^2} + \exp -\frac{(y + y_0)}{2\sigma_y^2} \right) \quad (6.2.2)$$

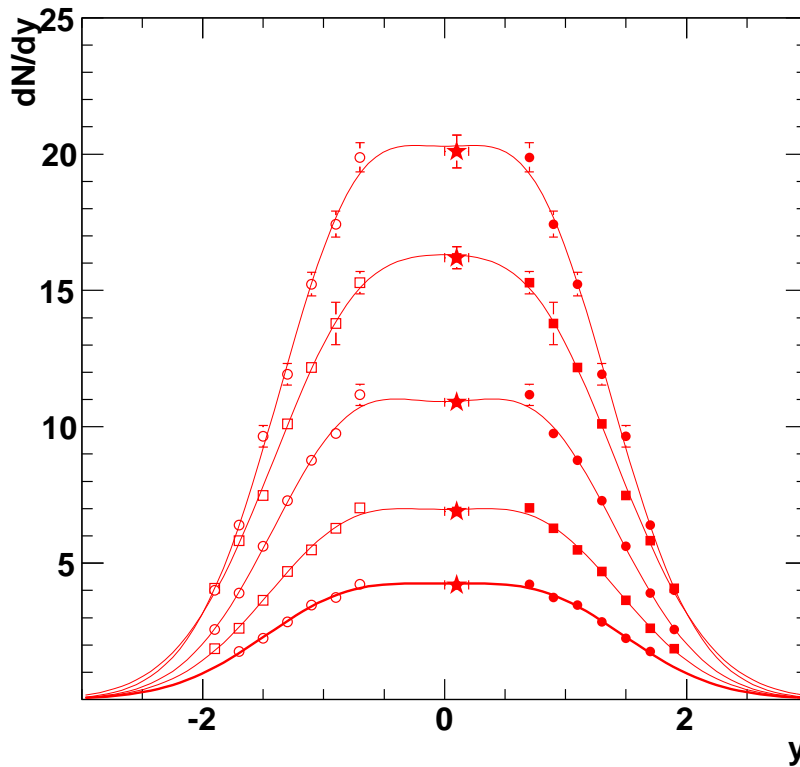


Figure 6.13:  $K^+$  rapidity distributions  $dN/dy$  for different centrality bins at 40 A·GeV beginning with centrality bin 1 at the top. The star shows the results of the time-of-flight measurements.

Centrality bin	Mean multiplicity	$dN/dy_{(y=0)}$	Integral	$y_0$	$\sigma_y$
1	$60.0 \pm 4.3 \pm 4.8$	$18.6 \pm 0.4 \pm 1.9$	60	0.72	0.70
2	$48.9 \pm 3.9 \pm 3.9$	$14.8 \pm 0.4 \pm 1.5$	49	0.73	0.76
3	$34.0 \pm 3.2 \pm 2.7$	$10.3 \pm 0.2 \pm 1.0$	34	0.75	0.71
4	$21.6 \pm 2.5 \pm 1.7$	$6.6 \pm 0.1 \pm 0.7$	22	0.78	0.71
5	$13.5 \pm 2.1 \pm 1.4$	$4.0 \pm 0.1 \pm 0.4$	14	0.78	0.75

Table 6.3: Mean multiplicities and fit parameters for double Gaussian fit of  $K^+$   $dN/dy$  spectra for different centrality bins at 40 A-GeV.

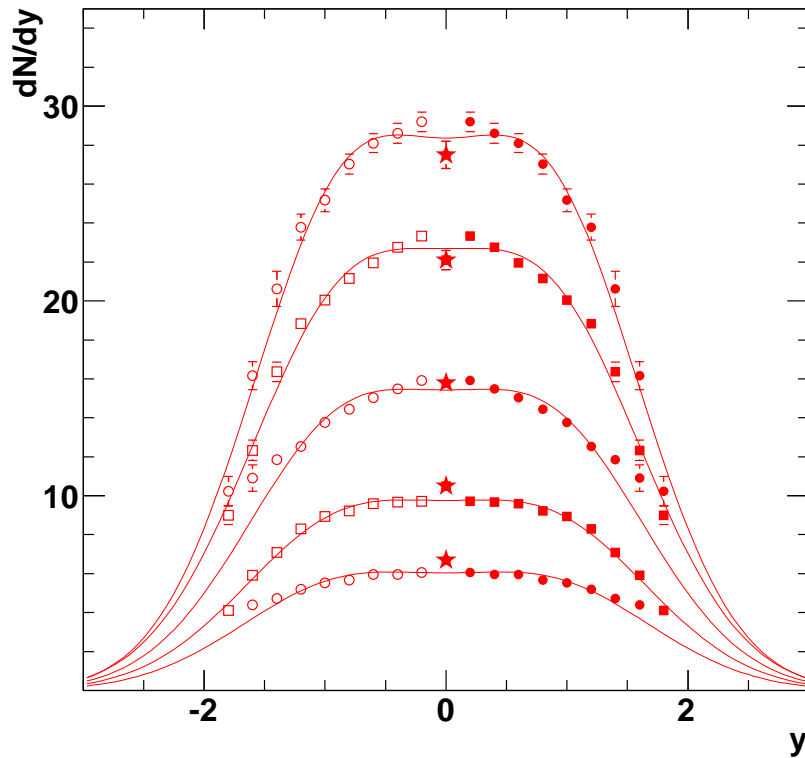


Figure 6.14:  $K^+$  rapidity distributions  $dN/dy$  for different centrality bins at 158 A-GeV beginning with centrality bin 1 at the top. The star shows the results of the time-of-flight measurements.

Centrality bin	Mean multiplicity	$dN/dy_{(y=0)}$	Integral	$y_0$	$\sigma_y$
1	$97.8 \pm 3.0 \pm 7.8$	$28.9 \pm 0.4 \pm 2.9$	98	0.83	0.80
2	$78.5 \pm 2.8 \pm 6.3$	$23.0 \pm 0.2 \pm 2.3$	78	0.84	0.83
3	$55.4 \pm 2.9 \pm 4.4$	$15.7 \pm 0.2 \pm 1.6$	54	0.85	0.83
4	$34.9 \pm 2.0 \pm 2.8$	$9.7 \pm 0.1 \pm 1.0$	35	0.86	0.84
5	$22.2 \pm 1.9 \pm 2.2$	$6.0 \pm 0.1 \pm 0.6$	22	0.87	0.83

Table 6.4: Mean multiplicities and fit parameters for double Gaussian fit of  $K^+$   $dN/dy$  spectra for different centrality bins at 158 A·GeV.

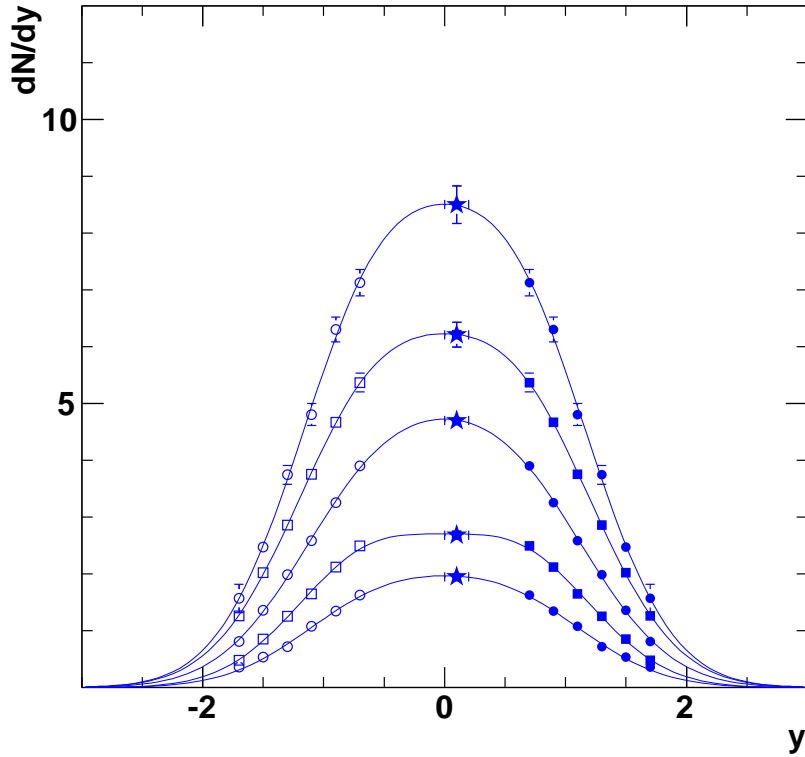


Figure 6.15:  $K^-$  rapidity distributions  $dN/dy$  for different centrality bins at 40 A·GeV beginning with centrality bin 1 at the top. The star shows the results of the time-of-flight measurements.



Centrality bin	Mean multiplicity	$dN/dy_{(y=0)}$	Integral	$y_0$	$\sigma_y$
1	$21.0 \pm 2.8 \pm 1.7$	$6.7 \pm 0.2 \pm 0.7$	21	0.59	0.66
2	$15.9 \pm 2.4 \pm 1.3$	$5.0 \pm 0.1 \pm 0.5$	16	0.61	0.68
3	$11.5 \pm 2.1 \pm 0.9$	$3.6 \pm 0.1 \pm 0.4$	11	0.56	0.70
4	$7.0 \pm 1.6 \pm 0.6$	$2.3 \pm 0.1 \pm 0.2$	7	0.62	0.63
5	$4.6 \pm 1.3 \pm 0.5$	$1.5 \pm 0.1 \pm 0.2$	5	0.56	0.64

Table 6.5: Mean multiplicities and fit parameters for double Gaussian fit of  $K^-$   $dN/dy$  spectra for different centrality bins at 40 A-GeV.

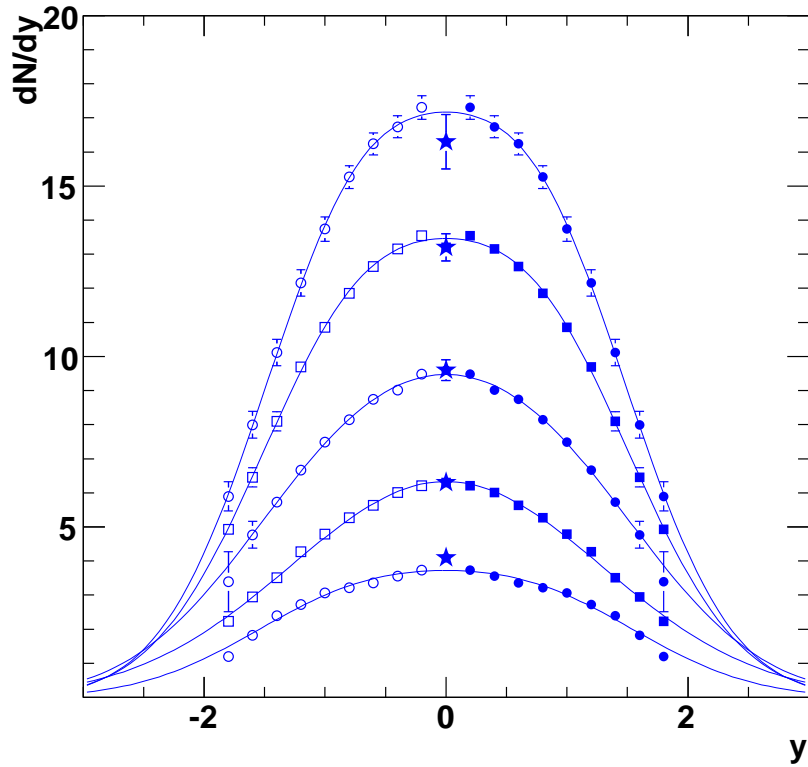


Figure 6.16:  $K^-$  rapidity distributions  $dN/dy$  for different centrality bins at 158 A-GeV beginning with centrality bin 1 at the top. The star shows the results of the time-of-flight measurements.

Centrality bin	Mean multiplicity	$dN/dy_{(y=0)}$	Integral	$y_0$	$\sigma_y$
1	$54.0 \pm 2.2 \pm 4.3$	$17.0 \pm 0.2 \pm 1.7$	54	0.76	0.83
2	$43.2 \pm 2.0 \pm 3.5$	$13.4 \pm 0.2 \pm 1.3$	43	0.77	0.86
3	$31.3 \pm 2.0 \pm 2.5$	$9.2 \pm 0.1 \pm 0.9$	31	0.75	1.00
4	$20.5 \pm 1.7 \pm 1.6$	$6.1 \pm 0.1 \pm 0.6$	20	0.01	1.29
5	$12.2 \pm 1.2 \pm 1.2$	$3.6 \pm 0.1 \pm 0.4$	12	0.78	0.92

Table 6.6: Mean multiplicities and fit parameters for double Gaussian fit of  $K^-$   $dN/dy$  spectra for different centrality bins at 158 A·GeV.

### 6.2.3 Systematic cross-checks and determination of systematic error

An estimate on the systematic error of the analysis can be derived by comparing the resulting kaon yield from different quality cuts for the track selection as well as a variation of the fixed asymmetry parameter  $\delta$  of the  $dE/dx$  function. For this analysis, several combinations have been analyzed, i.e., a minimum of 30 resp. 50 number of points for the track selection and a phi-wedge of  $30^\circ$  resp.  $50^\circ$  around the  $x$ - $z$ -plane. The asymmetry parameter  $\delta$  of the  $dE/dx$  fitting function 4.3.1 has been set to 0.06, 0.07 (standard), and 0.08. Figure 6.17 shows mid-rapidity transverse momentum spectra for  $K^+$  at 158 A·GeV for centrality bin 1 and 5 (see figure 6.20 for  $K^-$ ). The figure shows the analysis results for time-of-flight measurement and  $dE/dx$  analysis with a minimum number of 30 points and  $50^\circ$  wedge-cut resp. 50 points and  $30^\circ$  wedge-cut and their difference relative to standard  $dE/dx$  analysis. While the two  $dE/dx$  analyses are equal within the statistical errors, the TOF results are significantly lower up to 20% around  $p_T = 1$  GeV in centrality bin 1 and up to 20% higher in centrality bin 5.

At forward rapidity ( $1.5 < y < 1.7$  in figure 6.18) the  $p_t$  acceptance of the  $dE/dx$  analysis is getting limited in terms of statistics. While the differences between the 30 and 50 number of points is small, the  $dN/dy$  value depends on the extrapolation done by a single exponential fit. A variation of the fit parameters within the errors can lead to variation of the  $dN/dy$  yield of up to 5%. Figure 6.19 shows two different fits to  $K^+$  transverse momentum distribution at  $1.5 < y < 1.7$  at 158 A·GeV.

For  $K^-$  the systematic variations are smaller (figure 6.20) since the unfolding of the  $dE/dx$  spectra is easier due to the lower multiplicity of anti-protons.

At 40 A·GeV, there is a rapidity gap between the  $dE/dx$  analysis and time-of-flight measurement. Figure 6.21 shows a comparison of the first fully reliable rapidity bin

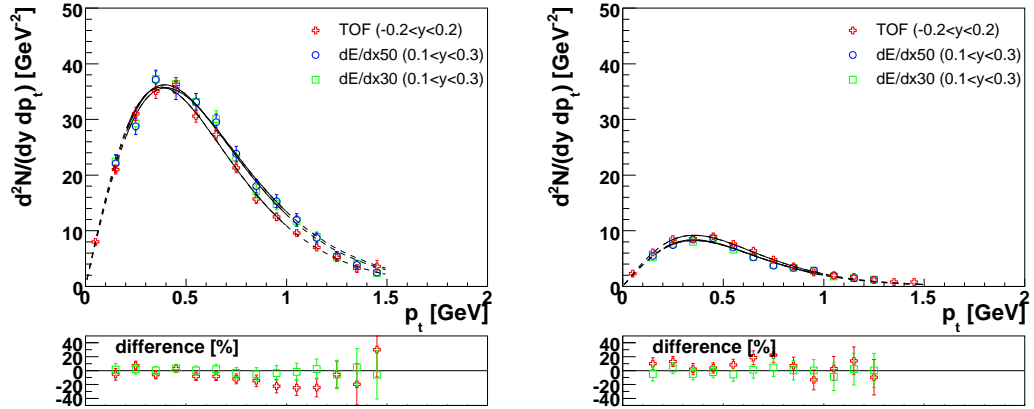


Figure 6.17:  $K^+$  transverse momentum distributions are shown on the top part at mid-rapidity for time-of-flight measurement and  $dE/dx$  analysis with a minimum number of 30 resp. 50 points for centrality bin 1 (left) and 5 (right) at 158 A·GeV. On the bottom part, the difference relative to the standard  $dE/dx$  analysis with 50 points is shown.

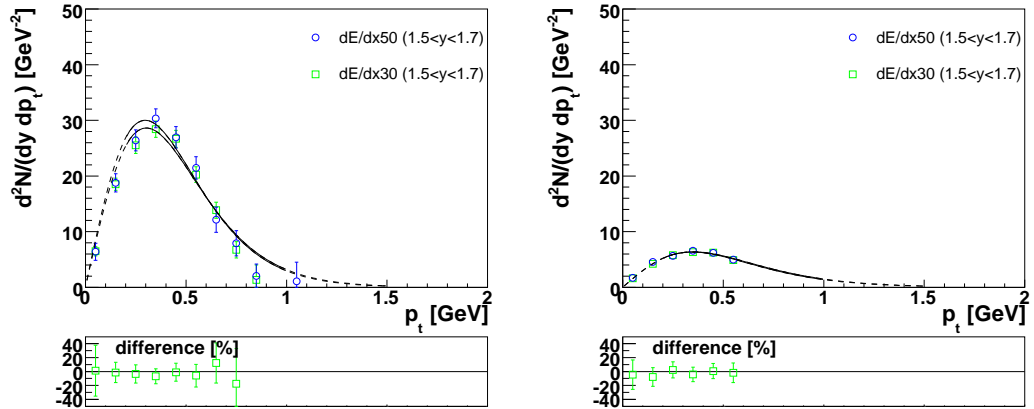


Figure 6.18:  $K^+$  transverse momentum distributions are shown on the top part at  $1.5 < y < 1.7$  for  $dE/dx$  analysis with a minimum number of 30 resp. 50 points for centrality bin 1 (left) and 5 (right) at 158 A·GeV. On the bottom part, the difference relative to the standard  $dE/dx$  analysis with 50 points is shown.

( $0.6 < y < 0.8$ ) and the time-of-flight measurement. No major systematical difference is visible.

Figures 6.22 and 6.23 show the derived mean multiplicity for kaons at 158 and 40 A·GeV for different systematic variations. The systematic error of the total

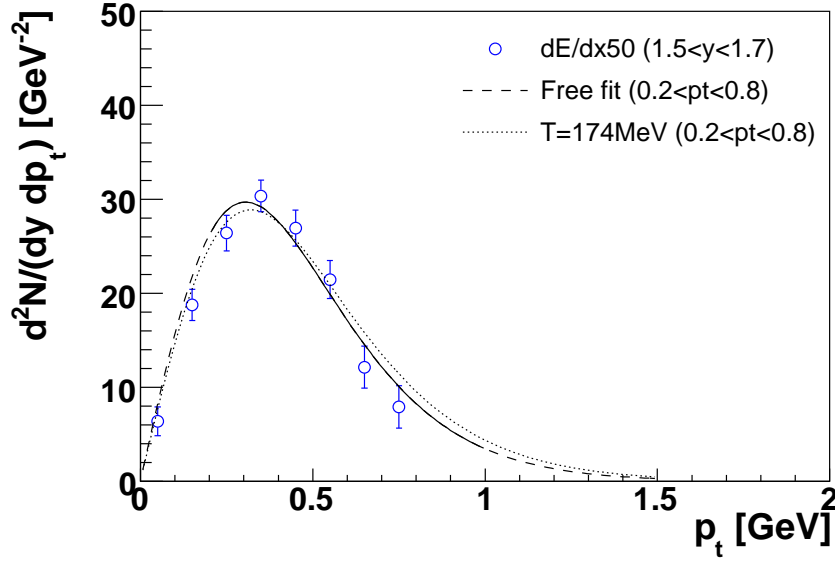


Figure 6.19: Two different fits to  $K^+$  transverse momentum distribution at  $1.5 < y < 1.7$  for  $dE/dx$  analysis at 158 A·GeV.

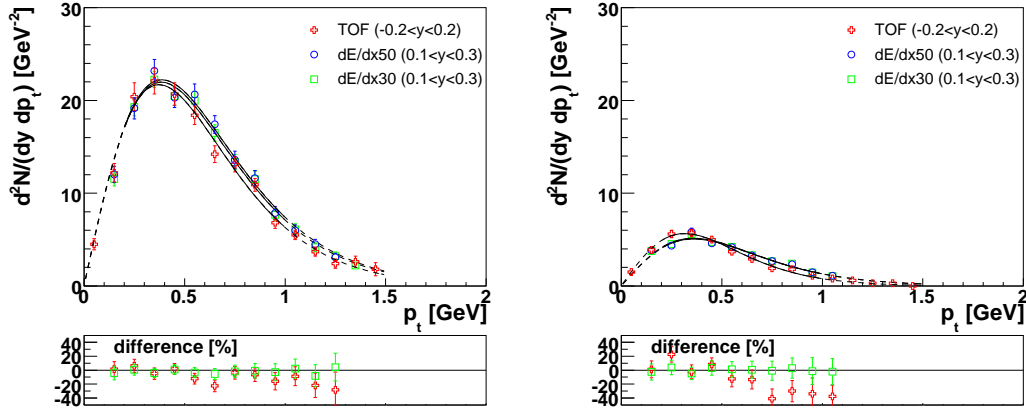


Figure 6.20:  $K^-$  transverse momentum distributions at mid-rapidity for time-of-flight measurement,  $dE/dx$  analysis with a minimum number of 30 and 50 points for centrality bin 1 and 5 at 158 A·GeV.

yield is about 8% for the centrality bins 1 to 4 and 10% for centrality bin 5. This higher error is due to the uncertainties of the event selection for the most peripheral centrality bin. Analysis 5 of the 00Ma data set in figure 6.10 deviates as much from the standard analysis. The midrapidity measurement has a systematical error of about 10%.

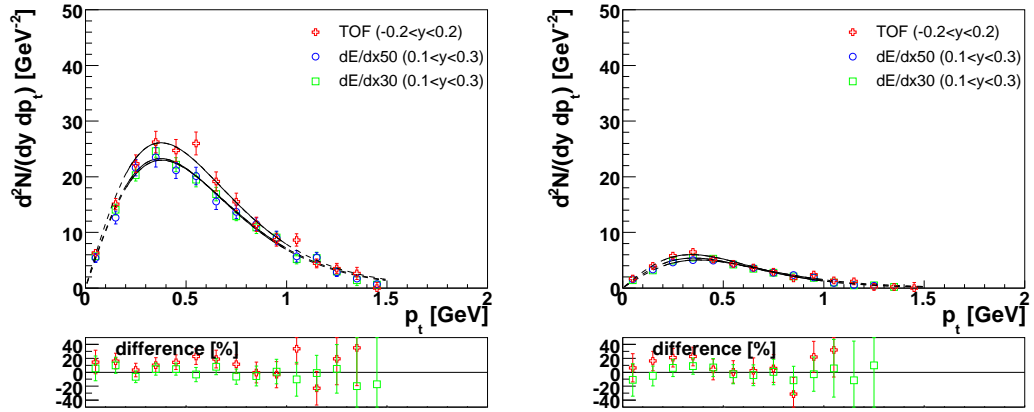


Figure 6.21:  $K^+$  transverse momentum distributions are shown on the top part at mid-rapidity for time-of-flight measurement and  $dE/dx$  analysis with a minimum number of 30 resp. 50 points for centrality bin 1 (left) and 5 (right) at 40 A·GeV. On the bottom part, the difference relative to the standard  $dE/dx$  analysis with 50 points is shown.

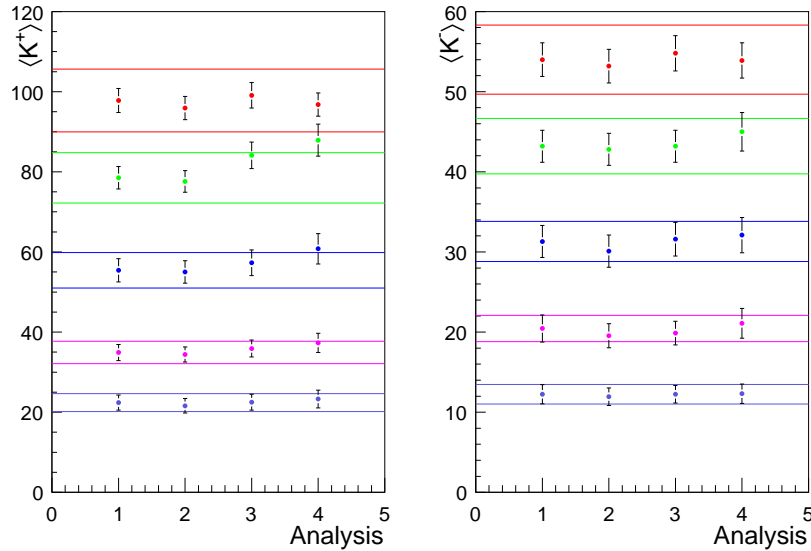


Figure 6.22: Mean multiplicities for  $K^+$  (left)  $K^-$  (right) at 158 A·GeV for the different centrality bins. Analysis 1 is the standard analysis with a minimum number of 50 points and a fixed asymmetry parameter  $\delta$  of 0.07, analysis 2 with a  $\delta$  of 0.06, analysis 3 with a  $\delta$  of 0.08, and analysis 4 with with a minimum number of 30 points, a wedge-cut of  $\pm 50^\circ$ , and a  $\delta$  of 0.07. The colored lines indicate the systematic errors.

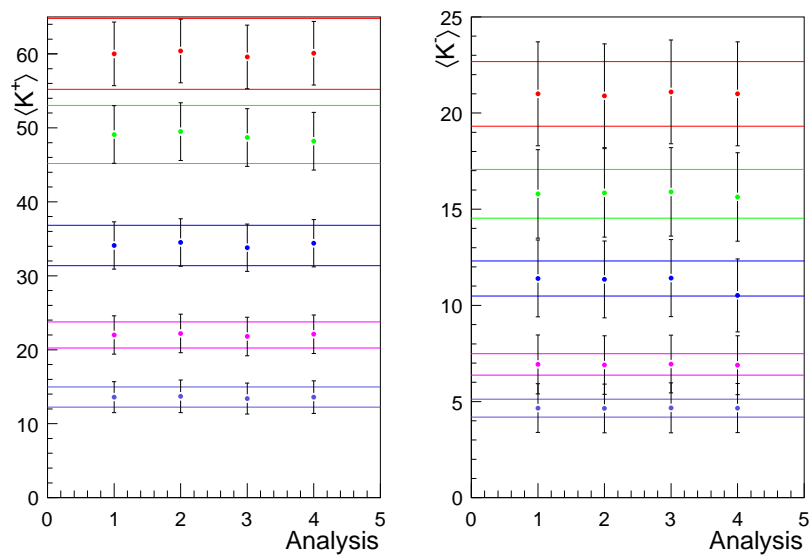


Figure 6.23: Mean multiplicities for  $K^+$  (left)  $K^-$  (right) at 40 A-GeV for the different centrality bins. Analysis 1 is the standard analysis with a minimum number of 50 points and a fixed asymmetry parameter  $\delta$  of 0.07, analysis 2 with a  $\delta$  of 0.06, analysis 3 with a  $\delta$  of 0.08, and analysis 4 with with a minimum number of 30 points, a wedge-cut of  $\pm 50^\circ$ , and a  $\delta$  of 0.07. The colored lines indicate the systematic errors of 8% for centrality bins 1 to 4 and 10% for centrality bin 5.



# 7 Discussion

The results from the two previous chapters are now discussed in comparison to results from central Pb+Pb events at various energies and to results from other experiments. First, the characteristics of the spectra are analyzed. Second, the results of kaons and pions are combined to form ratios to take out trivial effects of the increased beam energy and differences of the collision systems. They are compared with the measurements from smaller systems (p+p, C+C, and Si+Si) and at different beam energies.

## 7.1 Spectra characteristics

### 7.1.1 Transverse momentum spectra

Transverse mass  $m_t - m_0$  spectra are good to compare particle spectra with different masses. In case of a thermal source, the kinematic motion leads to higher transverse momentum the higher the mass of the particle is (see figure 7.5). Plotting transverse mass  $m_t - m_0$  spectra takes this effect out (see figure 7.4).



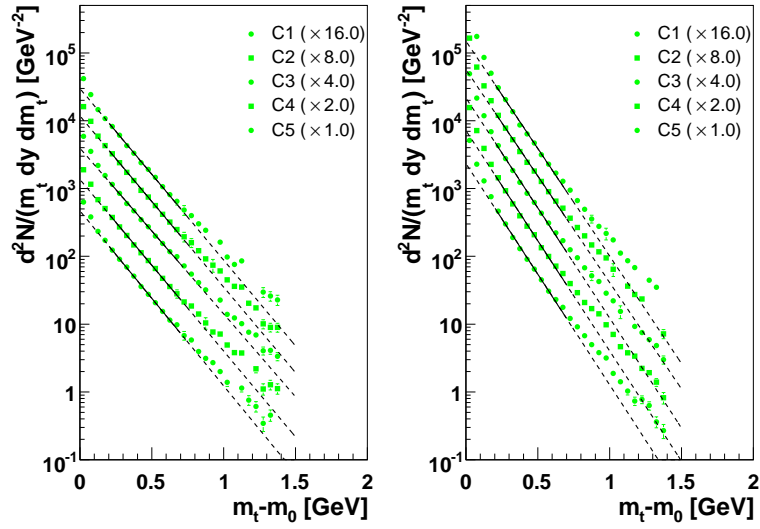


Figure 7.1: Transverse mass spectra for  $\pi^-$  at mid-rapidity at 40 (left) and 158 A-GeV (right). The solid line indicates the fit range for a single exponential function. The extrapolation of the single exponential function is drawn by a dashed line.

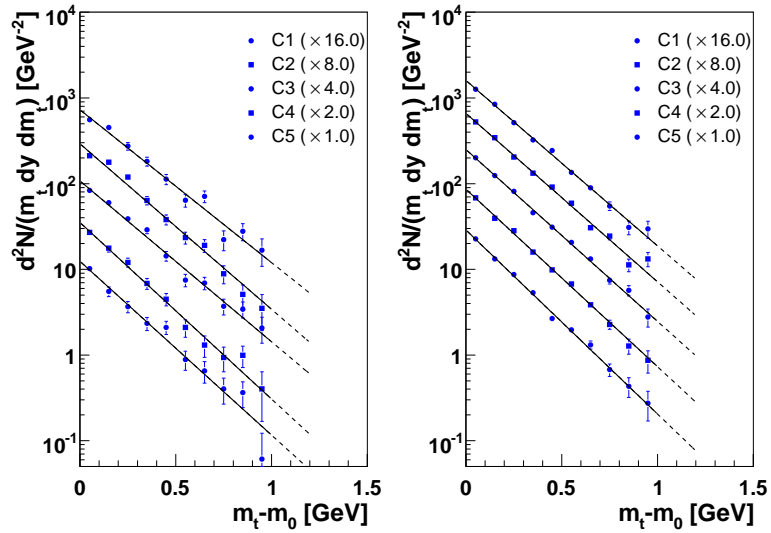


Figure 7.2: Transverse mass spectra from time-of-flight measurement for  $K^-$  at mid-rapidity at 40 (left) and 158 A-GeV (right). The solid line indicates the fit range for a single exponential function. The extrapolation of the single exponential function is drawn by a dashed line.

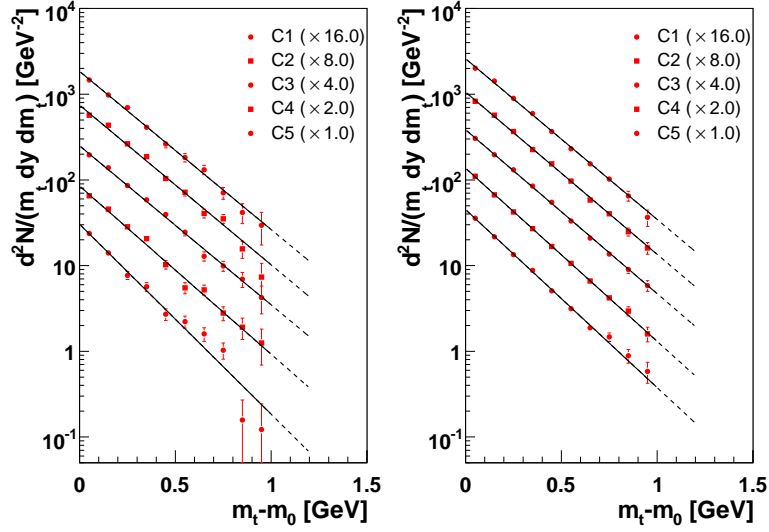


Figure 7.3: Transverse mass spectra from time-of-flight measurement for  $K^+$  at mid-rapidity at 40 (left) and 158 A·GeV (right). The solid line indicates the fit range for a single exponential function. The extrapolation of the single exponential function is drawn by a dashed line.

The mean transverse mass  $\langle m_t \rangle - m_0 = \frac{\Sigma N_i m_t}{N} - m_0$  lies for pions around 250 MeV. It is almost independent on the centrality of the collision and does not change significantly between 40 and 158 A·GeV. For  $K^-$  and  $K^+$  it rises from around 250 MeV for peripheral collisions to around 300 MeV for central collisions (see figure 7.4). Figure 7.5 shows a similar behavior for the fitted inverse slope parameter  $T$  in the range from  $0.2 \text{ GeV} < m_t - m_0 < 0.7 \text{ GeV}$  for  $\pi^-$ ,  $K^-$ , and  $K^+$ . The lower inverse slope parameter and mean transverse momentum for kaons in more peripheral collisions could stem from a decrease of collective flow [Alt03]. The lower the collective behaviour in the transverse plane, the lower the mean transverse mass will be.

At higher collision energies at the RHIC experiment STAR, pions also have a rather flat dependence with system size and kaons show a rising trend to higher transverse momenta for central collisions (figure 7.6). This is consistent with the measurements of collective flow [Adl01, Vol07].

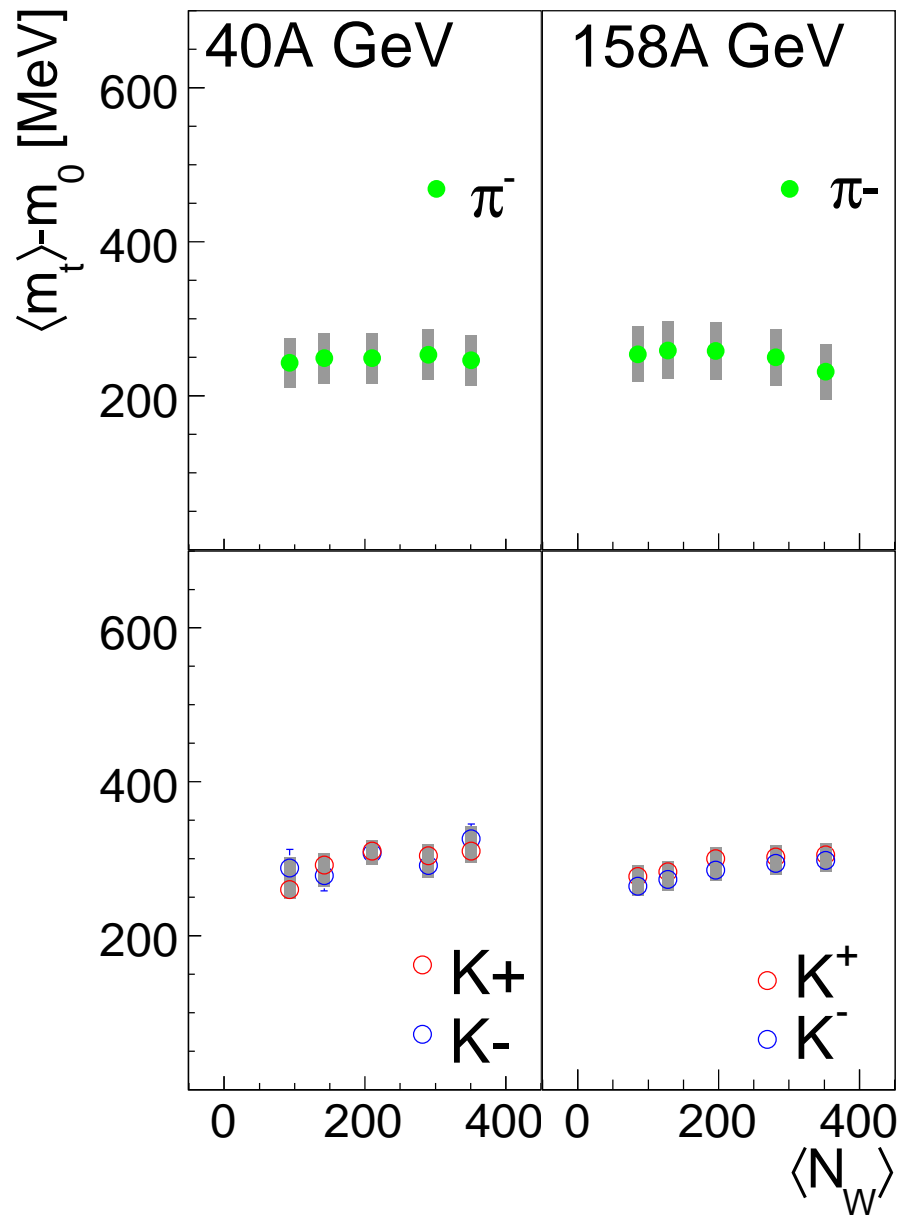


Figure 7.4: Mean transverse mass for the five centrality bins for  $\pi^-$ ,  $K^-$ , and  $K^+$  at mid-rapidity at 40 (left) and 158 A·GeV (right).

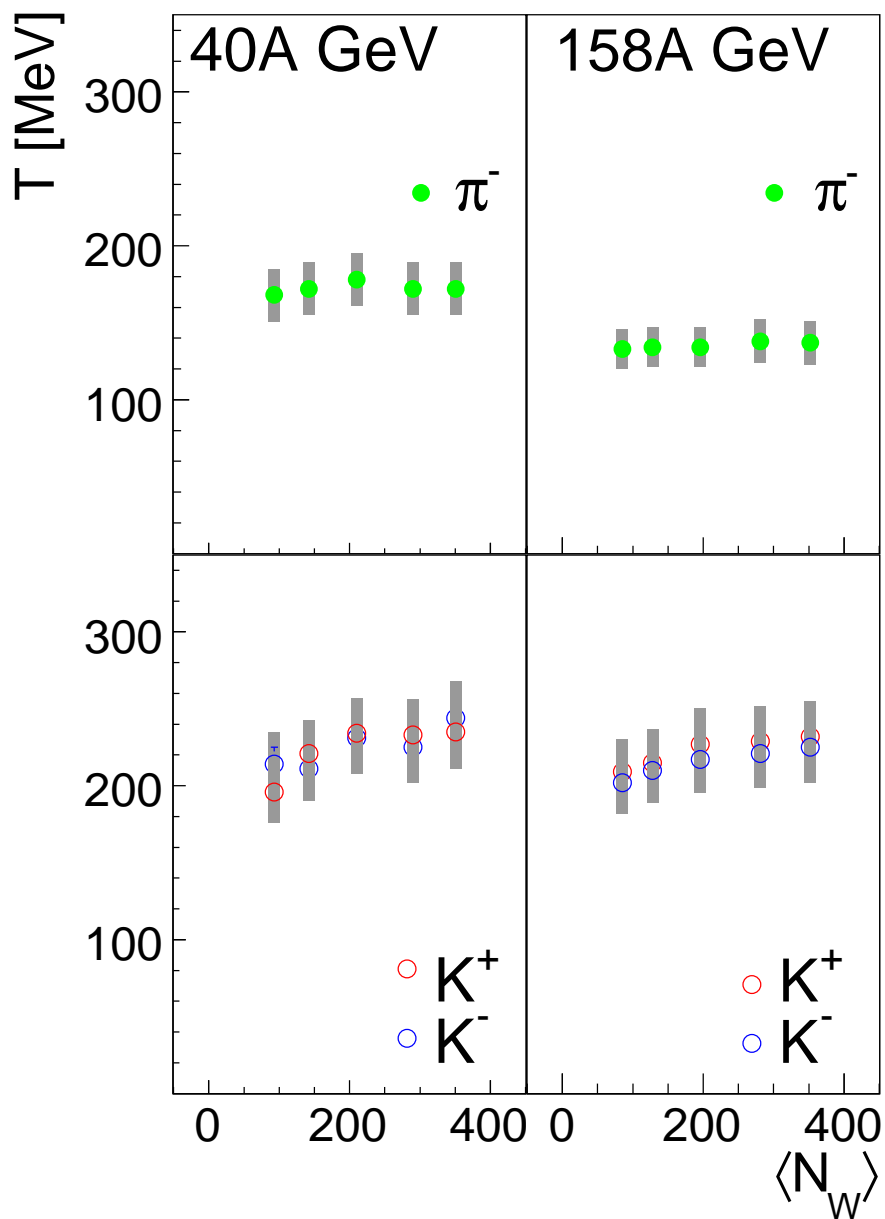


Figure 7.5: Fitted inverse slope parameter  $T$  in the range from  $0.2 < m_t - m_0 < 0.7$  at mid-rapidity for the five centrality bins for  $\pi^-$ ,  $K^-$ , and  $K^+$  at 40 (left) and 158 A·GeV (right).

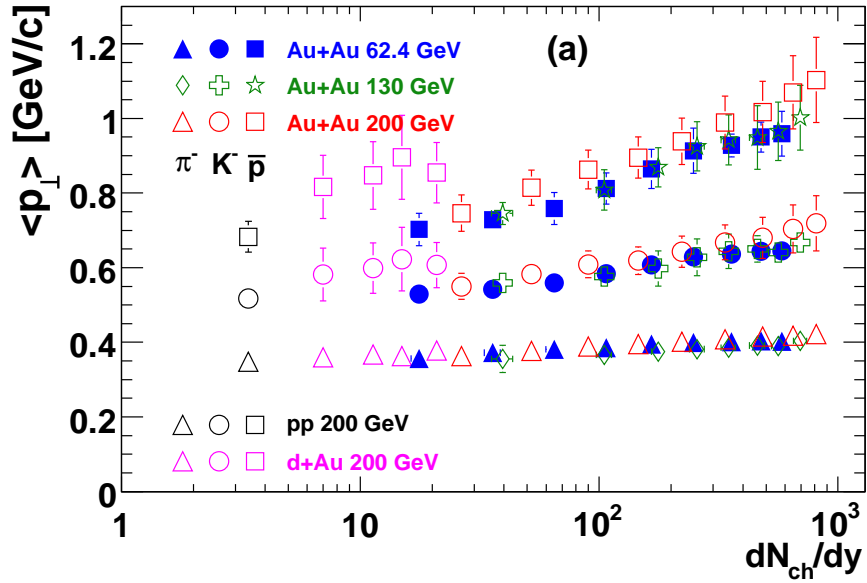


Figure 7.6: System size dependence of mean transverse momentum for various collision systems and energies from STAR experiment [Abe08].

### 7.1.2 Rapidity spectra

The presented rapidity spectra can be compared to model calculation from URQMD [Mit09] and HSD [Br09]. Where at 40 A·GeV both models agree to the experimental data for  $\pi^{-}$ , at 158 A·GeV the model calculations predict higher results around mid-rapidity. The difference gets more pronounced for central events (see figure 7.7).

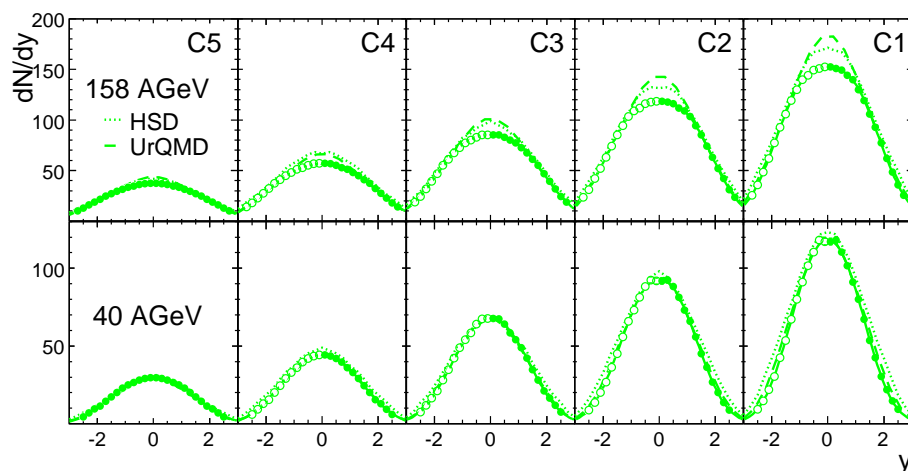


Figure 7.7:  $\pi^-$  rapidity spectra for the five centrality bins. The lines indicate URQMD (dashed) [Mit09], HSD (dotted) [Brt09] model calculations, and a double Gaussian fit (solid).

$K^-$  and  $K^+$  rapidity spectra are well reproduced by HSD model calculation at 158 A-GeV, whereas URQMD predicts lower yields. At 40 A-GeV both underestimate the yield with higher deviations for the more central bins.

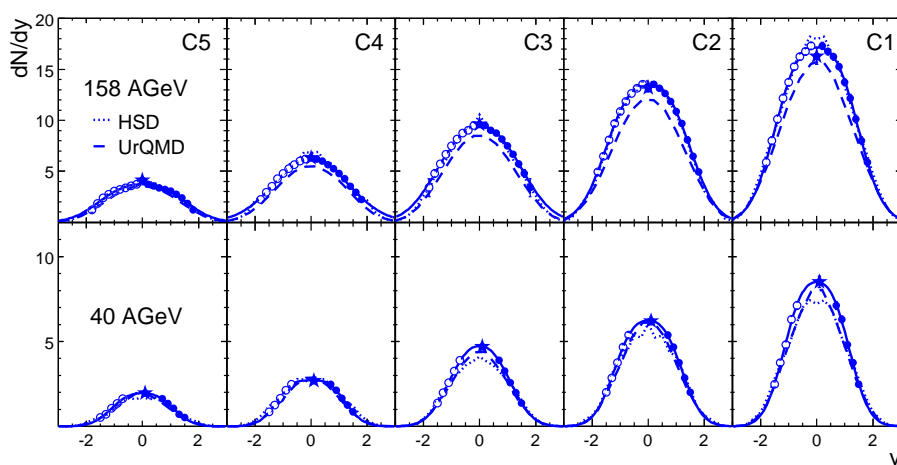


Figure 7.8:  $K^-$  rapidity spectra for the five centrality bins. The lines indicate URQMD (dashed) [Mit09], HSD (dotted) [Brt09] model calculations, and a double Gaussian fit (solid).

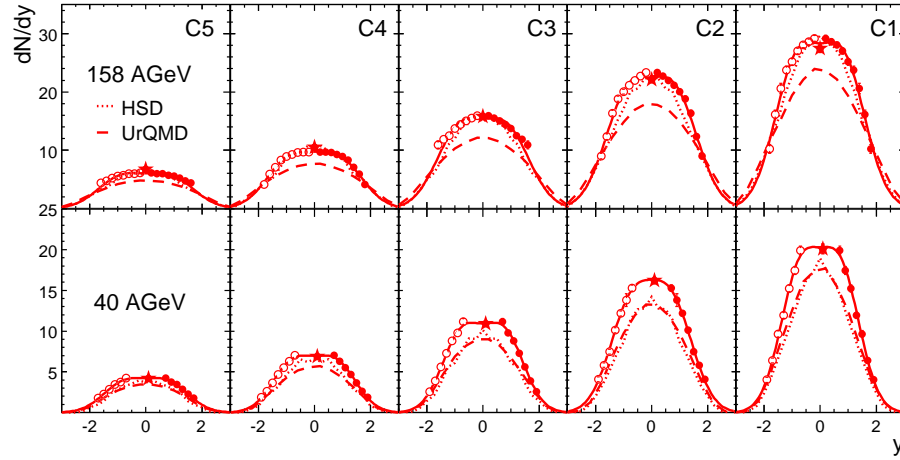


Figure 7.9:  $K^+$  rapidity spectra for the five centrality bins. The lines indicate URQMD (dashed) [Mit09], HSD (dotted) [Br09] model calculations, and a double Gaussian fit (solid).

The rapidity spectra are fitted with a double Gaussian (see equation 6.2.2). A measure of the width of the distribution is root-mean-square (RMS) which can be calculated from the fit parameters of the double Gaussian:

$$RMS = \sqrt{\sigma^2 + y_0^2} \quad (7.1.1)$$

with  $\sigma$  as the width of the Gaussians and  $y_0$  as the rapidity shift. While the dependence of the width of the rapidity distributions on the centrality of the collision is flat within errors for kaons, for pions the rapidity spectra get broader for peripheral events. The increased production of pions closer to beam and target rapidities could stem from increased production from excited nucleons. The stopping of the nucleons is decreased for peripheral collisions, since the cores of the nuclei are beginning to traverse through the more dilute surfaces of the other. For C+C and Si+Si collisions the width is on the order of central Pb+Pb. There, the nucleus is compact without a dilute surface. The Core-Corona model [Bec05, Aic08] describes Pb+Pb collisions as a combination of single nucleon-nucleon collisions and multiply colliding nucleons (for a comparison to data see below). Recent measurement of protons and anti-protons at 158 A-GeV show the decreased stopping in the ratio of forward rapidity to mid-rapidity protons vs. centrality of the collision [Utv09].

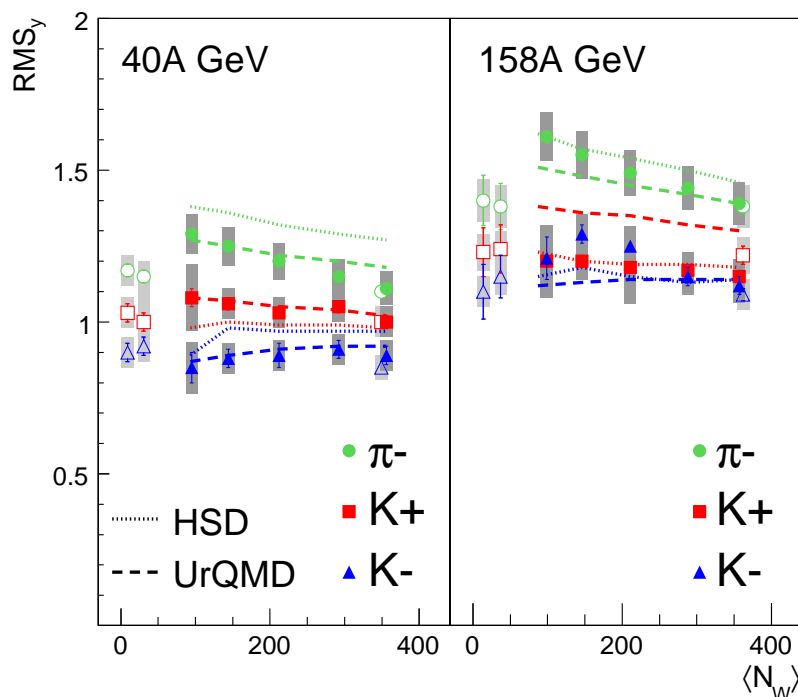


Figure 7.10: Width of rapidity distribution shown as root-mean-square (RMS) for  $\pi^-$ ,  $K^-$ , and  $K^+$  at 40 (left) and 158 A·GeV (right). Open symbols indicate measurements from C+C, Si+Si [Din05][Alt04b], and central Pb+Pb [Afa02]. The lines indicate URQMD (dashed) [Mit09] and HSD (dotted) [Br09] model calculations.

## 7.2 Particle multiplicities

### 7.2.1 Strangeness conservation

A simple cross-check for the total multiplicity measured for kaons is the comparison with other strangeness-carrying particles like  $\Lambda$  and  $\Xi$  [Ant09] since the net strangeness has to be zero. The contribution of other strangeness-carrying particles can be determined relative to  $\Lambda$ , i.e.,  $\Sigma$  (factor 1.6 from p+p collisions [Wro85]), are strangeness neutral like  $\Phi$ , or are rare like  $\Omega$  and can be neglected. The main strangeness-carrying particles are

$$\langle s \rangle \approx K^+ + \bar{K}^0 + (\Lambda + \Sigma^0) + \Sigma^+ + \Sigma^- + 2\Xi^0 + 2\Xi^-$$



and

$$\langle \bar{s} \rangle \approx K^- + K^0 + (\bar{\Lambda} + \bar{\Sigma}^0) + \bar{\Sigma}^+ + \bar{\Sigma}^- + 2\bar{\Xi}^0 + 2\bar{\Xi}^+$$

Table 7.1 summarizes the summands of the following equation

$$1.6(\Lambda - \bar{\Lambda}) + 4(\Xi^- - \Xi^+) - 2(K^+ - K^-) = \text{Netstrangeness} \quad (7.2.1)$$

Within the systematical errors the measured net strangeness is consistent with zero and fulfills strangeness conservation.

Centrality bin	$1.6(\Lambda - \bar{\Lambda}) +$	$4(\Xi^- - \Xi^+) -$	$2(K^+ - K^-) =$	Net strangeness
40 A·GeV				
1	$65 \pm 8$	11	78	$-2 \pm 8$
2	$54 \pm 6$	7	66	$-5 \pm 6$
3	$37 \pm 5$	4	44	$-3 \pm 5$
4	$26 \pm 3$	3	30	$-1 \pm 3$
5	$16 \pm 2$	2	18	$0 \pm 2$
158 A·GeV				
1	$83 \pm 15$	14	88	$9 \pm 15$
2	$69 \pm 11$	9	72	$6 \pm 11$
3	$48 \pm 8$	5	48	$5 \pm 8$
4	$29 \pm 5$	4	28	$5 \pm 5$
5	$18 \pm 3$	2	20	$0 \pm 3$

Table 7.1: Calculation of net strangeness derived from predominant particle types. The  $\Lambda$  and  $\Xi$  yields are taken from [Ant09]. Only the largest systematical error from the  $\Lambda$  analysis is shown. Statistical errors and the systematical errors for the other particles are lower and are excluded for reason of simplicity.

## 7.2.2 Relative multiplicities and scaling parameters

In order to remove trivial volume and energy effects from the analysis several relative multiplicities are derived. The centrality of the collision can be tested against scaling parameters like number of wounded nucleons [Bia76] and number of quark participants [Ani77, Bia77] (table 7.2 shows the values for the different centrality bins). If particle production scales with a certain parameter like number of wounded nucleons, the relevant production processes can be interpreted in this context. For the relative particle production, an additional model could be used to compare the data to. The

Core-Corona model [Bec05, Aic08] (see section 2.5) is applied to the measured observables by taking the values from the most central Pb+Pb collisions and p+p measurements (parameterized from close-by measurements for 40 A·GeV) with a mixing ratio depending on the centrality of the collision calculated by a Glauber calculation.

A·GeV	centrality bin	$\sigma / \sigma_{inel.}$	$\langle N_{wound} \rangle$	$\langle N_{q-part} \rangle$
40	1	0-5.0%	351	832
40	2	5.0-12.5%	290	619
40	3	12.5-23.5%	210	407
40	4	23.5-33.5%	142	249
40	5	33.5-43.5%	93	156
40	Si+Si	0-29.2%	32.2	54.8
40	C+C	0-65.7%	9.3	13.6
158	1	0-5.0%	352	834
158	2	5.0-12.5%	281	639
158	3	12.5-23.5%	196	437
158	4	23.5-33.5%	128	277
158	5	33.5-43.5%	85	171
158	Si+Si	0-12.2%	37	63
158	C+C	0-15.3%	14	19

Table 7.2: Mean number of wounded nucleons and mean number of quark-participants [Boi08] for different centrality bins at 40 and 158 A·GeV and C+C and Si+Si collisions.

The dependence of pion multiplicity normalized by the number of wounded nucleons on the number of wounded nucleons (figure 7.11) shows no significant difference between small systems and Pb+Pb. From peripheral to more central Pb+Pb collisions a slight decrease is observed. There is no strong dependence of this behavior on energy. URQMD reproduces the values very well for Pb+Pb collisions, HSD slightly overpredicts the observed ratios. For peripheral collisions the slightly higher pion yield per wounded nucleon in comparison to central collisions is not described by the Core-Corona model, which assumes a monotonous evolution towards p+p collisions.

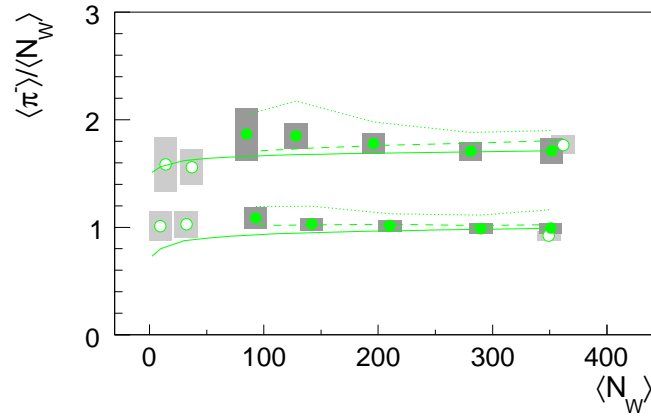


Figure 7.11:  $\pi^-$  multiplicity normalized by the number of wounded nucleons for centrality selected minimum bias Pb+Pb as well as C+C and Si+Si at 40 (lower) and 158 A-GeV(upper). Open symbols indicate measurements from C+C, Si+Si [Din05][Alt04b], and central Pb+Pb [Afa02]. The lines indicate model calculations from URQMD (dashed) [Mit09], HSD (dotted) [Brt09], and Core-Corona (solid).

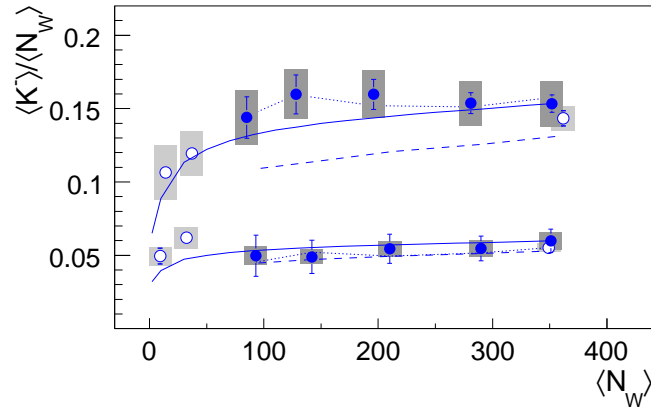


Figure 7.12:  $K^-$  multiplicity normalized by number of wounded nucleons for centrality selected minimum bias Pb+Pb as well as C+C and Si+Si at 40 (lower) and 158 A-GeV(upper). Open symbols indicate measurements from C+C, Si+Si [Din05][Alt04b], and central Pb+Pb [Afa02]. The lines indicate model calculations from URQMD (dashed) [Mit09], HSD (dotted) [Brt09], and Core-Corona (solid).

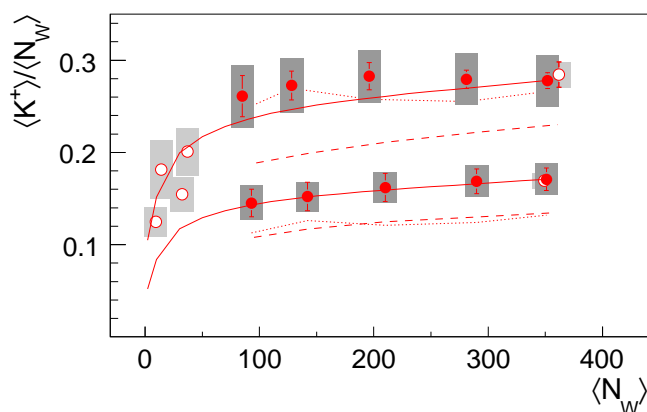


Figure 7.13:  $K^+$  multiplicity normalized by number of wounded nucleons for centrality selected minimum bias Pb+Pb as well as C+C and Si+Si at 40 (lower) and 158 A·GeV(upper). Open symbols indicate measurements from C+C, Si+Si [Din05][Alt04b], and central Pb+Pb [Afa02]. The lines indicate model calculations from URQMD (dashed) [Mit09], HSD (dotted) [Br09], and Core-Corona (solid).

At 158 A·GeV the  $K^-$  multiplicity normalized by the number of wounded nucleons (figure 7.12) rises steeply for small systems and saturates from centrality bin 5 resp. 4 onward. While HSD nicely reproduces the values for Pb+Pb collisions, URQMD underpredicts the peripheral observations by 30% improving to about 10% deviation for the most central bin. At 40 A·GeV both models reproduce the measured values, the ratio from Si+Si collisions is on the same level as central Pb+Pb. For  $K^+$  multiplicity normalized by the number of wounded nucleons (figure 7.13) the same holds true for 158 A·GeV with HSD in good agreement and a 10-30% deviation to the measured ratios for URQMD. At 40 A·GeV both model underpredict the  $K^+$  to the number of wounded nucleons ratio by 10-20%. Here, the ratio from Si+Si collisions is on the order of the central Pb+Pb measurement. The Core-Corona model describes the trend in Pb+Pb collisions very well. It lies below the measurements for C+C and Si+Si. This is to be expected since the mix of multiply colliding nucleons and single nucleon-nucleon collisions is very different for peripheral Pb+Pb and C+C resp. Si+Si at the same number of wounded nucleons.

Alternative scaling parameters are tested like the number of quark participants. While  $\pi^-$  show a stronger dependence on centrality when normalized by the number of quark participants (figure 7.14),  $K^-$  and  $K^+$  seem to scale with number of quark participants (figures 7.15 and 7.16). The pion production channel via excited nucleons is very important and could lead to the strong dependency on the number of wounded nucleons.

Since kaon production scales with the number of quark participants, the associated production of kaons, which is predominant close to the threshold energy, seems to become less relevant. Otherwise, a dependence on the number of wounded nucleons would be expected.

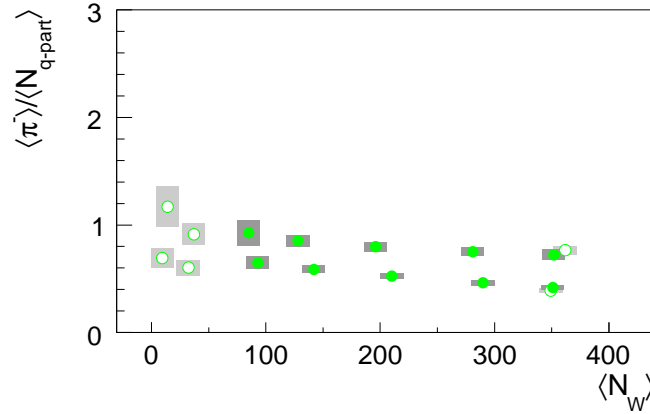


Figure 7.14:  $\pi^-$  multiplicity normalized by the number of quark participants for centrality selected minimum bias Pb+Pb. Open symbols indicate measurements from C+C, Si+Si [Din05][Alt04b], and central Pb+Pb [Afa02].

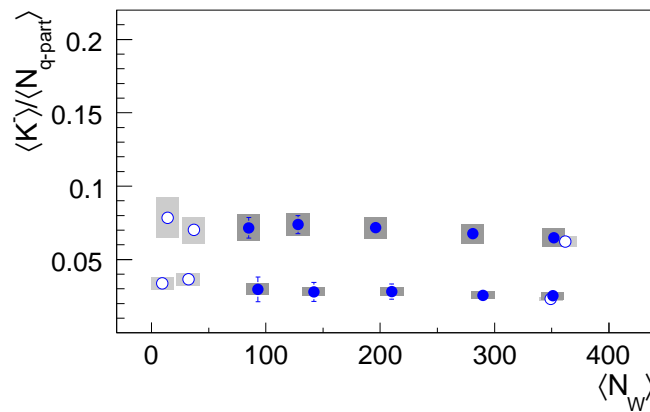


Figure 7.15:  $K^-$  multiplicity normalized by the number of quark participants for centrality selected minimum bias Pb+Pb. Open symbols indicate measurements from C+C, Si+Si [Din05][Alt04b], and central Pb+Pb [Afa02].

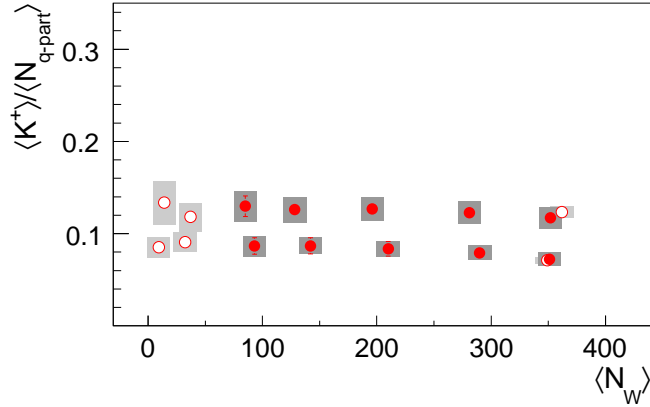


Figure 7.16:  $K^+$  multiplicity normalized by the number of quark participants for centrality selected minimum bias Pb+Pb. Open symbols indicate measurements from C+C, Si+Si [Din05][Alt04b], and central Pb+Pb [Afa02].

The  $K^+$  to  $K^-$  ratio is independent with system size. Therefore, the relative production does not change with system size.

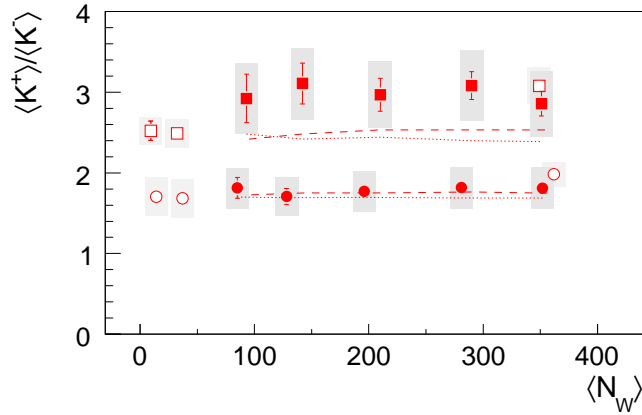


Figure 7.17:  $K^+$  multiplicity divided by  $K^-$  multiplicity for centrality selected minimum bias Pb+Pb at 40 (squares) and 158 A-GeV (circles). Open symbols indicate measurements from C+C, Si+Si [Din05][Alt04b], and central Pb+Pb [Afa02]. The lines indicate model calculations from HSD (dotted), and URQMD (dashed).

Using pion multiplicities as a measure of the entropy created in a collision, relative

production of kaons to pions are compared between different energies and collision systems. For  $K^-$ , there is a smooth evolution from the smaller systems over peripheral to central Pb+Pb collisions at 158 A·GeV. At 40 A·GeV, the measurement from Si+Si already is as high as the ratio for central Pb+Pb. HSD model calculation approximates the measurements at 40 and 158 A·GeV closely. URQMD underpredicts the ratio at 158 A·GeV. For  $K^+$ , the ratios at 40 and 158 A·GeV are equal within the errors. Regarding the connection of the trend for the smaller systems to Pb+Pb, the observation is the same as for  $K^-$ . There is a rather smooth evolution at 158 A·GeV whereas for 40 A·GeV the Si+Si measurement and peripheral Pb+Pb do not match. Both, URQMD and HSD, underpredict the measured ratios significantly. The Core-Corona model describes the trend and values very well at 158 A·GeV. C+C, Si+Si, and Pb+Pb measurements lie on the rising curve of the Core-Corona model. At 40 A·GeV, peripheral Pb+Pb collisions deviate from the Core-Corona line. The saturation there is not reached as fast as in the model prediction.

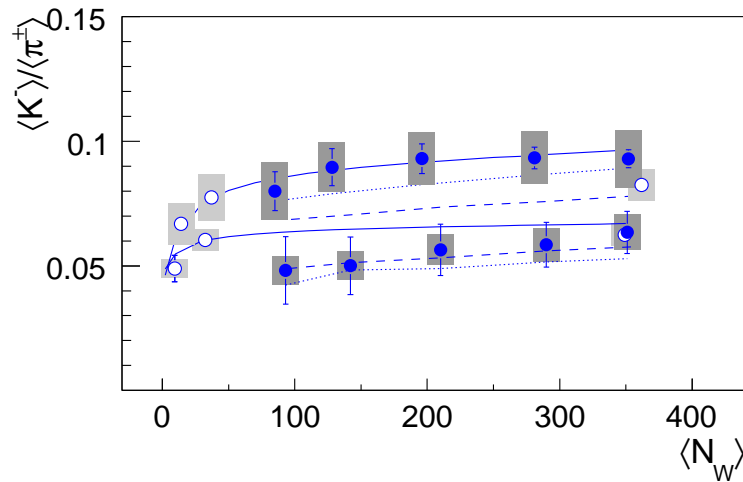


Figure 7.18:  $K^-$  multiplicity normalized by  $\pi^\pm$  multiplicity for centrality selected minimum bias Pb+Pb at 40 and 158 A·GeV. Open symbols indicate measurements from C+C, Si+Si [Din05][Alt04b], and central Pb+Pb [Afa02]. The lines indicate model calculations from URQMD (dashed) [Mit09], HSD (dotted) [Brt09], and Core-Corona (solid).

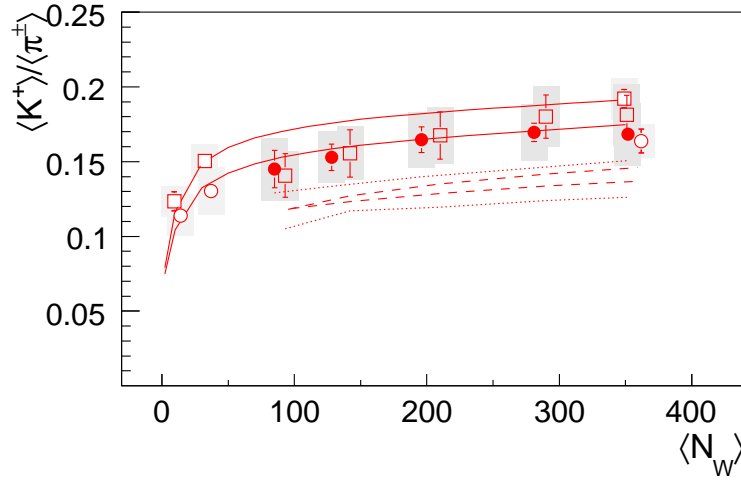


Figure 7.19:  $K^+$  multiplicity normalized by  $\pi^\pm$  multiplicity for centrality selected minimum bias Pb+Pb at 40 (squares) and 158 A-GeV (circles). Open symbols indicate measurements from C+C, Si+Si [Din05][Alt04b], and central Pb+Pb [Afa02]. The lines indicate model calculations from URQMD (dashed) [Mit09], HSD (dotted) [Br09], and Core-Corona (solid).

The evolution of the kaon to pion ratio with system size at 40 and 158 A-GeV shows no non-monotonic behaviour as observed for the energy scan of central Pb+Pb collisions (figure 7.20). Figure 7.21 shows the centrality dependence of Pb+Pb resp. Au+Au collisions for various energies (center of mass energy per nucleon pair: PHENIX at 200 GeV [Adr03], STAR at 62.4, 130, and 200 GeV [Abe08]; beam energy per nucleon: NA49 at 40 and 158 A-GeV, E802 at 11 A-GeV [Ahl99], and KAOS at 1.5 A-GeV [For04]). The measurements are normalized to the most central bin for each energy. The shape and especially the system size at which saturation sets in changes strongly with energy. Whereas there is no saturation visible at the lower energy measurements from KAOS and E802, from 40 A-GeV onwards saturation sets in at a number of wounded nucleons of about 200 decreasing to about 50 wounded nucleons at the highest RHIC energies for STAR and PHENIX experiment. The data are compared to a calculation of canonical strangeness suppression from a statistical model [Tou02]. In the context of statistical models, the relative strangeness production rises with the volume of the system. The larger reaction volume decreases the effect of local strangeness conservation for the production rate [Raf80]. The volume  $V$  is assumed to be dependent on the number of wounded nucleons  $N_W$

$$V = \frac{V_0}{2} N_W \quad (7.2.2)$$



with  $V_0 \approx 7 \text{ fm}^3$  [Ham00]. Here, the saturation is reached already at about 10 wounded nucleons, which is much earlier than observed in the data. The dilute surfaces of the lead nuclei lead to practically independent single scatterings of nucleons. Therefore, the collective effect of close-by reactions could evolve only for higher number of wounded nucleons. The collision geometry is better described by the Core-Corona model [Bec05, Aic08] (see section 2.5) or by a percolation model [Hoh05] which derives the ensemble volume from a percolation of elementary clusters. In the percolation model all cluster are formed from coalescing strings that are assumed to decay statistically with the described volume dependence of canonical strangeness suppression.

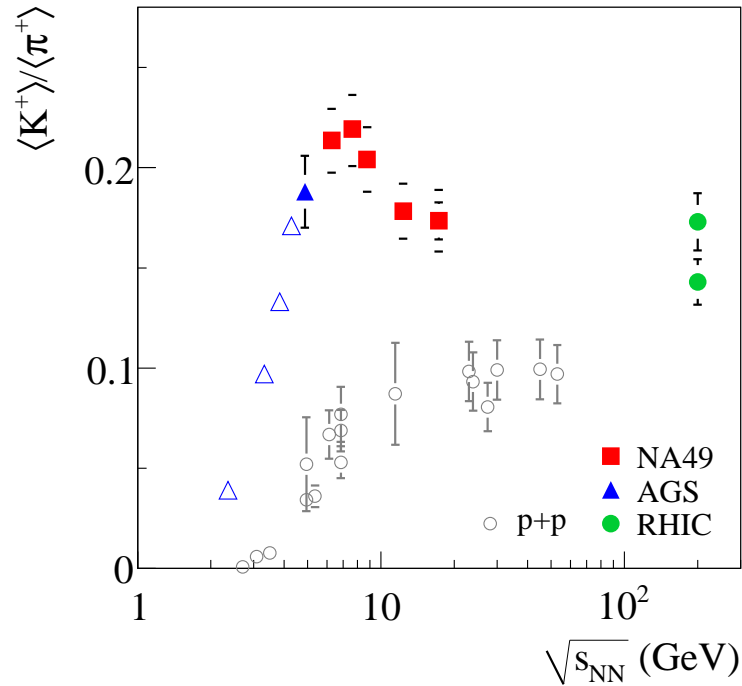


Figure 7.20: Kaon to pion ratio for central Pb+Pb collisions (full symbols) and p+p interactions (open symbols) versus beam energy [Gaz04].

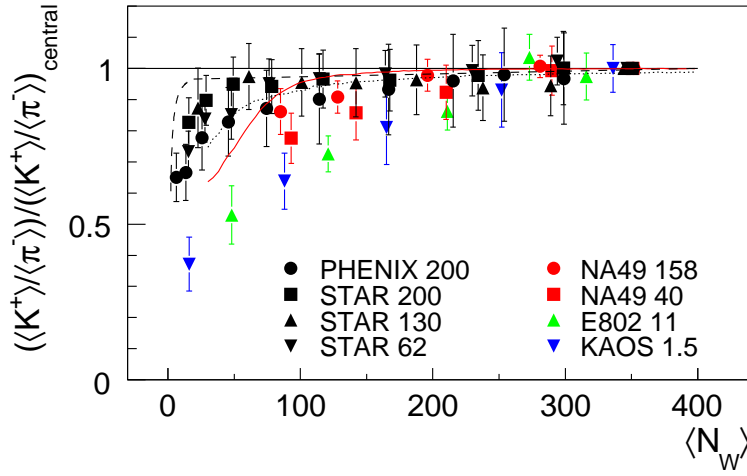


Figure 7.21:  $K^+$  multiplicity scaled by  $\pi^-$  multiplicity for centrality selected minimum bias Pb+Pb resp. Au+Au at various beam energies scaled to the ratio from the most central measurement. The lines indicate statistical model (dashed) and percolation model for RHIC (dotted) and SPS (solid) [Hoh05].

A similar behavior can be observed in the total relative strangeness production approximated by  $E_s$

$$E_s = \frac{\langle\Lambda\rangle + 2(\langle K^+\rangle + \langle K^-\rangle)}{3/2(\langle\pi^+\rangle + \langle\pi^-\rangle)}. \quad (7.2.3)$$

The  $\Lambda$  yield is taken from [Ant09]. Figure 7.22 shows the measured  $E_s$  for different centralities of Pb+Pb collisions at 40 and 158 A·GeV as well as p+p, C+C, Si+Si, S+S and central Pb+Pb at 158 A·GeV. While the expected rise from diminishing canonical suppression from a statistical model overpredicts the data, the percolation model nicely describes the centrality selected Pb+Pb as well as the smaller systems at 158 A·GeV. At 40 A·GeV, there seems to be no saturation from peripheral collisions onwards and the percolation model does not describe the data.

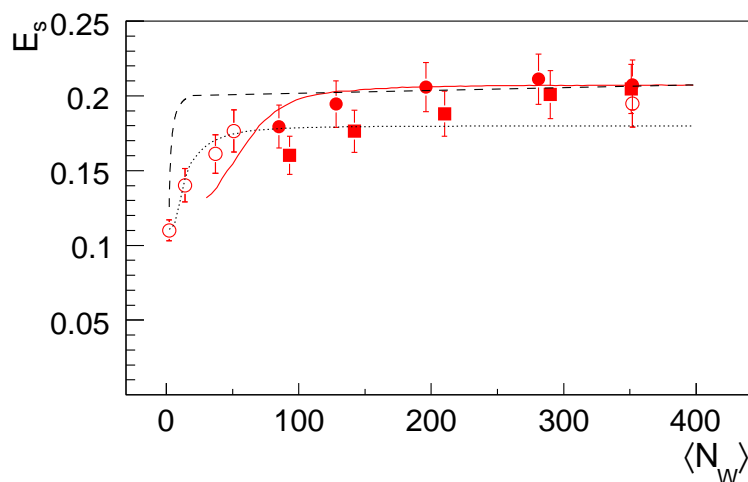


Figure 7.22: Total relative strangeness approximated by  $E_s$  for centrality selected minimum bias Pb+Pb at 40 (squares) and 158 A-GeV (circles). The open symbols are from p+p, C+C, Si+Si, S+S and central Pb+Pb at 158 A-GeV (data from [Hoh03]). The lines indicate statistical model (dashed) and percolation model for SPS small systems (dotted) and SPS Pb+Pb collisions (solid) [Hoh05].

The observed saturation of strangeness production at top SPS energy and above could be interpreted in the context of statistical models as an equilibrium of relative strangeness production. Increasing the energy available for particle production does not change the relative multiplicities of strangeness carrying particles to pions. This equilibrium has to be established before or in the process of hadronization since an equilibration by rescattering in a hadron gas could not be reached due to the fast expansion of the fire ball. This saturation could not be observed at lower energies at SIS and AGS. The measurement at 40 A-GeV is intermediate between the two. This transition lies in the vicinity of the non-monotonic behavior seen in the energy dependence of the  $K^+/\pi^-$  ratio for central collisions (figure 7.20).

The system size dependence is well described by taking into account the effect from canonical strangeness suppression for small volumes. The appropriate volume is not simply proportional to the number of wounded nucleons but takes a superposition of smaller subvolumes from single collisions into account that form low volume clusters plus a core region with multiple collisions. For the higher energies the measurements from heavy ion interactions are not very different from Si+Si and even C+C. If a partonic phase is created in Pb+Pb, then there is also a (lower volume) partonic state created in C+C. At 40 A-GeV, the relative strangeness production shows a stronger

dependence on system size for peripheral Pb+Pb. For lower energies at AGS and SIS, the dependence on system size is linear. A good description of this behavior can be derived in models that calculate rescattering in a hadron gas (e.g., RQMD [Wan99]). Statistical models also describe the observed behavior at AGS and SIS energies with a volume proportional to the number of wounded nucleons  $V \propto N_W$  [Cle98].



## 8 Summary and Conclusion

Results on charged kaon and negatively charged pion production and spectra for centrality selected Pb+Pb minimum bias events at 40 and 158 A·GeV have been presented in this thesis. All analysis are based on data taken by the NA49 experiment at the accelerator Super Proton Synchrotron (SPS) at the European Organization for Nuclear Research (CERN) in Geneva, Switzerland. The kaon results are based on an analysis of the mean energy loss  $\langle dE/dx \rangle$  of the charged particles traversing the detector gas of the time projection chambers (TPCs). The pion results are from an analysis of all negatively charged particles  $h^-$  corrected for contributions from particle decays and secondary interactions.

For the  $dE/dx$  analysis of charged kaons, main TPC tracks with a total momentum between 4 and 50 GeV have been analyzed in logarithmic momentum  $\log(p)$  and transverse momentum  $p_T$  bins. The resulting  $dE/dx$  spectra have been fitted by the sum of 5 Gaussians, one for each main particle type (electrons, pions, kaons, protons, deuterons). The amplitude of the Gaussian used for the kaon part of the spectra has been corrected for efficiency and acceptance and the binning has been transformed to rapidity  $y$  and transverse momentum  $p_T$  bins. The multiplicity  $dN/dy$  of the single rapidity bins has been derived by summing the measured range of the transverse momentum spectra and an extrapolation to full coverage with a single exponential function fitted to the measured range. The results have been combined with the mid-rapidity measurements from the time-of-flight detectors and a double Gaussian fit to the  $dN/dy$  spectra has been used for extrapolation to rapidity outside of the acceptance of the  $dE/dx$  analysis.

For the  $h^-$  analysis of negatively charged pions, all negatively charged tracks have been analyzed. The background from secondary reactions, particle decays, and  $\gamma$ -conversions has been corrected with the VENUS event generator. The results were also corrected for efficiency and acceptance and the  $p_T$  spectra were analyzed and extrapolated where necessary to derive the mean yield per rapidity bin  $dN/dy$ . The mean multiplicity  $\langle \pi^- \rangle$  has been derived by summing up the measured  $dN/dy$  and extrapolating the rapidity spectrum with a double Gaussian fit to  $4\pi$  coverage.

The results have been discussed in detail and compared to various model calculations.

Microscopical models like URQMD and HSD do not describe the full complexity of Pb+Pb collisions. Especially the production of the positively charged kaons, which carry the major part of strange quarks, cannot be consistently reproduced by the model calculations. Centrality selected minimum bias Pb+Pb collisions can be described as a mixture of a high-density region of multiply colliding nucleons (core) and practically independent nucleon-nucleon collisions (corona). This leads to a smooth evolution from peripheral to central collisions. A more detailed approach derives the ensemble volume from a percolation of elementary clusters. In the percolation model all clusters are formed from coalescing strings that are assumed to decay statistically with the volume dependence of canonical strangeness suppression. The percolation model describes the measured data for top SPS and RHIC energies. At 40 A·GeV, the system size dependence of the relative strangeness production starts to evolve from the saturation seen at higher energies from peripheral events onwards towards a linear dependence at SIS and AGS. This change of the dependence on system size occurs in the energy region of the observed maximum of the  $K^+$  to  $\pi$  ratio for central Pb+Pb collisions.

Future measurements with heavy ion beam energies around this maximum at RHIC and FAIR as well as the upgraded NA49 successor experiment NA61 will further improve our understanding of quark matter and its reflection in modern heavy ion physics and theories.

# A Kinematics

As a convention in high energy physics, the following variables are set to unity  $c = k = h = 1$ . Temperature, energy, and momentum are all expressed in units of MeV.

The total energy  $E$  of a particle can be described as

$$E = \text{sqr}(m^2 + p^2) \quad (\text{A.0.1})$$

where  $m$  is the rest mass and  $p$  is the total momentum.

The standard unit of length in heavy ion physics is typically stated in femto meter  $fm$  (often referred to as fermi meter) which corresponds to  $10^{-15}m$ . Areas are often presented in barn  $b$  which corresponds to  $100fm^2$ .

Particle spectra are usually presented vs. rapidity

$$y = \frac{1}{2} \ln \left( \frac{E + p_z}{E - p_z} \right) \quad (\text{A.0.2})$$

and transverse momentum

$$p_T = \sqrt{p_x^2 + p_y^2} \quad (\text{A.0.3})$$

where the latter is invariant to Lorentz transformation and the former's shape is Lorentz-invariant. The Lorentz transformation shift rapidity only linearly

$$y' = y + y_0 \quad (\text{A.0.4})$$

Invariant yields  $\frac{d^3N}{dpdp_T}$  can be presented in different kinematic variables:

$$E \frac{d^3N}{d\bar{p}^3} = \frac{E}{p_T} \frac{p_L}{p} \frac{d^3N}{d\phi dp dp_T} = \frac{1}{p_T} \frac{d^3N}{d\phi dy dp_T} = \frac{1}{m_T} \frac{d^3N}{d\phi dy dm_T} = \frac{E_0}{p_T p_0} \frac{d^3N}{d\phi d\chi_F dp_T} \quad (\text{A.0.5})$$



The shape of the bins changes by transforming from one kinematic variable into another (figure A.1). This can be neglected if the binning is chosen small enough. For the transformation of  $d(\log(p)) = 0.2$  into  $dy$  bins the change to the multiplicity is small. The rectangular binning of  $\log(p)-p_T$  is transformed into a non rectangular binning of  $y-p_T$  by the following equation

$$\frac{d^2 N}{dp_T dy} = E \frac{p_L}{p} \frac{d^2 N}{dp_T dp} \quad (\text{A.0.6})$$

with  $\frac{d^2 N}{dp_T dp}$  as the corrected yield determined from the  $dE/dx$  fits in each  $p-p_T$  bin. To derive  $p_T$  spectra for different rapidity bins a linear interpolation in rapidity is applied.

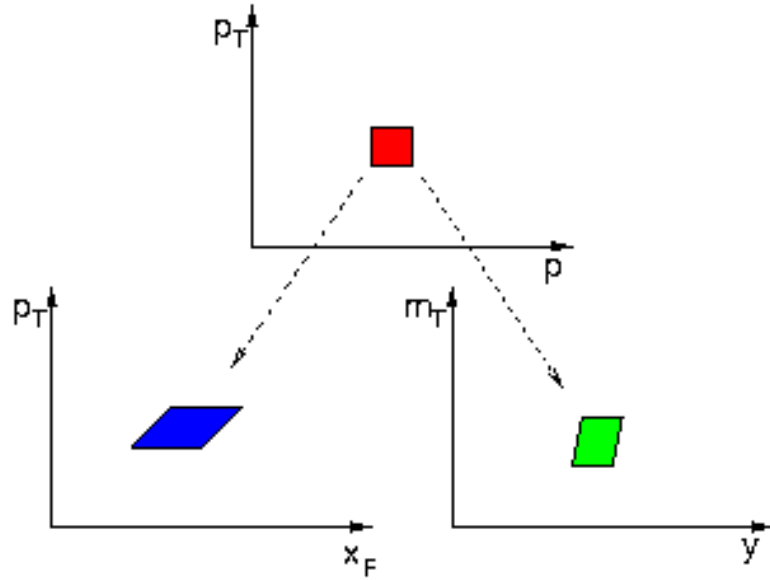


Figure A.1: Transformation of the kinematic variables changes the shape of the bins [Sik99]

## B Comparison to previous analysis

A preliminary analysis of the 158 A·GeV data had been presented at the Quark Matter Conference 1999 in Torino [Bac99]. While the results for charged kaons are within the systematical errors of the two analyses, the results for negatively charged pions deviate by about 20% for peripheral collisions.

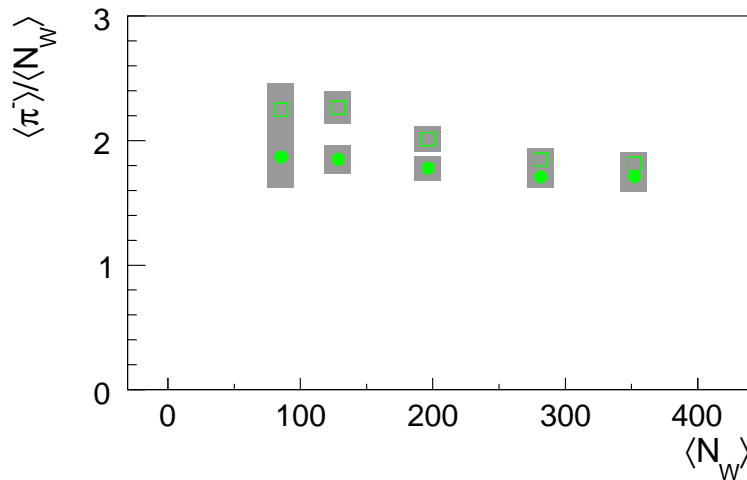


Figure B.1: Multiplicity of  $\pi^-$  normalized by the number of wounded nucleons for centrality selected minimum bias Pb+Pb collisions at 158 A·GeV. The new results are presented by circles, the old analysis [Bac99] by squares. The systematical errors are indicated by the shaded areas.

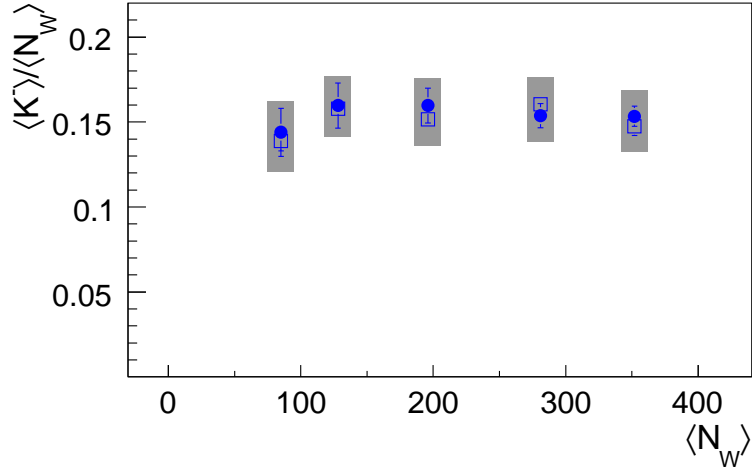


Figure B.2: Multiplicity of  $K^-$  normalized by the number of wounded nucleons for centrality selected minimum bias Pb+Pb collisions at 158 A·GeV. The new results are presented by circles, the old analysis [Bac99] by squares. The systematical errors are indicated by the shaded areas.

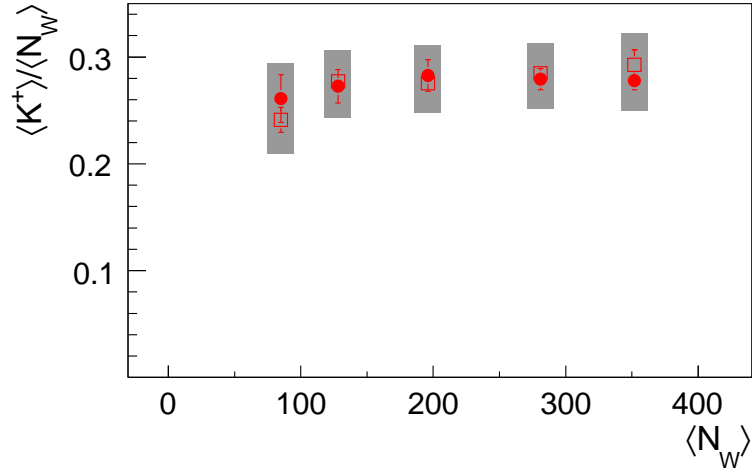


Figure B.3: Multiplicity of  $K^+$  normalized by the number of wounded nucleons for centrality selected minimum bias Pb+Pb collisions at 158 A·GeV. The new results are presented by circles, the old analysis [Bac99] by squares. The systematical errors are indicated by the shaded areas.

# C Additional plots and numerical data

Transverse momentum spectra

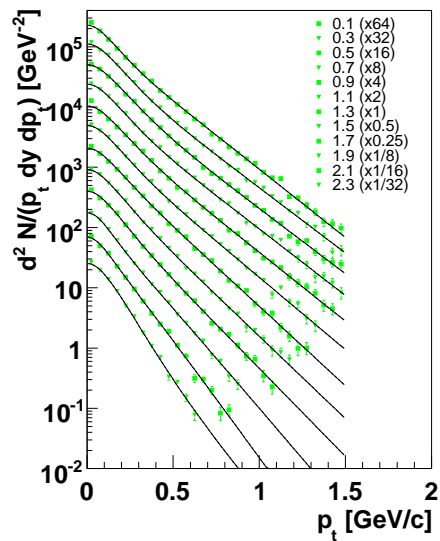


Figure C.1: Transverse momentum spectra  $1/p_T dN/dp_T$  for  $\pi^-$  for different rapidities (mid-rapidity on top) for centrality bin 1 at 40 A·GeV. The lines indicate a fit by the sum of two exponential functions.

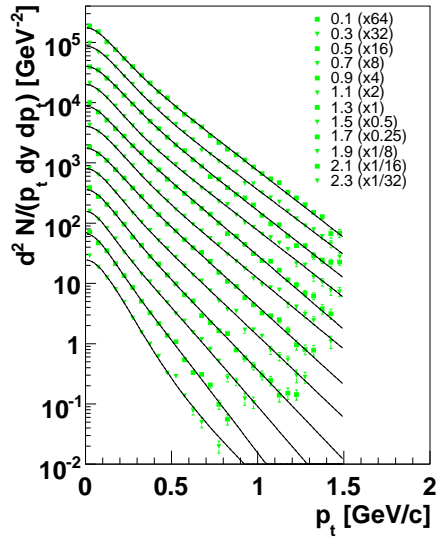


Figure C.2: Transverse momentum spectra  $1/p_T dN/dp_T$  for  $\pi^-$  for different rapidities (mid-rapidity on top) for centrality bin 2 at 40 A·GeV. The lines indicate a fit by the sum of two exponential functions.

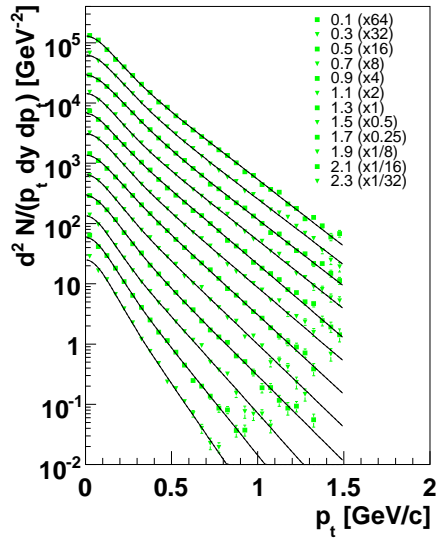


Figure C.3: Transverse momentum spectra  $1/p_T dN/dp_T$  for  $\pi^-$  for different rapidities (mid-rapidity on top) for centrality bin 3 at 40 A·GeV. The lines indicate a fit by the sum of two exponential functions.

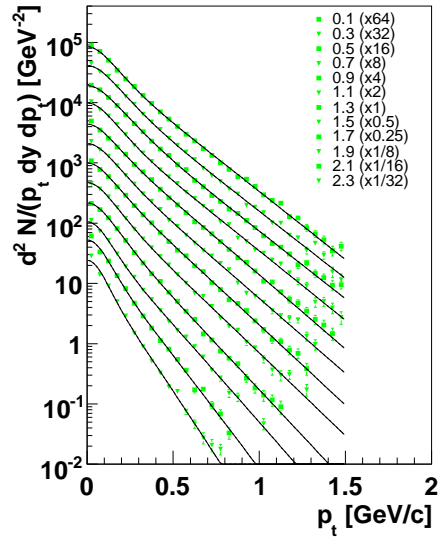


Figure C.4: Transverse momentum spectra  $1/p_T dN/dp_T$  for  $\pi^-$  for different rapidities (mid-rapidity on top) for centrality bin 4 at 40 A-GeV. The lines indicate a fit by the sum of two exponential functions.

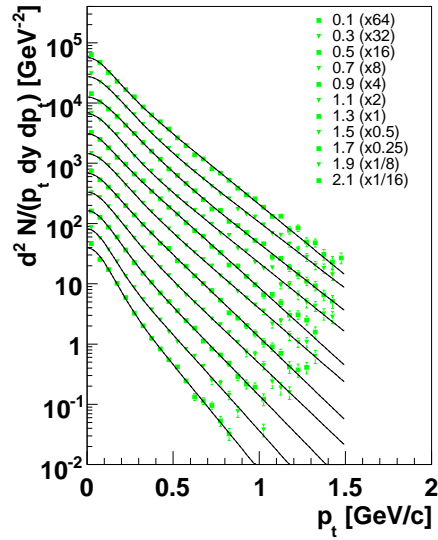


Figure C.5: Transverse momentum spectra  $1/p_T dN/dp_T$  for  $\pi^-$  for different rapidities (mid-rapidity on top) for centrality bin 5 at 40 A-GeV. The lines indicate a fit by the sum of two exponential functions.

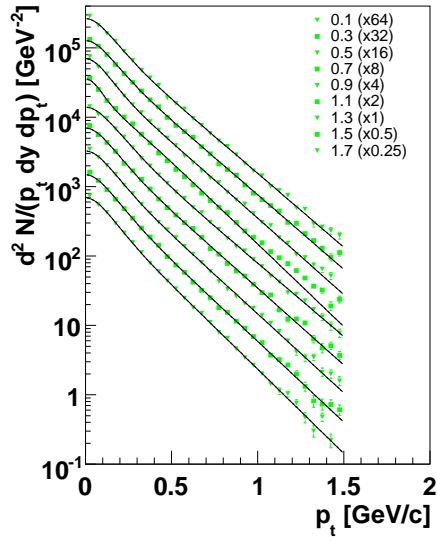


Figure C.6: Transverse momentum spectra  $1/p_T dN/dp_T$  for  $\pi^-$  for different rapidities (mid-rapidity on top) for centrality bin 1 at 158 A·GeV. The lines indicate a fit by the sum of two exponential functions.

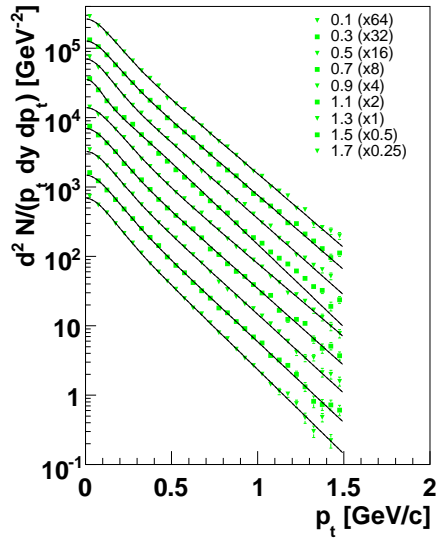


Figure C.7: Transverse momentum spectra  $1/p_T dN/dp_T$  for  $\pi^-$  for different rapidities (mid-rapidity on top) for centrality bin 2 at 158 A·GeV. The lines indicate a fit by the sum of two exponential functions.

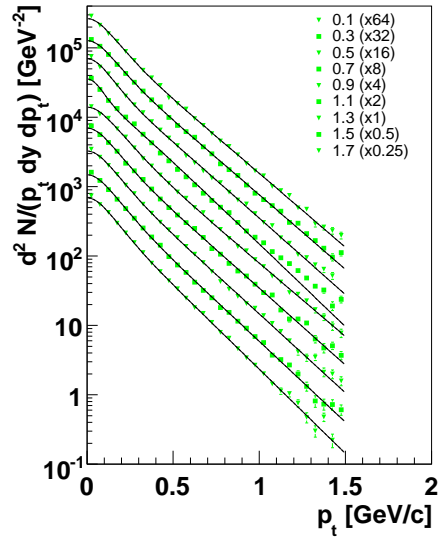


Figure C.8: Transverse momentum spectra  $1/p_T dN/dp_T$  for  $\pi^-$  for different rapidities (mid-rapidity on top) for centrality bin 3 at 158 A·GeV. The lines indicate a fit by the sum of two exponential functions.

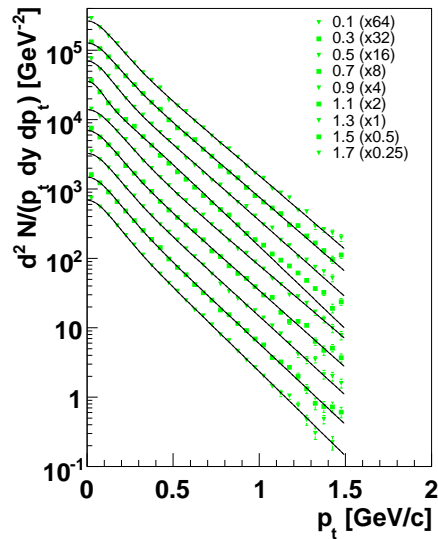


Figure C.9: Transverse momentum spectra  $1/p_T dN/dp_T$  for  $\pi^-$  for different rapidities (mid-rapidity on top) for centrality bin 4 at 158 A·GeV. The lines indicate a fit by the sum of two exponential functions.



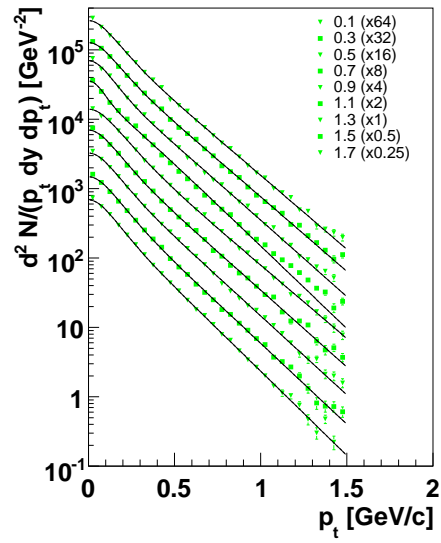


Figure C.10: Transverse momentum spectra  $1/p_T dN/dp_T$  for  $\pi^-$  for different rapidities (mid-rapidity on top) for centrality bin 5 at 158 A-GeV. The lines indicate a fit by the sum of two exponential functions.

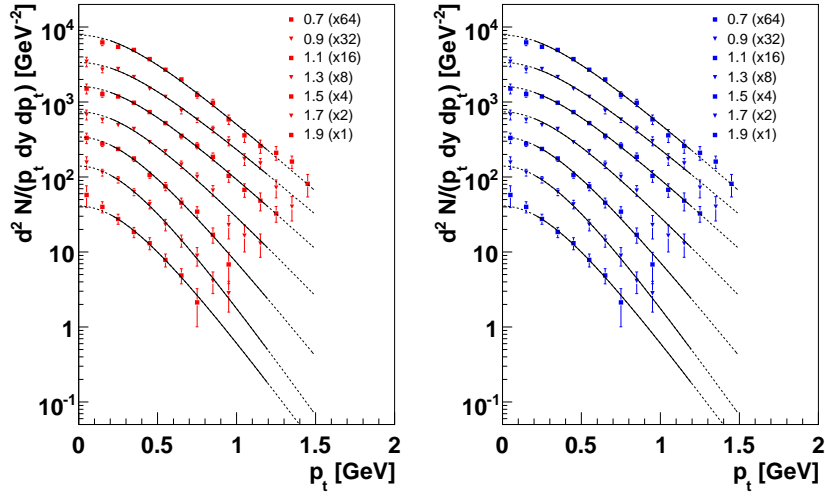


Figure C.11: Transverse momentum spectra  $1/p_T dN/dp_T$  for  $K^+$  (left) and  $K^-$  (right) for different rapidities (mid-rapidity on top) for centrality bin 1 at 40 A-GeV. The lines indicate a fit by a single exponential function (solid for fitting range).

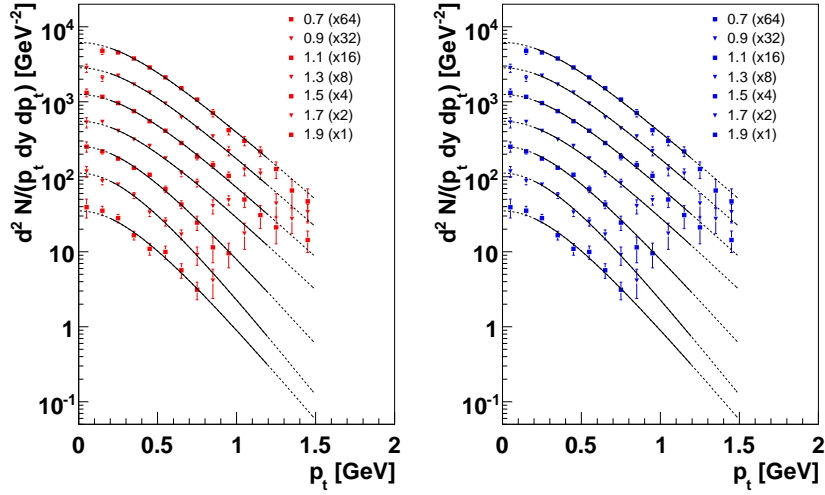


Figure C.12: Transverse momentum spectra  $1/p_T dN/dp_T$  for  $K^+$  (left) and  $K^-$  (right) for different rapidities (mid-rapidity on top) for centrality bin 2 at 40 A-GeV. The lines indicate a fit by a single exponential function (solid for fitting range).

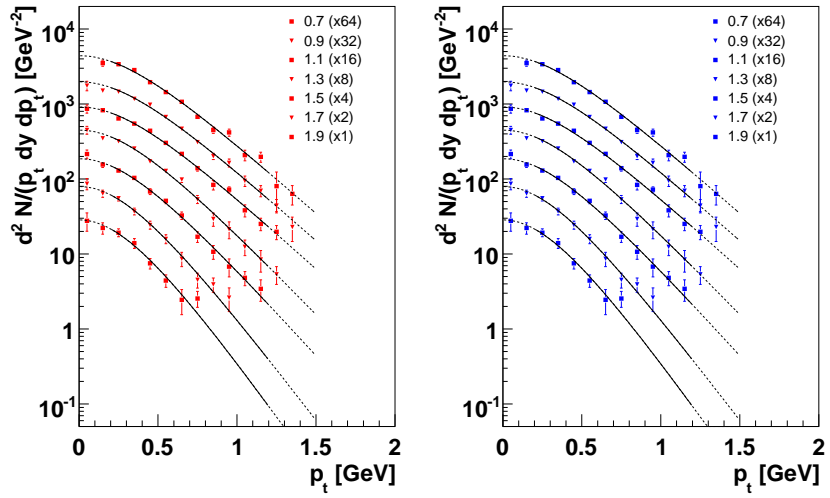


Figure C.13: Transverse momentum spectra  $1/p_T dN/dp_T$  for  $K^+$  (left) and  $K^-$  (right) for different rapidities (mid-rapidity on top) for centrality bin 3 at 40 A-GeV. The lines indicate a fit by a single exponential function (solid for fitting range).

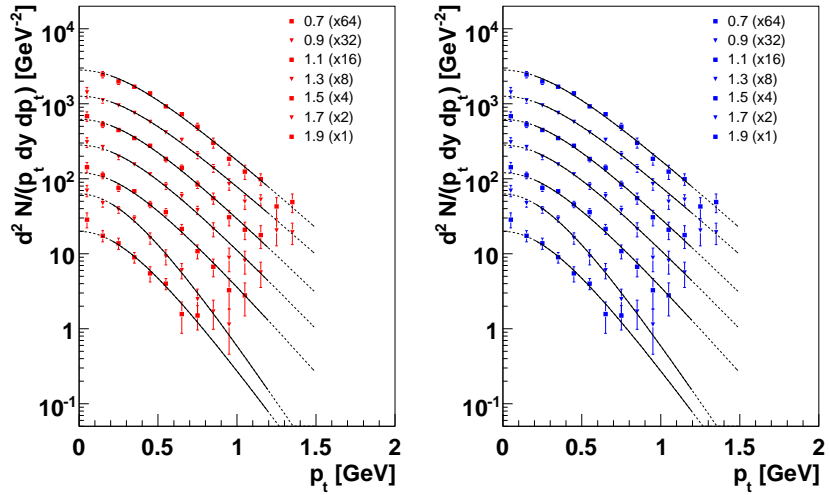


Figure C.14: Transverse momentum spectra  $1/p_T dN/dp_T$  for  $K^+$  (left) and  $K^-$  (right) for different rapidities (mid-rapidity on top) for centrality bin 4 at 40 A-GeV. The lines indicate a fit by a single exponential function (solid for fitting range).

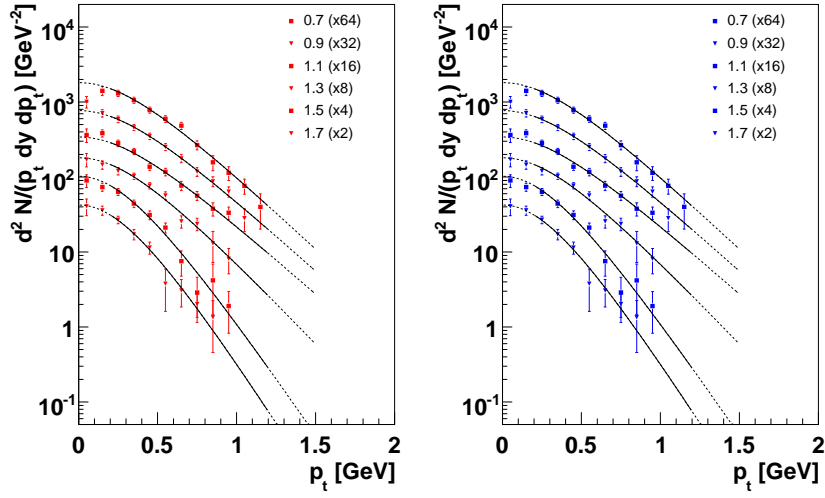


Figure C.15: Transverse momentum spectra  $1/p_T dN/dp_T$  for  $K^+$  (left) and  $K^-$  (right) for different rapidities (mid-rapidity on top) for centrality bin 5 at 40 A·GeV. The lines indicate a fit by a single exponential function (solid for fitting range).

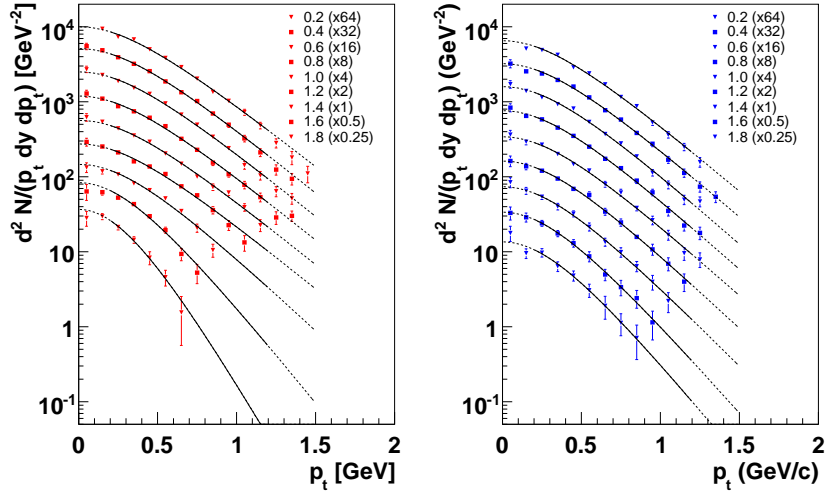


Figure C.16: Transverse momentum spectra  $1/p_T dN/dp_T$  for  $K^+$  (left) and  $K^-$  (right) for different rapidities (mid-rapidity on top) for centrality bin 1 at 158 A·GeV. The lines indicate a fit by a single exponential function (solid for fitting range).

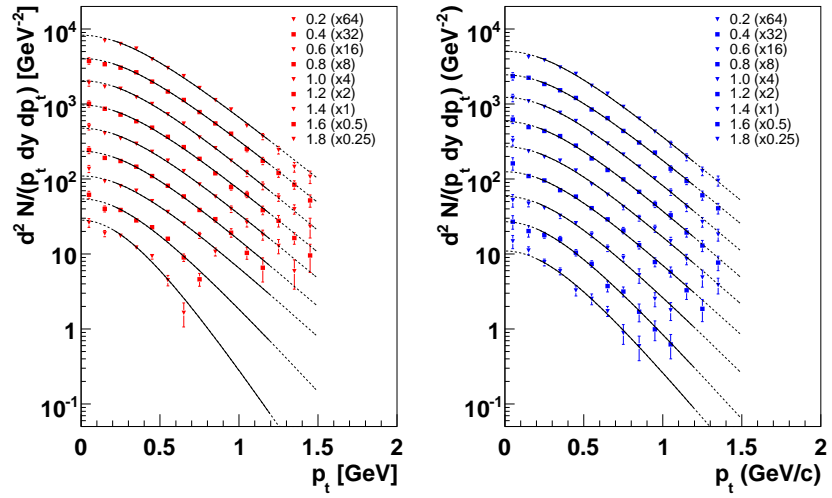


Figure C.17: Transverse momentum spectra  $1/p_T dN/dp_T$  for  $K^+$  (left) and  $K^-$  (right) for different rapidities (mid-rapidity on top) for centrality bin 2 at 158 A-GeV. The lines indicate a fit by a single exponential function (solid for fitting range).

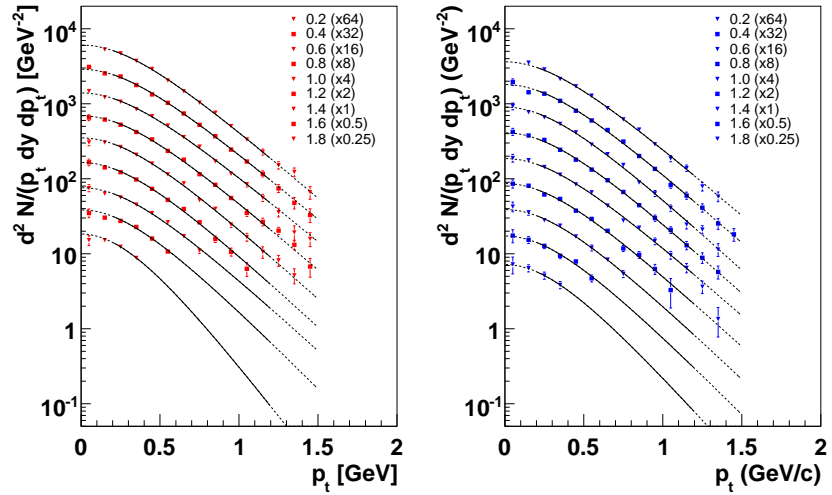


Figure C.18: Transverse momentum spectra  $1/p_T dN/dp_T$  for  $K^+$  (left) and  $K^-$  (right) for different rapidities (mid-rapidity on top) for centrality bin 3 at 158 A-GeV. The lines indicate a fit by a single exponential function (solid for fitting range).

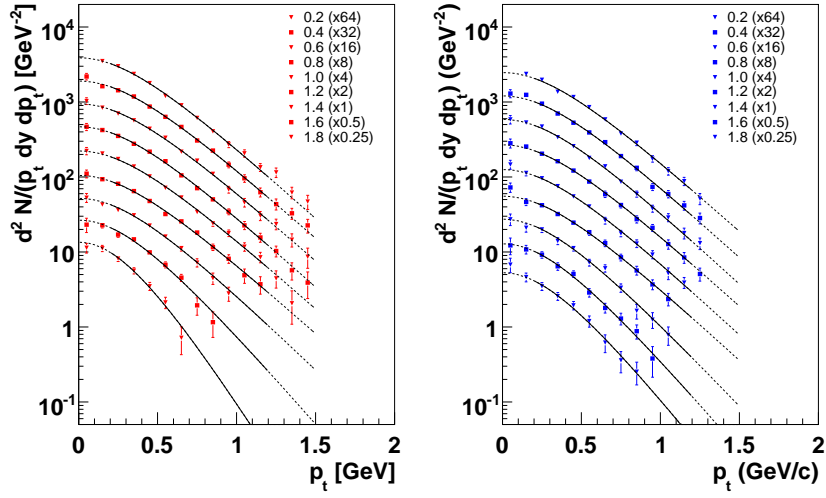


Figure C.19: Transverse momentum spectra  $1/p_T dN/dp_T$  for  $K^+$  (left) and  $K^-$  (right) for different rapidities (mid-rapidity on top) for centrality bin 4 at 158 A·GeV. The lines indicate a fit by a single exponential function (solid for fitting range).

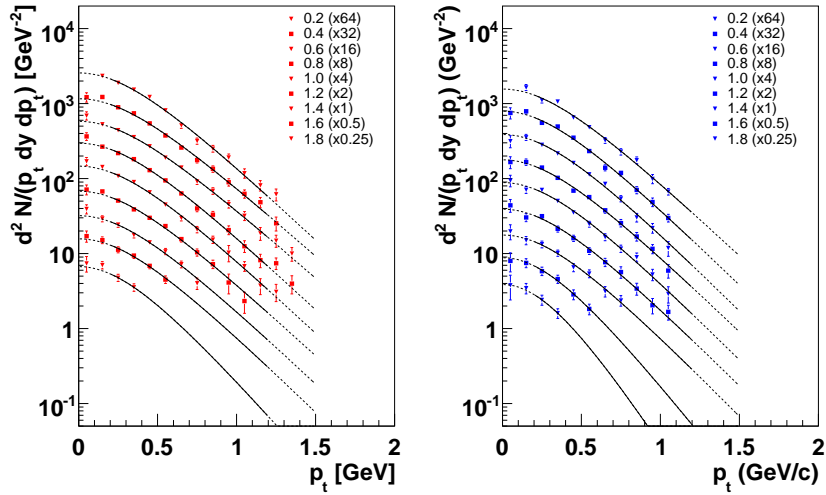


Figure C.20: Transverse momentum spectra  $1/p_T dN/dp_T$  for  $K^+$  (left) and  $K^-$  (right) for different rapidities (mid-rapidity on top) for centrality bin 5 at 158 A·GeV. The lines indicate a fit by a single exponential function (solid for fitting range).

APPENDIX C. ADDITIONAL PLOTS AND NUMERICAL DATA

---

$m_t - m_0$	Bin 1	Bin 2	Bin 3	Bin 4	Bin 5
0.05	$34.92 \pm 2.14$	$26.52 \pm 1.47$	$20.80 \pm 1.10$	$13.50 \pm 0.91$	$10.21 \pm 0.81$
0.15	$28.30 \pm 2.38$	$22.30 \pm 1.70$	$15.01 \pm 1.15$	$8.84 \pm 0.90$	$5.52 \pm 0.71$
0.25	$17.14 \pm 1.76$	$14.93 \pm 1.30$	$9.69 \pm 0.88$	$6.03 \pm 0.71$	$3.67 \pm 0.55$
0.35	$11.39 \pm 1.35$	$7.95 \pm 0.90$	$7.23 \pm 0.70$	$3.42 \pm 0.50$	$2.34 \pm 0.41$
0.45	$7.05 \pm 0.96$	$4.76 \pm 0.64$	$3.58 \pm 0.46$	$2.24 \pm 0.37$	$2.10 \pm 0.37$
0.55	$4.01 \pm 0.69$	$2.93 \pm 0.47$	$1.87 \pm 0.31$	$1.05 \pm 0.24$	$0.89 \pm 0.22$
0.65	$4.43 \pm 0.69$	$2.38 \pm 0.41$	$1.73 \pm 0.28$	$0.65 \pm 0.18$	$0.65 \pm 0.18$
0.75	$1.39 \pm 0.36$	$1.11 \pm 0.27$	$0.93 \pm 0.20$	$0.47 \pm 0.15$	$0.40 \pm 0.14$
0.85	$1.74 \pm 0.39$	$0.64 \pm 0.18$	$0.86 \pm 0.18$	$0.50 \pm 0.14$	$0.36 \pm 0.12$
0.95	$1.05 \pm 0.37$	$0.44 \pm 0.20$	$0.52 \pm 0.17$	$0.20 \pm 0.12$	$0.06 \pm 0.06$

Table C.1:  $K^- 1/m_T dN/dy dm_T$  for different centrality bins at 40 A·GeV.

$m_t - m_0$	Bin 1	Bin 2	Bin 3	Bin 4	Bin 5
0.05	$79.17 \pm 3.75$	$65.66 \pm 1.93$	$50.25 \pm 1.37$	$34.15 \pm 1.11$	$22.66 \pm 0.94$
0.15	$52.66 \pm 2.48$	$43.02 \pm 1.50$	$31.01 \pm 1.02$	$19.75 \pm 0.80$	$13.23 \pm 0.69$
0.25	$32.12 \pm 1.58$	$25.61 \pm 0.99$	$20.29 \pm 0.71$	$14.15 \pm 0.58$	$8.72 \pm 0.48$
0.35	$20.25 \pm 1.08$	$16.55 \pm 0.70$	$11.45 \pm 0.47$	$7.98 \pm 0.38$	$5.33 \pm 0.33$
0.45	$15.20 \pm 0.89$	$11.41 \pm 0.54$	$7.75 \pm 0.36$	$4.94 \pm 0.28$	$2.67 \pm 0.22$
0.55	$8.46 \pm 0.63$	$7.39 \pm 0.42$	$5.16 \pm 0.28$	$3.38 \pm 0.22$	$1.97 \pm 0.18$
0.65	$5.59 \pm 0.49$	$3.83 \pm 0.29$	$3.31 \pm 0.22$	$1.93 \pm 0.16$	$1.32 \pm 0.14$
0.75	$3.43 \pm 0.39$	$3.05 \pm 0.29$	$1.86 \pm 0.18$	$1.14 \pm 0.14$	$0.68 \pm 0.11$
0.85	$1.94 \pm 0.35$	$1.41 \pm 0.24$	$1.42 \pm 0.19$	$0.64 \pm 0.13$	$0.43 \pm 0.11$
0.95	$1.86 \pm 0.42$	$1.66 \pm 0.32$	$0.69 \pm 0.16$	$0.43 \pm 0.13$	$0.27 \pm 0.10$

Table C.2:  $K^- 1/m_T dN/dy dm_T$  for different centrality bins at 158 A·GeV.

APPENDIX C. ADDITIONAL PLOTS AND NUMERICAL DATA

---

$m_t - m_0$	Bin 1	Bin 2	Bin 3	Bin 4	Bin 5
0.05	$91.77 \pm 3.89$	$71.06 \pm 2.60$	$49.04 \pm 1.78$	$32.73 \pm 1.48$	$23.75 \pm 1.25$
0.15	$61.14 \pm 3.81$	$54.30 \pm 2.74$	$34.70 \pm 1.82$	$22.81 \pm 1.51$	$14.02 \pm 1.16$
0.25	$43.60 \pm 3.07$	$32.94 \pm 2.04$	$21.44 \pm 1.35$	$14.20 \pm 1.12$	$7.69 \pm 0.82$
0.35	$25.70 \pm 2.17$	$23.41 \pm 1.59$	$14.66 \pm 1.04$	$10.29 \pm 0.91$	$5.66 \pm 0.65$
0.45	$16.42 \pm 1.63$	$12.99 \pm 1.10$	$9.86 \pm 0.79$	$5.13 \pm 0.59$	$2.71 \pm 0.42$
0.55	$11.38 \pm 1.26$	$8.96 \pm 0.85$	$6.14 \pm 0.59$	$2.75 \pm 0.41$	$2.22 \pm 0.36$
0.65	$8.22 \pm 1.01$	$5.09 \pm 0.60$	$3.22 \pm 0.40$	$2.60 \pm 0.37$	$1.59 \pm 0.29$
0.75	$4.41 \pm 0.70$	$4.40 \pm 0.53$	$2.48 \pm 0.33$	$1.40 \pm 0.26$	$1.03 \pm 0.22$
0.85	$2.61 \pm 0.68$	$1.96 \pm 0.44$	$1.74 \pm 0.34$	$0.95 \pm 0.27$	$0.16 \pm 0.11$
0.95	$1.85 \pm 0.76$	$0.92 \pm 0.41$	$1.06 \pm 0.38$	$0.63 \pm 0.28$	$0.12 \pm 0.12$

Table C.3:  $K^+$   $1/m_T dN/dydm_T$  for different centrality bins at 40 A·GeV.

$m_t - m_0$	Bin 1	Bin 2	Bin 3	Bin 4	Bin 5
0.05	$125.64 \pm 2.88$	$103.37 \pm 2.08$	$76.26 \pm 1.43$	$55.00 \pm 1.20$	$35.76 \pm 0.83$
0.15	$89.09 \pm 2.42$	$71.04 \pm 1.71$	$49.05 \pm 1.14$	$33.44 \pm 0.93$	$21.68 \pm 0.68$
0.25	$56.06 \pm 1.65$	$45.92 \pm 1.19$	$32.80 \pm 0.81$	$21.16 \pm 0.64$	$13.45 \pm 0.48$
0.35	$37.14 \pm 1.23$	$28.29 \pm 0.83$	$21.16 \pm 0.58$	$13.51 \pm 0.46$	$8.80 \pm 0.36$
0.45	$22.91 \pm 0.93$	$19.23 \pm 0.64$	$13.72 \pm 0.44$	$8.36 \pm 0.33$	$5.07 \pm 0.26$
0.55	$14.42 \pm 0.71$	$12.11 \pm 0.49$	$8.28 \pm 0.32$	$5.31 \pm 0.26$	$3.14 \pm 0.20$
0.65	$9.60 \pm 0.58$	$7.28 \pm 0.38$	$5.24 \pm 0.26$	$3.31 \pm 0.20$	$1.89 \pm 0.17$
0.75	$6.40 \pm 0.54$	$5.03 \pm 0.35$	$3.41 \pm 0.23$	$2.10 \pm 0.18$	$1.47 \pm 0.17$
0.85	$4.07 \pm 0.53$	$3.10 \pm 0.33$	$2.25 \pm 0.22$	$1.48 \pm 0.18$	$0.89 \pm 0.16$
0.95	$2.29 \pm 0.49$	$2.01 \pm 0.31$	$1.46 \pm 0.21$	$0.80 \pm 0.15$	$0.58 \pm 0.16$

Table C.4:  $K^+$   $1/m_T dN/dydm_T$  for different centrality bins at 158 A·GeV.



APPENDIX C. ADDITIONAL PLOTS AND NUMERICAL DATA

$m_t - m_0$	Bin 1	Bin 2	Bin 3
0.025	$2.6e+03 \pm 3.2e+01$	$2.0e+03 \pm 2.2e+01$	$1.5e+03 \pm 1.5e+01$
0.075	$1.5e+03 \pm 2.1e+01$	$1.2e+03 \pm 1.4e+01$	$8.8e+02 \pm 9.8e+00$
0.125	$9.1e+02 \pm 1.5e+01$	$7.4e+02 \pm 1.0e+01$	$5.5e+02 \pm 7.1e+00$
0.175	$6.7e+02 \pm 1.1e+01$	$5.4e+02 \pm 7.7e+00$	$3.9e+02 \pm 5.4e+00$
0.225	$5.1e+02 \pm 8.9e+00$	$4.1e+02 \pm 6.0e+00$	$2.9e+02 \pm 4.1e+00$
0.275	$3.8e+02 \pm 7.1e+00$	$3.0e+02 \pm 4.8e+00$	$2.1e+02 \pm 3.3e+00$
0.325	$2.7e+02 \pm 5.6e+00$	$2.2e+02 \pm 3.8e+00$	$1.5e+02 \pm 2.6e+00$
0.375	$2.1e+02 \pm 4.6e+00$	$1.6e+02 \pm 3.1e+00$	$1.2e+02 \pm 2.2e+00$
0.425	$1.5e+02 \pm 3.9e+00$	$1.2e+02 \pm 2.6e+00$	$8.7e+01 \pm 1.8e+00$
0.475	$1.2e+02 \pm 5.0e+00$	$9.4e+01 \pm 2.2e+00$	$6.9e+01 \pm 1.5e+00$
0.525	$9.2e+01 \pm 2.7e+00$	$7.0e+01 \pm 1.8e+00$	$5.0e+01 \pm 2.0e+00$
0.575	$6.7e+01 \pm 5.0e+00$	$5.2e+01 \pm 1.6e+00$	$3.9e+01 \pm 1.1e+00$
0.625	$5.1e+01 \pm 4.0e+00$	$4.0e+01 \pm 1.3e+00$	$2.9e+01 \pm 9.3e-01$
0.675	$4.1e+01 \pm 5.0e+00$	$3.1e+01 \pm 1.1e+00$	$2.5e+01 \pm 8.1e-01$
0.725	$3.0e+01 \pm 5.0e+00$	$2.4e+01 \pm 4.0e+00$	$1.8e+01 \pm 2.0e+00$
0.775	$2.5e+01 \pm 1.3e+00$	$2.0e+01 \pm 3.0e+00$	$1.4e+01 \pm 5.8e-01$
0.825	$1.9e+01 \pm 1.1e+00$	$1.5e+01 \pm 7.4e-01$	$1.0e+01 \pm 5.0e-01$
0.875	$1.5e+01 \pm 9.6e-01$	$1.1e+01 \pm 6.3e-01$	$8.0e+00 \pm 4.3e-01$
0.925		$9.3e+00 \pm 2.0e+00$	
0.975	$1.0e+01 \pm 7.3e-01$	$7.6e+00 \pm 4.8e-01$	$5.6e+00 \pm 3.4e-01$
$m_t - m_0$	Bin 4	Bin 5	
0.025	$9.5e+02 \pm 1.3e+01$	$6.3e+02 \pm 1.0e+01$	
0.075	$5.8e+02 \pm 8.2e+00$	$3.8e+02 \pm 6.6e+00$	
0.125	$3.4e+02 \pm 5.8e+00$	$2.3e+02 \pm 4.7e+00$	
0.175	$2.5e+02 \pm 4.4e+00$	$1.7e+02 \pm 3.6e+00$	
0.225	$1.9e+02 \pm 3.4e+00$	$1.2e+02 \pm 2.8e+00$	
0.275	$1.4e+02 \pm 2.7e+00$	$9.1e+01 \pm 2.2e+00$	
0.325	$1.0e+02 \pm 2.2e+00$	$6.9e+01 \pm 1.8e+00$	
0.375	$7.4e+01 \pm 1.8e+00$	$5.1e+01 \pm 1.5e+00$	
0.425	$5.7e+01 \pm 1.5e+00$	$3.6e+01 \pm 1.2e+00$	
0.475	$4.3e+01 \pm 1.2e+00$	$2.8e+01 \pm 9.9e-01$	
0.525	$3.3e+01 \pm 1.1e+00$	$2.1e+01 \pm 8.4e-01$	
0.575	$2.4e+01 \pm 2.0e+00$	$1.5e+01 \pm 1.0e+00$	
0.625	$1.8e+01 \pm 2.0e+00$	$1.1e+01 \pm 1.0e+00$	
0.675	$1.4e+01 \pm 2.0e+00$	$9.8e+00 \pm 1.0e+00$	
0.725	$1.1e+01 \pm 5.4e-01$	$6.8e+00 \pm 1.0e+00$	
0.775	$9.3e+00 \pm 4.9e-01$	$5.8e+00 \pm 3.9e-01$	
0.825	$7.1e+00 \pm 4.2e-01$	$3.9e+00 \pm 3.2e-01$	
0.875	$5.2e+00 \pm 1.0e+00$	$3.1e+00 \pm 2.8e-01$	
0.925	$3.8e+00 \pm 3.0e-01$	$2.7e+00 \pm 2.5e-01$	
0.975	$3.6e+00 \pm 2.7e-01$	$2.0e+00 \pm 2.0e-01$	

Table C.5:  $\pi^- 1/m_T dN/dy dm_T$  for different centrality bins at 40 A·GeV.

APPENDIX C. ADDITIONAL PLOTS AND NUMERICAL DATA

$m_t - m_0$	Bin 1	Bin 2	Bin 3
0.025	6.11e+03 ± 2.87e+01	3.39e+03 ± 2.15e+01	2.03e+03 ± 1.49e+01
0.075	2.34e+03 ± 1.96e+01	1.66e+03 ± 1.46e+01	1.16e+03 ± 1.02e+01
0.125	1.41e+03 ± 1.45e+01	1.08e+03 ± 1.09e+01	7.82e+02 ± 7.52e+00
0.175	9.87e+02 ± 1.12e+01	7.75e+02 ± 8.40e+00	5.44e+02 ± 5.75e+00
0.225	6.98e+02 ± 8.67e+00	5.47e+02 ± 6.51e+00	3.92e+02 ± 4.54e+00
0.275	5.32e+02 ± 6.97e+00	4.03e+02 ± 5.23e+00	2.86e+02 ± 3.60e+00
0.325	3.96e+02 ± 5.75e+00	3.04e+02 ± 4.30e+00	2.14e+02 ± 2.97e+00
0.375	2.77e+02 ± 4.87e+00	2.25e+02 ± 3.61e+00	1.58e+02 ± 2.46e+00
0.425	2.26e+02 ± 4.19e+00	1.72e+02 ± 3.03e+00	1.20e+02 ± 2.05e+00
0.475	1.81e+02 ± 3.56e+00	1.40e+02 ± 2.61e+00	9.59e+01 ± 1.75e+00
0.525	1.31e+02 ± 3.04e+00	1.06e+02 ± 2.23e+00	7.18e+01 ± 1.48e+00
0.575	1.02e+02 ± 2.59e+00	8.04e+01 ± 1.88e+00	5.55e+01 ± 1.25e+00
0.625	8.06e+01 ± 2.26e+00	6.22e+01 ± 1.61e+00	4.25e+01 ± 1.08e+00
0.675	6.54e+01 ± 1.94e+00	5.24e+01 ± 1.42e+00	3.46e+01 ± 2.00e+00
0.725	5.11e+01 ± 1.68e+00	3.96e+01 ± 3.00e+00	2.71e+01 ± 8.07e-01
0.775	3.81e+01 ± 3.00e+00	3.05e+01 ± 1.04e+00	2.18e+01 ± 7.00e-01
0.825	2.98e+01 ± 1.22e+00	2.42e+01 ± 9.03e-01	1.63e+01 ± 5.91e-01
0.875	2.26e+01 ± 3.00e+00	1.87e+01 ± 7.74e-01	1.32e+01 ± 2.00e+00
0.925	1.84e+01 ± 9.12e-01	1.56e+01 ± 6.77e-01	1.14e+01 ± 4.55e-01
0.975	1.51e+01 ± 3.00e+00	1.32e+01 ± 6.30e-01	7.98e+00 ± 3.93e-01
$m_t - m_0$	Bin 4	Bin 5	
0.025	1.28e+03 ± 1.28e+01	8.42e+02 ± 1.05e+01	
0.075	7.68e+02 ± 8.68e+00	4.90e+02 ± 6.93e+00	
0.125	5.17e+02 ± 6.36e+00	3.43e+02 ± 5.20e+00	
0.175	3.57e+02 ± 4.84e+00	2.39e+02 ± 3.97e+00	
0.225	2.62e+02 ± 3.89e+00	1.69e+02 ± 3.12e+00	
0.275	1.92e+02 ± 3.09e+00	1.25e+02 ± 2.50e+00	
0.325	1.38e+02 ± 2.49e+00	8.80e+01 ± 2.00e+00	
0.375	1.02e+02 ± 2.05e+00	6.70e+01 ± 1.68e+00	
0.425	7.87e+01 ± 1.72e+00	5.12e+01 ± 1.39e+00	
0.475	6.40e+01 ± 1.48e+00	3.99e+01 ± 1.17e+00	
0.525	4.45e+01 ± 1.21e+00	3.00e+01 ± 9.96e-01	
0.575	3.56e+01 ± 1.05e+00	2.19e+01 ± 8.21e-01	
0.625	2.74e+01 ± 8.99e-01	1.77e+01 ± 7.20e-01	
0.675	2.27e+01 ± 7.77e-01	1.45e+01 ± 6.22e-01	
0.725	1.72e+01 ± 6.58e-01	1.05e+01 ± 5.22e-01	
0.775	1.33e+01 ± 1.00e+00	8.38e+00 ± 4.53e-01	
0.825	1.01e+01 ± 4.89e-01	6.50e+00 ± 3.95e-01	
0.875	8.62e+00 ± 4.40e-01	5.07e+00 ± 3.35e-01	
0.925	7.56e+00 ± 3.89e-01	4.06e+00 ± 2.86e-01	
0.975	5.46e+00 ± 3.32e-01	3.54e+00 ± 2.68e-01	

Table C.6:  $\pi^- 1/m_T dN/dydm_T$  for different centrality bins at 158 A·GeV.

## Rapidity spectra

y bin	Bin 1	Bin 2	Bin 3	Bin 4	Bin 5
0.0-0.2 (TOF)	8.50±0.33	6.21±0.22	4.70±0.16	2.68±0.12	1.95±0.10
0.2-0.4					
0.4-0.6					
0.6-0.8	7.12±0.23	5.37±0.16	3.90±0.11	2.49±0.10	1.62±0.08
0.8-1.0	6.30±0.22	4.67±0.14	3.25±0.09	2.12±0.09	1.35±0.07
1.0-1.2	4.80±0.19	3.76±0.13	2.58±0.09	1.65±0.07	1.07±0.07
1.2-1.4	3.74±0.17	2.86±0.11	1.99±0.08	1.26±0.07	0.72±0.06
1.4-1.6	2.47±0.16	2.02±0.12	1.36±0.08	0.85±0.06	0.53±0.07
1.6-1.8	1.57±0.25	1.26±0.12	0.81±0.08	0.48±0.07	0.36±0.10

Table C.7:  $K^-$   $dN/dy$  for different centrality bins at 40 A·GeV.

y bin	Bin 1	Bin 2	Bin 3	Bin 4	Bin 5
-0.1-0.1 (TOF)	16.30±0.80	13.20±0.40	9.60±0.30	6.30±0.20	4.10±0.20
0.1-0.3	17.30±0.34	13.55±0.25	9.48±0.16	6.21±0.13	3.74±0.11
0.3-0.5	16.74±0.32	13.16±0.23	9.02±0.15	6.00±0.13	3.56±0.10
0.5-0.7	16.24±0.32	12.64±0.22	8.74±0.15	5.64±0.12	3.36±0.10
0.7-0.9	15.26±0.33	11.85±0.23	8.14±0.14	5.27±0.12	3.22±0.10
0.9-1.1	13.74±0.36	10.85±0.24	7.49±0.15	4.78±0.13	3.07±0.10
1.1-1.3	12.16±0.38	9.70±0.25	6.66±0.18	4.27±0.13	2.73±0.11
1.3-1.5	10.11±0.39	8.10±0.28	5.72±0.22	3.51±0.14	2.39±0.14
1.5-1.7	8.00±0.40	6.46±0.28	4.77±0.39	2.94±0.14	1.82±0.17
1.7-1.9	5.90±0.43	4.93±0.27	3.39±0.88	2.22±0.13	1.20±0.24

Table C.8:  $K^-$   $dN/dy$  for different centrality bins at 158 A·GeV.

APPENDIX C. ADDITIONAL PLOTS AND NUMERICAL DATA

y bin	Bin 1	Bin 2	Bin 3	Bin 4	Bin 5
0.0-0.2 (TOF)	20.10±0.60	16.20±0.40	10.90±0.30	6.90±0.20	4.20±0.20
0.2-0.4					
0.4-0.6					
0.6-0.8	19.88±0.54	15.28±0.41	11.18±0.39	7.02±0.21	4.22±0.17
0.8-1.0	17.43±0.47	13.79±0.78	9.76±0.24	6.28±0.18	3.75±0.14
1.0-1.2	15.23±0.43	12.17±0.33	8.77±0.21	5.49±0.17	3.46±0.14
1.2-1.4	11.92±0.39	10.10±0.31	7.30±0.21	4.69±0.17	2.84±0.14
1.4-1.6	9.65±0.40	7.48±0.30	5.61±0.18	3.64±0.16	2.25±0.13
1.6-1.8	6.39±0.31	5.82±0.28	3.90±0.18	2.61±0.15	1.75±0.13
1.8-2.0	4.01±0.30	4.08±0.29	2.57±0.18	1.87±0.15	

Table C.9:  $K^+$   $dN/dy$  for different centrality bins at 40 A·GeV.

y bin	Bin 1	Bin 2	Bin 3	Bin 4	Bin 5
-0.1-0.1 (TOF)	27.50±0.70	22.10±0.50	15.80±0.40	10.50±0.30	6.70±0.20
0.1-0.3	29.19±0.51	23.34±0.35	15.93±0.23	9.71±0.18	6.07±0.15
0.3-0.5	28.60±0.51	22.76±0.33	15.48±0.21	9.68±0.17	5.96±0.14
0.5-0.7	28.10±0.48	21.94±0.33	15.02±0.22	9.59±0.18	5.96±0.14
0.7-0.9	27.03±0.51	21.15±0.36	14.44±0.22	9.23±0.17	5.68±0.14
0.9-1.1	25.17±0.59	20.04±0.39	13.76±0.23	8.93±0.19	5.53±0.15
1.1-1.3	23.79±0.67	18.83±0.44	12.52±0.26	8.29±0.21	5.20±0.17
1.3-1.5	20.62±0.90	16.36±0.51	11.84±0.37	7.09±0.34	4.73±0.22
1.5-1.7	16.17±0.73	12.33±0.52	10.90±0.67	5.91±0.24	4.39±0.36
1.7-1.9	10.24±0.75	9.00±0.47		4.11±0.24	

Table C.10:  $K^+$   $dN/dy$  for different centrality bins at 158 A·GeV.

APPENDIX C. ADDITIONAL PLOTS AND NUMERICAL DATA

y bin	Bin 1	Bin 2	Bin 3	Bin 4	Bin 5
0.0-0.2	118.14±0.81	93.90±0.65	67.94±0.52	43.70±0.41	28.92±0.31
0.2-0.4	118.32±0.82	93.72±0.66	67.56±0.52	43.62±0.40	29.31±0.37
0.4-0.6	111.57±0.78	88.81±0.60	64.24±0.48	42.07±0.38	27.99±0.34
0.6-0.8	100.87±0.73	80.68±0.58	58.02±0.44	39.38±0.36	26.19±0.32
0.8-1.0	90.32±0.70	72.70±0.51	53.70±0.37	35.84±0.33	24.74±0.30
1.0-1.2	79.55±0.71	65.56±0.55	48.54±0.42	32.64±0.36	22.89±0.31
1.2-1.4	66.78±0.61	55.57±0.46	42.07±0.36	29.00±0.33	20.06±0.25
1.4-1.6	52.94±0.58	44.54±0.41	34.26±0.32	24.21±0.31	17.02±0.28
1.6-1.8	42.22±0.53	36.07±0.33	27.92±0.26	19.81±0.25	14.25±0.29
1.8-2.0	30.36±0.55	26.68±0.38	21.04±0.26	15.49±0.34	11.16±0.29
2.0-2.2	21.85±0.39	19.97±0.36	16.43±0.25	12.72±0.26	9.35±0.25
2.2-2.4	14.78±0.44	13.72±0.32	11.77±0.22	9.25±0.18	7.07±0.15
2.4-2.6	9.24±0.32	8.69±0.32	7.54±0.25	5.98±0.25	4.49±0.18

Table C.11:  $\pi^-$   $dN/dy$  for different centrality bins at 40 A·GeV.

y bin	Bin 1	Bin 2	Bin 3	Bin 4	Bin 5
0.0-0.2	160.62±1.00	122.22±0.90	86.37±0.72	57.36±0.57	37.43±0.42
0.2-0.4	156.99±0.97	120.73±0.83	86.08±0.66	56.97±0.54	36.98±0.39
0.4-0.6	153.21±0.91	117.61±0.77	83.38±0.62	55.09±0.48	36.12±0.38
0.6-0.8	145.68±0.79	113.03±0.80	80.39±0.64	52.75±0.49	34.34±0.37
0.8-1.0	139.64±0.91	108.33±0.75	76.87±0.61	50.95±0.47	33.14±0.36
1.0-1.2	129.13±0.83	102.83±0.71	72.19±0.56	47.61±0.45	31.10±0.35
1.2-1.4	118.45±0.76	93.77±0.64	67.10±0.50	44.42±0.40	29.38±0.30
1.4-1.6	104.48±0.68	84.39±0.56	60.37±0.42	40.35±0.35	26.84±0.41
1.6-1.8	92.29±0.64	73.79±0.52	54.55±0.40	36.85±0.34	24.39±0.29
1.8-2.0	76.94±0.59	62.65±0.47	46.57±0.37	31.76±0.29	21.37±0.28
2.0-2.2	62.28±0.68	52.28±0.44	39.30±0.33	27.47±0.38	18.61±0.31
2.2-2.4	48.95±0.49	42.25±0.44	31.86±0.35	22.47±0.29	15.91±0.23
2.4-2.6	36.41±0.46	31.42±0.39	24.39±0.31	17.88±0.28	12.64±0.28
2.6-2.8	26.08±0.70	23.89±0.84	19.02±0.66	14.23±0.62	10.21±0.43

Table C.12:  $\pi^-$   $dN/dy$  for different centrality bins at 158 A·GeV.

# Bibliography

- [Abe08] B. I. Abelev *et al.* [STAR Collaboration], Phys. Rev. C **79** (2009) 034909 [arXiv:0808.2041 [nucl-ex]].
- [Adl01] C. Adler *et al.* [STAR Collaboration], Phys. Rev. Lett. **87** (2001) 182301 [arXiv:nucl-ex/0107003].
- [Adr03] S. S. Adler *et al.* [PHENIX Collaboration], Phys. Rev. C **69** (2004) 034909 [arXiv:nucl-ex/0307022].
- [Afa99] S. V. Afanasev *et al.* [NA49 Collaboration], Nucl. Instrum. Meth. A **430** (1999) 210.
- [Afa02] S. V. Afanasev *et al.* [NA49 Collaboration], Nucl. Phys. A **698** (2002) 104.
- [Ahl99] L. Ahle *et al.* [E-802 Collaboration and E-866 Collaboration], Phys. Rev. C **60** (1999) 044904 [arXiv:nucl-ex/9903009].
- [Aic08] J. Aichelin and K. Werner, arXiv:0810.4465 [nucl-th].
- [Aic09] J. Aichelin, private communication.
- [Afa02] S. V. Afanasiev *et al.* [The NA49 Collaboration], Phys. Rev. C **66** (2002) 054902 [arXiv:nucl-ex/0205002].
- [Alb97] T. Alber *et al.* [NA35 Collaboration], Eur. Phys. J. C **2** (1998) 643 [arXiv:hep-ex/9711001].
- [Alt03] C. Alt *et al.* [NA49 Collaboration], Phys. Rev. C **68** (2003) 034903 [arXiv:nucl-ex/0303001].
- [Alt04b] C. Alt *et al.* [NA49 Collaboration], Phys. Rev. Lett. **94**, 052301 (2005) [arXiv:nucl-ex/0406031v2].
- [Alt07] C. Alt *et al.* [NA49 Collaboration], Phys. Rev. C **77** (2008) 024903 [arXiv:0710.0118 [nucl-ex]].
- [Ani77] V. V. Anisovich, Yu. M. Shabelski and V. M. Shekhter, Nucl. Phys. B **133** (1978) 477.
- [Ant09] T. Anticic *et al.* [NA49 Collaboration], arXiv:0906.0469 [nucl-ex].
- [Amb86] K. Ambrus, Dissertation, Heidelberg (1986).

- [Bac99] J. Bachler *et al.* [NA49 Collaboration], Nucl. Phys. A **661** (1999) 45.
- [Bai00] R. Baier, D. Schiff and B. G. Zakharov, Ann. Rev. Nucl. Part. Sci. **50**, 37 (2000) [arXiv:hep-ph/0002198].
- [Bas96] S. A. Bass *et al.*, *Prepared for International Conference on Nuclear Physics at the Turn of Millennium: Structure of Vacuum and Elementary Matter, Wilderness / George, South Africa, 10-16 Mar 1996*
- [Bec97a] F. Becattini, M. Gazdzicki and J. Sollfrank, Eur. Phys. J. C **5** (1998) 143 [arXiv:hep-ph/9710529].
- [Bec97b] F. Becattini and U. W. Heinz, Z. Phys. C **76** (1997) 269 [Erratum-ibid. C **76** (1997) 578] [arXiv:hep-ph/9702274].
- [Bec00] F. Becattini, J. Cleymans, A. Keranen, E. Suhonen and K. Redlich, Phys. Rev. C **64**, 024901 (2001) [arXiv:hep-ph/0002267].
- [Bec05] F. Becattini, J. Manninen and M. Gazdzicki, Phys. Rev. C **73** (2006) 044905 [arXiv:hep-ph/0511092].
- [Bec08a] F. Becattini and J. Manninen, J. Phys. G **35** (2008) 104013 [arXiv:0805.0098 [nucl-th]].
- [Bec08b] F. Becattini and J. Manninen, Phys. Lett. B **673** (2009) 19 [arXiv:0811.3766 [nucl-th]].
- [Ber89] V. Bernard and U. G. Meissner, Phys. Lett. B **227** (1989) 465.
- [Bet30] H. A. Bethe, Annalen der Physik **5** (1930) 325.
- [Bia76] A. Białas, M. Bleszynski and W. Czyz, Nucl. Phys. B **111** (1976) 461.
- [Bia77] A. Białas, W. Czyz and W. Furmanski, Acta Phys. Polon. B **8** (1977) 585.
- [Bjo82] J. D. Bjorken, Phys. Rev. D **27** (1983) 140.
- [Blo33] F. Bloch, Z. Physik **81** (1933) 363.
- [Blu89] W. Blum *et. al* [ALEPH collaboration], The ALEPH Handbook, ALEPH 89-77 CERN (1989).
- [Boc95] R. K. Bock *et al.*, Data Analysis Techniques for High-Energy Physics Experiments, Cambridge University Press (1995).
- [Boi08] Bożena Boimska and Helena Białkowska, private communication.
- [Brm01] R. Bramm, Diploma thesis, Johann-Wolfgang-Goethe-Universität, Frankfurt am Main, 2001.
- [Brt09] E. Bratkovskaya, private communication.
- [Bra99] P. Braun-Munzinger, I. Heppe and J. Stachel, Phys. Lett. B **465** (1999) 15 [arXiv:nucl-th/9903010].
- [Bra01] P. Braun-Munzinger, J. Cleymans, H. Oeschler and K. Redlich, Nucl. Phys. A **697** (2002) 902 [arXiv:hep-ph/0106066].

- 
- [Bra03] P. Braun-Munzinger, J. Stachel and C. Wetterich, Phys. Lett. B **596** (2004) 61 [arXiv:nucl-th/0311005].
- [Car73] P. Carruthers and M. Doung-van, Phys. Rev. D **8** (1973) 859.
- [Cas99] W. Cassing and E. L. Bratkovskaya, Phys. Rept. **308** (1999) 65.
- [Ceb09] D. Cebra [STAR Collaboration], arXiv:0903.4702 [nucl-ex].
- [Cer91] CERN,  
[http://multimedia-gallery.web.cern.ch/multimedia-gallery/PhotoGallery\\_Detailed.aspx?searchTerm=internalnote:'Views\\*'&page=5&order=22](http://multimedia-gallery.web.cern.ch/multimedia-gallery/PhotoGallery_Detailed.aspx?searchTerm=internalnote:'Views*'&page=5&order=22)
- [Cer05] CERN,  
<http://www.cern.ch>
- [Cho74] A. Chodos, R. L. Jaffe, K. Johnson, C. B. Thorn and V. F. Weisskopf, Phys. Rev. D **9** (1974) 3471.
- [Cle98] J. Cleymans, H. Oeschler and K. Redlich, Phys. Rev. C **59** (1999) 1663 [arXiv:nucl-th/9809027].
- [Cle05] J. Cleymans, H. Oeschler, K. Redlich and S. Wheaton, [arXiv:hep-ph/0504065v1]
- [Coo00] G. E. Cooper, Ph.D. thesis, Lawrence Berkely National Laboratory, 2000.
- [Din05] P. Dinkelaker [NA49 Collaboration], J. Phys. G **31** (2005) S1131.
- [Ehe95] W. Ehehalt and W. Cassing, arXiv:hep-ph/9507274.
- [Fer40] E. Fermi, Phys. Rev. **57** (1940) 485.
- [Fis02] H. G. Fischer [NA49 Collaboration], Nucl. Phys. A **715** (2003) 118 [arXiv:hep-ex/0209043].
- [For04] A. Forster *et al.* [KaoS Collaboration], J. Phys. G **31** (2005) S693 [arXiv:nucl-ex/0411045].
- [Gab98] F. Gabler, Dissertation, Johann-Wolfgang-Goethe-Universität, Frankfurt am Main, 1998.
- [Gaz98] M. Gazdzicki and M. I. Gorenstein, Acta Phys. Polon. B **30** (1999) 2705 [arXiv:hep-ph/9803462].
- [Gaz04] M. Gazdzicki *et al.* [NA49 Collaboration], J. Phys. G **30** (2004) S701 [arXiv:nucl-ex/0403023].
- [GEA93] GEANT, Detector Description and Simulation Tool, CERN Program Library Long Writeup W5013 (1993).
- [Ger86] H. Von Gersdorff, L. D. McLerran, M. Kataja and P. V. Ruuskanen, Phys. Rev. D **34** (1986) 794.
-



- [Gla70] R. J. Glauber and G. Matthiae, Nucl. Phys. B **21** (1970) 135.
- [Glu63] R. L. Gluckstern, Nucl. Instrum. Meth. **24** (1963) 381.
- [Ham00] S. Hamieh, K. Redlich and A. Tounsi, Phys. Lett. B **486** (2000) 61 [arXiv:hep-ph/0006024].
- [Han03] M. Hanson  
<http://www.physics.uc.edu/~hanson/ASTRO/LECTURENOTES/W03/Lec23/Page6.html>
- [Hei00a] U. W. Heinz, Nucl. Phys. A **685** (2001) 414 [arXiv:hep-ph/0009170].
- [Hei00b] U. W. Heinz and M. Jacob, arXiv:nucl-th/0002042.
- [Hoh03] C. Höhne, Dissertation, Philipps-Universität, Marburg, 2003.
- [Hoh05] C. Höhne, F. Puhlhofer and R. Stock, Phys. Lett. B **640** (2006) 96 [arXiv:hep-ph/0507276].
- [Iwa96] Y. Iwasaki, K. Kanaya, S. Kaya, S. Sakai and T. Yoshie, Phys. Rev. D **54** (1996) 7010 [arXiv:hep-lat/9605030].
- [Jaf76] R. L. Jaffe, Phys. Rev. D **15**, 281 (1977).
- [Kaj81] K. Kajantie and H. I. Miettinen, Z. Phys. C **9** (1981) 341.
- [Kan02] K. Kanaya, Nucl. Phys. A **715** (2003) 233 [arXiv:hep-ph/0209116].
- [Kar03] F. Karsch, C. R. Allton, S. Ejiri, S. J. Hands, O. Kaczmarek, E. Laermann and C. Schmidt, Nucl. Phys. Proc. Suppl. **129** (2004) 614 [arXiv:hep-lat/0309116].
- [Kha94] D. Kharzeev and H. Satz, Phys. Lett. B **334** (1994) 155 [arXiv:hep-ph/9405414].
- [Kli05] M. Kliemant, Diploma thesis, Johann-Wolfgang-Goethe-Universität, Frankfurt am Main, 2005.
- [Kol06] V. Kolesnikov, Private communication, 2006.
- [Kog01] T. Kollegger, Diploma thesis, Johann-Wolfgang-Goethe-Universität, Frankfurt am Main, 2001.
- [Kra04] I. Kraus, Dissertation, Johann-Wolfgang-Goethe-Universität, Frankfurt am Main, 2004.
- [Lan44] L. Landau, J. Phys. (USSR) **8** (1944) 201.
- [Lan53] L. D. Landau, Izv. Akad. Nauk Ser. Fiz. **17** (1953) 51.
- [Lan69] L.D. Landau and E.M. Lifshitz, *Statistical Physics*, Pergamom Press, 1969.
- [Lag04] S. Lange, private communication

- 
- [Las06] A. Laszlo, Calculating mean values of collision parameters as function of centrality, Internal Report (2006).
- [Lee03] M. van Leeuwen, Dissertation, NIKHEF, Amsterdam (2003).
- [Lun04] B. Lungwitz, Diploma thesis, Johann-Wolfgang-Goethe-Universität, Frankfurt am Main (2004).
- [Lun08] B. Lungwitz, Dissertation, Johann-Wolfgang-Goethe-Universität, Frankfurt am Main (2008).
- [Mat86] T. Matsui and H. Satz, Phys. Lett. B **178** (1986) 416.
- [Mit06] M. K. Mitrovski *et al.* [NA49 Collaboration], J. Phys. G **32** (2006) S43 [arXiv:nucl-ex/0606004].
- [Mit07] M. Mitrovski, Dissertation, Johann-Wolfgang-Goethe-Universität, Frankfurt am Main (2007).
- [Mit09] M. Mitrovski, private communication.
- [Moc97] A. Mock, Dissertation, Max-Planck-Institut für Physik, München (1997).
- [NA49] NA49,  
<http://na49info.web.cern.ch/na49info/>
- [Pet06] P. Petreczky, Nucl. Phys. A **785** (2007) 10 [arXiv:hep-lat/0609040].
- [Pi92] H. Pi, Comput. Phys. Commun. **71** (1992) 173.
- [Pis81] R. D. Pisarski, Phys. Lett. B **110** (1982) 155.
- [Raf80] J. Rafelski and M. Danos, Phys. Lett. B **97** (1980) 279.
- [Raf82a] J. Rafelski, Phys. Rept. **88** (1982) 331.
- [Raf82b] J. Rafelski and B. Muller, Phys. Rev. Lett. **48** (1982) 1066 [Erratum-ibid. **56** (1986) 2334].
- [Rol00] C. Roland, Dissertation, Johann-Wolfgang-Goethe-Universität, Frankfurt am Main, 2000.
- [Sam00] T. Sammer, Dissertation, Max-Planck-Institut für Physik, München (2000).
- [Shu78] E. V. Shuryak, Phys. Lett. B **78** (1978) 150 [Sov. J. Nucl. Phys. **28** (1978) YAFIA,28,796-808.1978] 408.1978 YAFIA,28,796].
- [Sik99] F. Sikler, NA49 notes  
<http://na49info.web.cern.ch/na49info/na49/Physics/dEdx/notes/dedx.ps.gz>
- [Sik00] F. Sikler, NA49 Collaboration Meeting, CERN, Oktober 2000 und NA49 Collaboration Meeting, GSI, Dezember 2000.
- [Ste71] R. M. Sternheimer, R. F. Peierls, Phys. Rev. **B3** (1971), 3681.
-

- [Sto94] R. Stock, *Prepared for NATO Advanced Study Workshop on Hot Hadronic Matter: Theory and Experiment, Divonne-les-Bains, France, 27 Jun - 1 Jul 1994*
- [Tim08] A. R. Timmins [STAR Collaboration], arXiv:0810.0017 [nucl-ex].
- [Tou02] A. Tounsi and K. Redlich, J. Phys. G **28** (2002) 2095.
- [Toy99] M. Toy, Ph.D. thesis, University of California, Los Angeles, 1999.
- [Utv09] M. Utvic, Diploma thesis, Johann-Wolfgang-Goethe-Universität, Frankfurt am Main (2009).
- [Ver00] G. Veres, Dissertation (2000).
- [Vol07] S. A. Voloshin [STAR Collaboration], J. Phys. G **34** (2007) S883 [arXiv:nucl-ex/0701038].
- [Wan99] F. Wang, H. Liu, H. Sorge, N. Xu and J. Yang, Phys. Rev. C **61** (2000) 064904 [arXiv:nucl-th/9909001].
- [Wen95] S. Wenig, NA49 note, 1995.
- [Wer93] K. Werner, Phys. Rept. **232** (1993) 87.
- [Won94] C.-Y. Wong, Introduction to high-energy heavy-ion collisions, World Scientific, 1994.
- [Wro85] A. Wroblewski, Acta Phys. Polon. B **16** (1985) 379.
- [Zyb95] R. Zybert and P. Buncic, *Prepared for International Conference on Computing in High-energy Physics (CHEP 95), Rio de Janeiro, Brazil, 18-22 Sep 1995*



# Curriculum Vitae



Peter Dinkelaker  
born September 21, 1976 in Frankfurt am Main

## Education

08/1993-06/1996 University-entrance diploma (Abitur) at Goethe-Gymnasium in Frankfurt am Main

10/1996-10/1997 National service at youth center Jugendhaus Frankfurter Berg

10/1997-05/2002 University diploma in physics at Goethe University Frankfurt am Main  
Main Topic of diploma thesis:  
"Phi-Produktion in zentralen Blei-Blei-Kollisionen bei 158 A·GeV"  
(Gutachter: Dr. Dr. h.c. Reinhard Stock)

## Career

Since 10/2000 Member of the NA49 collaboration at CERN-SPS

06/2002-12/2005 Scientific employee at institute for nuclear physics Frankfurt (IKF) at the Goethe university under Prof. Dr. Dr. h.c. Reinhard Stock

Since 02/2006 Associate at McKinsey & Company, Inc., Frankfurt



## **Erklärung**

Ich erkläre hiermit, dass ich mich bisher keiner Doktorprüfung unterzogen habe.

Frankfurt am Main, den 30. Juni 2009

..... (Unterschrift)

## **Eidesstattliche Versicherung**

Ich erkläre hiermit an Eides Statt, dass ich die vorgelegte Dissertation über

Kaon and Pion Production in Centrality Selected Minimum Bias Pb+Pb Collisions at 40 and 158 A·GeV

selbständig angefertigt und mich anderer Hilfsmittel als der in ihr angegebenen nicht bedient habe, insbesondere, dass aus Schriften Entlehnungen, soweit sie in der Dissertation nicht ausdrücklich als solche mit Angabe der betreffenden Schrift bezeichnet sind, nicht stattgefunden haben.

Frankfurt am Main, den 30. Juni 2009

..... (Unterschrift)





# **Acknowledgment**

I would like to thank all those who supported me in the finalization of this thesis!

Special thanks goes to Claudia Höhne and my supervisors Reinhard Stock, Christoph Blume, Marek Gazdzicki, Herbert Ströbele, and Peter Seyboth and all members of the NA49 collaboration.

Thanks to my friends and family, especially to my wife Stephe for her patience.

